DESIGN OF APPARATUS FOR A STERILE NEUTRINO SEARCH USING ^{131}CS: THE HUNTER EXPERIMENT

A Dissertation

Submitted to

the Temple University Graduate Board

---

in Partial Fulfillment

of the Requirements for the Degree

DOCTOR OF PHILOSOPHY

---

by

Xunzhen Yu

May 2021

Examining Committee Members:

C. J. Martoff, Advisory Chair, Physics
Andreas Metz, Physics
Bernd Surrow, Physics
Robert Stanley, External Member, Chemistry

ABSTRACT

The unveiling of neutrino oscillation from observing the change in solar neutrino flux triggered physicists' interest in studying the nature of the neutrino mass. The prevailing theory of explaining the tiny neutrino mass is called the "see-saw" mechanism, which postulates that the neutrino flavor eigenstate is the mixing between mass eigenstate of active neutrinos of a small mass and (left-) right-handed "sterile" (anti-)neutrinos of a large mass. The sterile neutrino is believed to be a new physics beyond the Standard Model, which can explain many other outstanding physical problems, like warm dark matter, asymmetry of baryon, etc. The HUNTER (**H**eavy **U**nseen **N**eutrinos from the **T**otal **E**nergy-momentum **R**econstruction) experiment is a collaboration for searching for keV-mass range sterile neutrinos, and brings together an interdisciplinary team of researchers from Temple University, UCLA, Princeton University and the University of Huston to develop an apparatus capable of searching for sterile neutrinos with high precision.

In the HUNTER proposal, the radiation source generating neutrinos will be a cloud of atoms laser cooled and suspended by laser beams, the decay products except neutrinos will be detected by corresponding detectors, and their initial vector momenta will be reconstructed from the data recorded by the corresponding detectors. The missing mass in the decay, taken away by the neutrino, can then be evaluated from the energy and momentum conservation. The radiation sources of electron-capture decay are preferred for laboratory neutrino experiments because of the absence of energetic electrons in the decay products. ^{131}Cs is chosen by HUNTER to study the sterile neutrino mass and the mixing between sterile neutrinos and active neutrinos because of its short lifetime, simply decay products, and its alkali element spectral structure which enhances laser cooling and trapping.

The Phase 1 HUNTER experiment targeting sterile neutrinos in the range 20-300 keV/c^2 requires the design of spectrometers with momentum resolution of a part in a thousand or better. To detect a ^{131}Xe ion, a spectrometer consisting of numbers of annular electrodes has been designed. The potentials of the electrodes of the ion spectrometer were carefully optimized to form an electrostatic lens, with time focusing and spatial focusing to achieve a high momentum resolution for ions despite the extended source presented by the magneto-optical trap. The optimization algorithm presented in this dissertation achieves a momentum precision of $\sim$0.12%

($\sim$0.03%) for the high acceptance (high resolution) tune.

An electron spectrometer was designed without "double focusing" for detecting the electrons produced in ^{131}Cs decays. The electron trajectories are guided by a uniform electric and magnetic field. An octagonal shaped, magnetic shield was designed to diminish the influence of external magnetic fields on the electron trajectories. The achieved electron momentum resolution is $\sim$0.1 keV including extended source effects, sufficient for the desired missing mass resolution.

Other issues like the systematic errors of the ion spectrometer and the eddy current induced in the electrodes by periodically switching on/off the anti-Helmholtz coils of the magneto-optical trap were studied. The deformation of the spectrometer under its gravity was simulated using Autodesk Inventor.

ACKNOWLEDGEMENTS

First, I would like to express my deepest appreciation to my adviser C.J. Martoff for his support and instruction throughout this research. Without his tremendous encouragement, direction, invaluable advice, and patience during my PhD, it would be impossible for me to complete my research. Secondly, I would like to extend my deepest gratitude to my colleagues, and also friends, B. R. Lamichhane, F. Granato, for sharing their wisdom with me, and helping me throughout much of this work. I would like to thank all the entire HUNTER Collaboration for their commitment and hard work on designing and constructing the HUNTER apparatus. I would also like to thank the support from the W. M. Keck Foundation, Temple University, and the collaborating universities. This work would not have been possible without their financial support. My success at Temple University would not have been possible without the help and guidance from the Physics department, including the faculty, the staff, and members of my committee. Thank you so much.

Most importantly I would like to express my overwhelming gratitude for the love and unconditional support of my family and friends, who fill my world with light and with joy. Without them behind me, I would not be where I am today.

TABLE OF CONTENTS

Page

ABSTRACT ii

ACKNOWLEDGEMENTS iv

LIST OF TABLES vii

LIST OF FIGURES xi

CHAPTER

1 PHYSICAL BACKGROUND 1
  1.1 Electroweak Interaction 1
  1.2 Neutrino Physics 3
  1.3 See-Saw Mechanism 6
    1.3.1 Majorana Fermions 7
    1.3.2 Neutrino Mass Eigenstates in the Two-Flavor Case 9

2 INTRODUCTION 11
  2.1 Motivation 11
  2.2 HUNTER Experiment 14
    2.2.1 Choice of ^{131}Cs as Decay Source for HUNTER 16
  2.3 ^{131}Cs Decay Kinematics 20

3 THE HUNTER ION SPECTROMETER 23
  3.1 Wiley-McLaren Spectrometer 23
  3.2 Transverse-Focusing Spectrometer 25
  3.3 HUNTER Double-Focusing Spectrometer 25
  3.4 Estimate of Required Ion Spectrometer Resolution 28
    3.4.1 Limits to Wiley-McLaren Time Focusing 29
    3.4.2 Extraction Field Strength and Longitudinal Momentum Resolution 31
  3.5 Optimization Scheme 32
    3.5.1 Preliminary Optimization Procedure 33
    3.5.2 Description of Objective Function 37
  3.6 Brute-force Optimization 39
  3.7 Resolution and Reconstruction 40
  3.8 High Resolution Tune 44

4 SYSTEMATIC ERRORS OF THE ION SPECTROMETER 46
  4.1 Potentials and Positions of Electrodes 46
  4.2 Effect of Asymmetric Components 50
  4.3 Systematic Effect of Charge Accumulation 50
  4.4 Systematic Effects of Eddy Current Suppression Slots in Electrodes 54
  4.5 Systematic Effect Due to Different Spacer Configurations 58
  4.6 Systematic Effect due to Variations of Source Position 58

4.7 Influence of Mesh . . . 61

5 SYSTEMATIC ERRORS DUE TO MECHANICAL DEFORMATION OF SPECTROMETER UNDER GRAVITY . . . 67
5.1 Stiffness Improvement . . . 67
5.2 Spectrometer Deflection Under Gravity . . . 69

6 MAGNETIC FIELDS IN HUNTER . . . 72
6.1 MOT Coils . . . 72
6.2 Magnetic Force on Coils . . . 76
6.3 Eddy Current Magnetic Field . . . 79
6.3.1 Slotted Electrodes . . . 79
6.3.2 Effectiveness of Titanium Electrodes . . . 84

7 MAGNETIC SHIELD DESIGN . . . 86
7.1 Estimation of Permitted Stray Field Leakage into HUNTER Spectrometers . . . 86
7.2 HUNTER Magnetic Shield Design . . . 88
7.3 Interaction of Spectrometer with Magnetic Shield . . . 92
7.4 Shield Performance with Particle Trajectories . . . 93
7.5 Magnetic Effects of X-ray Detector Components . . . 94

8 BACKGROUNDS IN HUNTER . . . 98
8.1 Random Coincidence Background . . . 98
8.1.1 Random Background Simulation . . . 100
8.2 Other Physics Backgrounds . . . 101

9 SUMMARY . . . 105

BIBLIOGRAPHY . . . 115

APPENDICES . . . 116

A. ELECTRODES DESIGN . . . 116

B. POTENTIALS AND RESOLUTIONS . . . 121

LIST OF TABLES

2.1 Energies of x-rays and Auger electrons emitted in a ^{131}Cs decay and the corresponding branching ratios are listed in the table. The refilling channels and Auger energies are taken from Ref. [65]. The Auger "type" notation NNO and NOO are the same as N2O1O1 without specifying the electron numbers in the corresponding shells. 19

2.2 Table shows the energy levels of ^{131}Cs and ^{131}Xe [66] 19

3.1 The table lists the algorithms for generating ion kinematic characteristics for the optimization. 34

3.2 The momentum resolution of ions achieved by the optimization, for each emission angle without presence of the ∼8 G uniform magnetic field produced by the outside solenoids. The standard deviations of TOF (IR) of MCP and x-ray are included in calculating $\delta p_{\|}$ ($\delta p_{\perp}$). 41

3.3 The momentum resolution of ions achieved by the optimization, for each emission angle with presence of the ∼8 G uniform magnetic field. The standard deviations of TOF (IR) of MCP and x-ray are included in calculating $\delta p_{\|}$ ($\delta p_{\perp}$). 41

4.1 The values in the legends in Fig. 4.1 are listed in this table. $\mu(\mu_{TOF})$ and $\delta(\mu_{TOF})$ are the mean value and the standard deviation for the μ_{TOF} distribution, respectively. $\mu(\delta p_{\|})$ and $\delta(\delta p_{\|})$ are the mean value and the standard deviation for the distribution of reconstructed $\delta p_{\|}$, respectively. 47

4.2 The values in the legends in Fig. 4.2 are listed in this table. $\mu(\mu_{IR})$ and $\delta(\mu_{IR})$ are the mean value and the standard deviation of the μ_{IR} distribution, respectively. $\mu(\delta p_{\perp})$ and $\delta(\delta p_{\perp})$ are the mean value and the standard deviation of the distribution of reconstructed $\delta p_{\perp}$, respectively. 49

4.3 The momentum resolution of ions for each emission angle. The standard deviations of TOF, impact radius on MCP, and x-ray momentum are included in calculating $\delta p_{\|}$ ($\delta p_{\perp}$). 51

4.4 The momentum resolution of ions emitted in the upper half of YZ plane with the presence of the 10 V patch. The standard deviations of TOF (IR) of MCP and x-ray are included in calculating $\delta p_{\parallel}$ ($\delta p_{\perp}$). 53

4.5 The momentum resolution of ions emitted in the lower half of YZ plane which is close to the path with potential of 10 V. The standard deviations of TOF (IR) of MCP and x-ray are included in calculating $\delta p_{\parallel}$ ($\delta p_{\perp}$). 53

4.6 The variations of the ion momentum resolutions due to the offset of the MOT center are shown in the table. The positive (negative) offset in longitudinal direction means shifting the MOT center away from (toward) the ion MCP. In the vertical direction, the positive (negative) offset means shifting the MOT center opposite (along) the gravity direction. Degradation (Improvement) of the momentum resolution is represented as a positive (negative) percentage in the table. 60

4.7 The table lists the standard deviation of TOF and IR associated with the five models. 65

5.1 The detailed information of each component of the spectrometer. The inner diameters of electrodes are not listed because they have different values and the realistic inner radius is from a previous model. 70

5.2 The detailed information of each component of the spectrometer. 71

6.1 This table gives a matrix indicating all the different simulations that were done to study the abatement of eddy current effects. All the simulations in a given row share the same slot geometry and differ in which components were simulated or in the materials used. For the first row, each annular electrode has one full-radius slot, i.e. the electrodes are C-shaped, but the support rings are fully intact, as shown in Fig. 6.8. For the second row, electrodes and supporting rings are both full-radius slotted. For the third row, each electrode has two full-radius slots along a diameter, dividing the electrode into two equal halves. For the last row, the electrodes have partial radius slots, leaving a 2 mm radial thickness bridge across the outer edge of the gap in the C-shape. The width of all slots is 1 mm. The models in the column "Eb_Rb" and "Eb_Rs" include all the components. "E" refers to electrodes, "R" to support rings, and suffix "b" means bronze, while "s" means 316LN stainless steel. Using 316L stainless steel for the supporting rings generally does not change the induced magnetic fields compared to using 316LN. Two additional eddy current simulations not shown in the table were also run as baseline cases; the coils by themselves, with no vessel or other components, and the coils plus the 316L stainless steel vessel but no other components. 81

6.2 The labels in the table have the same meaning as table 6.1. The numbers are the peak values of the induced magnetic fields in Gauss. The number in red is the peak value of the magnetic field generated by the eddy current in the vacuum vessel flange. 83

7.1 The parameters of the electron-confining solenoids are shown in the table. Distances are measured from the center of MOT to the near end of solenoids. The solenoids are numbered from the inside near the MOT to the outside. 93

7.2 Reconstruction results for three different external stray magnetic field cases. Numbers in blue refer to the "no stray field" case; numbers in red refer to the "longitudinal 0.6G" case; numbers in black refer to the "transverse 0.6G" case. 94

9.1 Table of factors to determine the overall collection efficiency of HUNTER using full kinematic reconstruction. Phase 1 is funded and being built at this time. The remaining Phases are illustrative of possible upgrades to increase the efficiency and extend the coverage to lower sterile neutrino masses. 106

A.1 Optimized electrode potentials for the low resolution tune. unit: V 121

A.2 Optimization results of ions are shown in the table. $\delta p_{\parallel}$ and $p_{\perp}$ are the resolution of longitudinal and transverse momentum. μ_{TOF} (μ_{IR}) and σ_{TOF} (σ_{IR}) are the average TOF (IR) and the standard deviation of the TOF for 1000 ions in a group, respectively. 122

LIST OF FIGURES

1.1 Four-fermion vetex for β decay proposed by Fermi. 1

1.2 The flavor compositions of different neutrino mass eigenstates. The red, green, and blue represent e, μ, and τ neutrinos, respectively. The probability of different flavor eigenstates is represented by the length of related color overline. The two panels represent two different neutrino mass orders. The lightest mass of the neutrino and its flavor composition is unknown. The figure is from Ref. [21]. . . . 6

1.3 The figure is from Ref. [25]. The Yukawa coupling constants needed to produce observed particle masses simply by coupling to the Higgs field span over 12 orders of magnitude. There is a 6 order of magnitude difference between the neutrino and electron Yukawa coupling constant. 7

2.1 Radiative decay channel of sterile neutrino ν_2 in the mass eigenstate, with ν_1 representing the active neutrino produced in the decay. From Fig. 2 of Ref. [45] . 13

2.2 Limits on sterile neutrino coupling strength vs. mass over a wide mass range. Full lines from laboratory experiments: the limits provided by the β decay searches are in red, as summarized in Ref. [46]; blue curve is from the Ice Cube experiment [47]; the limits provided by electron energy spectra of the tritium decays are shown in green [48, 49]. Dashed lines (orange) show astrophysical limits permitting sterile neutrinos to be the galactic dark matter, from Fig. 57 of Ref. [50, 51]. These are from the non-observation of sterile neutrino decay x-rays from dark matter dominated objects, assuming 100%, 10%, 1% of the dark matter is sterile neutrinos of a single mass. Black dashed curves show projected HUNTER Phase 1 (proposed here) and possible future upgrades, which would check or surpass the astrophysical limits. 14

2.3 Scheme of the HUNTER apparatus. The spectrometer situated on left (right) side is for ion (Auger electron). The upper port is for pushing ^{131}Cs atoms to the MOT. 15

2.4 A cartoon of the reconstructed mass-squared spectrum of neutrinos in HUNTER, showing a separated population of events corresponding to production of a 60 keV/c^2 neutrino. . . . 17
2.5 Decay sequence of ^{131}Cs 17
2.6 Illustration of the K shell electron capture with emission of an x-ray from the N shell refilling. . . . 18

3.1 An illustration of the Wiley-McLaren model for producing a time-focusing spectrometer. Particles emitted from the extended MOT are accelerated by a uniform electric field over the region with MOT located. . . . 24
3.2 An illustration of the transverse focusing spectrometer with an electro-static lens. The red lines are the equipotential lines of the electric fields. E1 and E2 are the electric fields for producing the electrostatic lens, where E2 > E1. . . . 25
3.3 Plan view of the HUNTER apparatus, not to scale. Tracks for electrons (helical track heading to the left) and ions (heading to the right) are schematically shown, originating from the MOT (red ball at the center). Red and blue contours are optimized equipotentials simulated using SIMION with contour interval labeled in the figure. . . . 26
3.4 Enlarged view of the source region of the spectrometer. Voltage settings for the electrodes labeled E55-57 will be described in Section. 3.5.1. Electrodes E48 and E49 with a gap of 2 mm generate the electrostatic lens needed for transverse (spatial) focusing. . . . 28
3.5 (a): Flight time standard deviation vs. axial coordinate when the electric field around the MOT is uniform. The solid (dashed) line is for ions with an initial momentum toward (away from) the MCP. The electric field is 0.11 V/mm. (b): Same as (a), but for the nonuniform field at the MOT caused by the introduction of the electrostatic lens. The fringe field of the electrostatic lens changes the field at the MOT to 0.12 V/mm, with a field gradient of around 10^{-3} V/mm^2. The uniform electric field strength and the lens field strength used in this simulation are arbitrarily chosen as an example. . . . 30

3.6 This figure shows the success of the final brute-force optimization at achieving double focusing for the source size used in HUNTER. Plotted are the standard deviations of TOF in (a) and IR in (b), as a function of the axial coordinate. The MOT center is located at an axial coordinate of 1090 mm. The MCP would be placed at an axial coordinate of 158 mm. All ions have the same total momentum (330 keV/c) but different emission angles as indicated by the different colors. Dashed lines show results after the preliminary optimization but before the final optimization. Solid lines show results after the final optimization. Only 5 different emission angles are shown for clarity and the emission angles are: 0, 44, 88, 114, 158 degrees. The standard deviation minima (time focus positions) are seen to be located close to the MCP position. The minimum values are all nearly the same depending on the performance of the preliminary optimization. (Points beyond the MCP cannot be plotted for technical reasons - the field beyond the MCP corresponds to the internal MCP amplification field, and cannot be changed without subtly affecting the focusing results.) 36

3.7 The trendlines of TOF vs. $p_{\parallel}$. A linear trendline $y = p0 + p1 \cdot x$ was used to fit the data. The parameters $p0$ and $p1$ are shown in the legends in figure (a) and (b). In (a), there is no data for ions with $p_{\parallel}$ between -0.24 MeV/c to 0.24 MeV/c because in the present configuration, ions of charge 1e emitted in the corresponding angle range arrive at the MCP axial position with a transverse coordinate larger than the MCP radius. This could be remedied by using larger MCPs when they become available. However, the charge 1e ions are at most 40% of the ions produced in HUNTER, and still 50% of these ions are collected. 42

3.8 The trendlines of IR vs. $p_{\perp}$. A second-order polynomial trendline $y = p0 + p1 \cdot x + p2 \cdot x^2$ had to be used to give a satisfactory fit, in contrast to the first-order trends used for the $p_{\parallel}$ cases. 43

3.9 Simulation of reconstructed neutrino mass spectrum for the "high acceptance" spectrometer tune. 44

3.10 The distribution of the IR for ions with charge 2e in the high acceptance tune. . 44

4.1 The μ_{TOF} and the associated $\delta p_{\parallel}$ distributions of ions emitted in 10 polar angles are shown in separate figures according to their emission directions with respect to the ion MCP. (a) and (c) show the distributions of μ_{TOF} and the calculated $\delta p_{\parallel}$ for 5 groups of ions emitted opposite the ion MCP direction, respectively. The initial $p_{\parallel}$, mean values of μ_{TOF}, and the standard deviations of the μ_{TOF} distributions are shown in the legend of (a). The initial $p_{\parallel}$, mean values of reconstructed $\delta p_{\parallel}$, and the standard deviations of the $\delta p_{\parallel}$ are shown in the legend of (c). (b) and (d) are the same as (a) and (c), but for 5 groups of ions emitted toward the ion MCP 48

4.2 The μ_{IR} and $\delta p_{\perp}$ distributions of ions emitted in 10 polar angles are shown in these figures. (a) and (c) show the μ_{IR} distributions and calculated $\delta p_{\perp}$ for 5 groups of ions emitted opposite the ion MCP direction, respectively. The initial $p_{\perp}$, mean values of μ_{IR}, and the standard deviations of the μ_{IR} distributions are shown in the legend of (a). The initial $p_{\perp}$, mean values of $\delta p_{\perp}$, and the standard deviation of $\delta p_{\perp}$ are shown in the legend of (c). (b) and (d) are the same as (a) and (c), but for 5 groups of ions emitted toward the ion MCP. 49

4.3 (a): Solidworks model of the spectrometer, courtesy of the HUNTER collaborators Dr. Schneider and Dr. Lamichhane. The radial distance from the axis of the spectrometer to the outside thick (inside thin) rods traversing the large electrodes is 270 mm (250 mm). The radial distance from the axis to the rods traversing the small electrodes is 126.5 mm. (b): Spectrometer 3-D model in SIMION with contour lines in red. The contour lines represent the the spatial potential distribution produced by the electrodes in those specific planes. The potential of the two innermost contour lines in the front face is -18 V and the potentials of the rest of the contour lines from the inside to outside are -16 V, -14 V, -12 V and -10 V, respectively. 51

4.4 The central region of the 3-D model with a patch of 10 V simulating the charge accumulation effect. The coordinate system is shown in the lower lefthand corner. 52

4.5 (a): Cross section of the 3-D model of the spectrometer constructed in SIMION. Two double-headed arrows are marked in the figure to indicate the positions of a pair of circles where the electric fields are extracted for studying the influence of the clamps. (b): Electrode with four slits, because of the fourfold symmetry used in constructing the model. The clamp is shown in the inset. 55

4.6 Comparisons of E_z and E_r with (orange) and without (blue) clamps. Panels (a) and (c) show the effect on a circle aligned with an electrode, while (b) and (d) show the effect midway between the two electrodes. The radial fields are the most strongly affected, but the effect is tiny, shifting on average by a few nV/mm and showing azimuthal variations of the same order. 56

4.7 The comparison of the momentum resolutions calculated in the simulations listed in the legends of the figures. The labels in legends are explained below: 1. "2d" represents the data from a 2-D simulation, which serves as a reference. 2. "3d_clamp_between_slits" ("3d_clamp_on_slit_plane") represents the data for ions flown with an initial azimuthal angle of 0 (42) degree through the 3-D model with clamps. 3. "3d_no_clamp_between_slits" ("3d_no_clamp_on_slit_plane") represents the data for ions flown with an initial azimuthal angle of 0 (42) degree through the 3-D model without clamps. 57

4.8 The comparison of the momentum resolutions for different spacer configurations. 59

4.9 Cross section of the 3-D model. The potential differences between adjacent red, blue, green equipotentials are 100 V, 1 V, 0.1 V, respectively. The left inset is an electrode. The outer and inner side lengths are L1 and L3, respectively. The right inset is the mesh with 6×6 cells. The frame width of the mesh is (L1 - L2)/2. In the model, L1, L2 and L3 are 3 mm, 1 mm and 2 mm, respectively. 62

4.10 The variation of field along the line parallel to the symmetric axis and passing through the mesh cell at the center. The data marked in blue, orange, yellow, gray, green are associated with **Case 1**, **Case 2**, **Case 3**, **Case 4**, **Case 5**, respectively. The blue markers are overlapped by other markers. 63

4.11 Illustration of the simulation model with full-width mesh. Square electrodes with outer side length of L1 and inner side length of L3 are used in the simulation. A frameless mesh with side length of L1 is used to separate two different electric fields represented in green and red. 64

4.12 Illustration of the enlarged model similar to Fig. 4.11, but the side lengths of the electrodes and mesh are increased by 1.92 mm. 64

4.13 The projection of the ion trajectories penetrating the central cell of the accelerating mesh. The frames in gray color represent the wires of the woven mesh. Left: the projection of the initial ion position in the mesh plane. Right: the projection of the impact positions of ions, where the black star shape dots show where ions strike the mesh frame. 65

4.14 The projection of the ion trajectories penetrating a cell on the edge of the accelerating mesh. The frames in gray color represent the wires of the woven mesh. Left: the projection of the initial ion position in the mesh plane. Right: the projection of the impact positions of ions, where the black star shape dots are the ions striking the mesh frame. The trajectories were distorted for the ions passing through the cells on edges of the mesh by comparing the projection of impact positions in Fig. 4.13 and Fig. 4.14. 66

5.1 Comparing the rod deflection due to the different loads. (a): The rod deflection due to its own weight plus the weight of the disk. (b): The rod deflection due to its own weight plus a concentrated force equal to the weight of the disk. 68

5.2 The rod deflection of the spectrometer without rings. In the simulation, the electrodes were supported by 8 rods. The two end surfaces of the supporting rods were "fixed". 68

5.3 Comparing the rod deflection of the different fixing methods. In this model, 8 rods pass through the electrodes and 4 supporting rings. (a): the two end surfaces of each rod are fixed. The maximum deflection as shown in the color bar is around 0.04 mm. (b): two "ears" are used to clamp the ends of the rods. In this simulation, the maximum deflection is around 0.04 mm. 69

5.4 The figure shows the mechanical support structure of the spectrometer. The components are marked in the picture. 70

5.5 The concept of the electrode design is shown in the figures. 71

5.6 The figure shows the spectrometer deflection. The yellow arrow indicates the direction of the gravity. The maximum deflection indicated by the color bar is around 0.05 mm 71

6.1 A typical configuration of a MOT. (a): A MOT consists of an arrangement producing both velocity damping (optical molasses) and a restoring force. (b): Schematic spectral splittings of a two-level atom. 73

6.2 (a): The axial component of the calculated magnetic field produced by the anti-Helmholtz coils with 4 × 4 turns of wires in each coil. The current in each turn of wire is 28.14 A. (b): The gradient of the field in (a). 75

6.3 (a): The magnetic field produced by the anti-Helmhlotz coils with biased currents plus the 8 G external magnetic field. (b): The gradient of the field in (a). 75

6.4 A truncated 2-D model of the spectrometer. The inset shows the details of the MOT coils on one side. 76

6.5 (a): The switching cycle of the MOT coils current with a transition time of 100 µs. (b): Time dependence of the axial magnetic field at $z = 55$ mm. The peak value of the axial magnetic field is around 26 G. 77

6.6 (a): Axial force acting on the coil. (b): Force acting on the electrode next to the coil in the downstream direction of the spectrometer. The force after switching on the coils is fitted with an exponential to study the decay time constant of the eddy current inside the electrode given that this force is the repulsion caused by the eddy current and the coil current. 78

6.7 The cross-section view of the simplified spectrometer model. This model is based on an old design of the spectrometer, but the conclusion still stands. 80

6.8 Left: Illustration of a C-shaped electrode. Right: Cross section of the electrode. For small electrodes, a, b and c are 93 mm, 0.3 mm and 54 mm, respectively. . . 80

6.9 Comparison of the axial magnetic fields at different time slots. The time slots are labeled in the titles of the figures. The magnetic fields are not symmetric with respect to the center of the MOT because these simulations are based on an old design of the spectrometer, in which the ion and electron spectrometer arms were asymmetric. The labels in the legend are explained following their orders in the legend: 1. "one_slot_Eb_Rb_RingNotSp": The electrodes are fully split; the materials of the electrodes and supporting rings are bronze; the supporting rings are not split; 2. "one_slot_Eb_Rs_RingNotSp": It has the same configuration as "one_slot_Eb_Rb_RingNotSp", except that the supporting rings are stainless steel; 3. "one_slot_E&R_Eb_Rs": The electrodes and the supporting rings are fully split; the materials of the electrodes and the supporting rings are bronze and stainless steel, respectively; 4. "coil_noVessel": Only the MOT coils are included in the simulation. The magnetic field produced by the coils serves as a reference for the other simulations; 5. "coil_Vessel": The MOT coils and the chamber are included in the simulation. This simulation is for studying the eddy current magnetic field produced by the eddy currents induced in the chamber; 6. "oneBridgedSlot_Eb_Rs_RingNotSp": The electrodes are partially split; the materials of the electrodes and the supporting rings are bronze and stainless steel, respectively; the supporting rings are not split; 7. "two_slot_Eb_Rb_RingNotSp": The electrodes are split into two equal halves; the materials of the electrodes and the supporting rings are bronze; 8. "two_slot_Eb_Rs_RingNotSp": The configuration is the same as "two_slot_Eb_Rb" except that the supporting rings are made of stainless steel. 82

6.10 Comparison of Bz of three simulations at $t = 22$ ms and $t = 24$ ms. The eddy current magnetic field generated in the simulation with only coils and a vessel serves as reference. "ELb_ELOD_SID_b_ESb" means that the large electrodes, the large electrode with a small inner diameter, and the small electrodes are made of bronze. "ELb_ELOD_SID_b_ESTi" is the same as "ELb_ELOD_SID_b_ESb" except that the small electrodes are made of titanium. These simulations are based on the latest spectrometer model, in which the ion arm and the electron arm are symmetric. The thicknesses of the small electrodes and large electrodes are 0.3 mm and 0.6 mm, respectively. 85

7.1 (Reproduced from Ref. [70]) Projection of an electron trajectory for the idealized case of uniform magnetic field. Point O is the initial point of electron trajectory and C is the impact position. ωt is the total spiraling angle, where ω is the angular frequency. R is the radius of the spiral. 87

7.2 (a): Results of measuring the 3-D background magnetic field in the laboratory. The disorder of the magnetic field on the right side of the plot is due to highly magnetic objects, like a breaker box and an equipment rack. (b): Illustration of the position at which the spectrometer will be situated. 89

7.3 Long term measurement of the background magnetic field. The step of the magnetic field measurement at $t = 5$ h is an artifact due to a misplaced ruler close to the magnetometer. 89

7.4 Left: The end-view of the chamber with the octagonal magnetic shield designed here. The red and blue lines represent the flat and bent components of the shield. Right: Zoom in of the details in the circle to show how the base of a sleeve is clamped between shield pieces. The unit of size marked in the figure is mm. . . . 90

7.5 (a): A quadrant of the magnetic shield model with sleeves. In this figure, the X axis is along the long axis of the shield pointing in the right direction, the Y axis is in the vertical direction with the positive direction pointing up. The Z axis is pointing outward perpendicular to the XY plane. (b): Contour lines in the XZ plane of the field inside the shield for a 0.6 G external longitudinal field. The range of the contour lines is from 0 to 30 milligauss with a contour interval of 0.2 milligauss. 91

7.6 (a): The X component of the magnetic field within the shielded volume along the central axis for the longitudinal external magnetic field of 0.6 G. (b): The X component of the magnetic field within the shielded volume along the central axis for the transverse external magnetic field of 0.6 G. 92

7.7 X component of the magnetic field produced by the solenoids inside the different models of magnetic shield. 93

7.8 (a): A re-entrant flange with a few SiPM modules. (b): The assembly of a re-entrant flange and the central chamber. The two crossed cylinders passing through the center of the chamber represent the laser beams for trapping Cs atoms. One re-entrant flange is placed in each wire-seal-flanged tube with an outer diameter of 16 inches. 95

7.9 Typical effect of magnetic fields perpendicular to PMT from Ref. [116] 96

7.10 Configuration of PMT magnetic shields for simulations. The PMT shield cases in the magnetic shield model are oriented toward the x-ray port. 16 PMT shield cases form a 4 × 4 array as shown in the figure. 96

7.11 Simulated magnetic fields along the axis of the two PMT shields in Fig. 7.10, marked with red cross. “inside shield” in the legend means the PMT shield at the center of the shield array. “outside shield” means the PMT shield on the edge of the shield array. 97

8.1 Distribution of the reconstructed decay events in m_ν^2 vs. p_ν^2. Considering the standard deviation of the mass-squared spectrum of the neutrino, the X axis range is set to [-400, 400] $(\mathrm{keV}/c^2)^2$. The black (green) dots are the events with one (two) Auger(s), and the ions are emitted from the hemisphere of the MOT opposite the ion MCP. The red (blue) dots are for the events with one (two) Auger(s) and the ions are emitted from the hemisphere of the MOT facing the ion MCP. The details of the events’ distribution are shown in the inset. The functions of the pair of red lines are $y = (\tilde{Q}^2 \pm 9.6) - m_\nu^2$ 99

8.2 (a): The spectrum of $\tilde{Q}$ of simulated random background events without applying the $\tilde{Q}$ cut. The $\tilde{Q}$ cut are represented by the parallel red lines. This shows the effectiveness of the $\tilde{Q}$ cut in suppressing random coincidence background to be 14%. 101

8.3 Scatter plot of the random coincidence background events. The black (green) dots are the random coincidence background events with one (two) Auger(s), and the ions are emitted from the hemisphere of the MOT opposite the ion MCP. The red (blue) dots are for the random coincidence background events with one (two) Auger(s) and the ions are emitted from the hemisphere of the MOT facing the ion MCP. 102

8.4 The scatter plot of triple coincidence background events for different cases. Each sub-plot is associated with an item in the legend of Fig. 8.3. The small window in each sub-plot is a zoom in of the plot around $m_\nu^2 = 0$. 102

8.5 Mass-squared spectrum of the RCBE accepted by the $\tilde{Q}$ cut. The smooth distribution cannot easily give a false sterile neutrino mass peak. In this simulation, 2×10^6 events were produced. 1.8×10^6 events passed through two preliminary momentum cuts [200, 400] keV and [5, 30] keV for ions and electrons, respectively. 2.6×10^5 events from the preliminary selection passed through the $\tilde{Q}$ cut, and formed the mass-squared spectrum. 103

8.6 Simulated “discovery spectrum” with 40 sterile neutrino events giving a 5σ peak at $m_\nu^2 = (60~\mathrm{keV/c^2})^2$ using the current reconstruction width 329 $(\mathrm{keV/c^2})^2$. This corresponds to a mixing of sterile neutrinos with active neutrinos given by $\sin^2\theta = 2 \times 10^{-4}$ based on the current estimation of one year background events (2.1×10^5 events) as shown in Table. 9.1. The curves are: magenta- random coincidence background; green- random plus ion-atom scattering; dark blue- backgrounds plus zero-mass and $(60~\mathrm{keV/c^2})^2$ peak. 104

1 Small electrode in the source region. 117

2 Small electrode facing the MOT. 118

3 Small electrode sandwiched between the two halves of coil holders. 119

4 Half of the coil holder. 120

CHAPTER 1

PHYSICAL BACKGROUND

In 1930, Wolfgang Pauli proposed a new particle to explain the observation of the continuous electron energy spectrum in β decay. The new particle was named the “neutrino”. 26 years after the neutrino was proposed, Clyde Cowan, Frederick Reines, and others detected neutrinos for the first time by using inverse β decay [1].

In the SM, each charged lepton (e, ν, τ) has its own “flavor” of neutrino, which are all experimentally observed. The theoretical description of the decays with the participation of neutrinos was not complete until the unification of electromagnetic and weak interactions proposed by Glashow, Salam, and Wemberg [2]. Later experimental observation of neutrino oscillation triggered the interest of physicists to study neutrino mass. The prevailing theory explaining the very small neutrino mass implied by oscillations is called the “see-saw” mechanism, which provides the theoretical support for the HUNTER experiment.

1.1 Electroweak Interaction

In 1934, Fermi proposed a Lagrangian density term analogous to electromagnetic interactions to describe β decays. Particles involved in β decays are assumed to interact at a four-fermion vertex as shown in Feynman diagram Fig. 1.1. For an electromagnetic interaction like $p \rightarrow p + \gamma$, the interaction Lagrangian density is

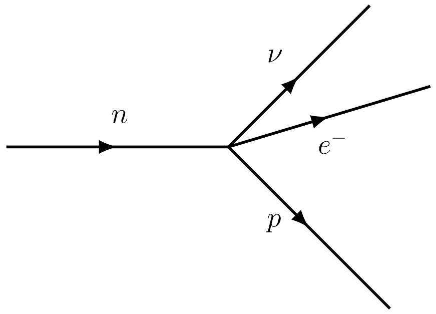

Figure 1.1: Four-fermion vetex for β decay proposed by Fermi.

$$\mathcal{L} = e(\overline{u}_p \gamma^\mu u_p) A_\mu \tag{1.1}$$

where $\overline{u}_p\gamma^\mu u_p$ is the proton current, u_p is the Dirac spinor of the proton. A_μ is the Dirac spinor of the photon. For the weak interaction β decay $n \to p + e^- + \overline{\nu}$, A_μ is replaced by the lepton current $\overline{u}_e\gamma_\mu u_\nu$ as shown in Eq. 1.2.

$$\mathcal{L} = G_F(\overline{u}_p\gamma^\mu u_n)(\overline{u}_{e^-}\gamma_\mu u_\nu) + h.c. \tag{1.2}$$

where γ^μ is Dirac matrix [3]. G_F is the coupling constant describing the interaction strength. For electroweak interaction, experimental results for decays give a value $G_F = 1.167 \times 10^{-5}$ GeV^{-2} [4].

For the case of the then-unknown weak interaction, the pure vector current-current coupling of Eq. 1.2 must be generalized. Considering the Lorentz invariants of a physics system, Eq. 1.2 can be written as

$$\mathcal{L} = \sum_i G(\overline{u}_p O_i u_n)(\overline{u}_{e^-} O^i u_\nu) + h.c. \tag{1.3}$$

where G is the coupling constant for different couplings represented by O_i. The possible Lorentz covariants of O_i are listed below

$$O_S = 1 \qquad Scalar(S) \tag{1.4}$$

$$O_V = \gamma_\mu \qquad Vector(V) \tag{1.5}$$

$$O_T = \sigma_{\mu\nu} = \frac{i}{2}(\gamma_{mu}\gamma_\nu - \gamma_\nu\gamma_\mu) \qquad Tensor(T) \tag{1.6}$$

$$O_A = \gamma_5\gamma_\mu \qquad AxialVector(A) \tag{1.7}$$

$$O_P = \gamma_5 \qquad Pseudoscalar(p) \tag{1.8}$$

Fermi proposed that β decay should be governed by his four-fermion vertex with a coupling comprised of a sum of these invariants, which could be distinguished kinematically. Fermi's proposal about β decay was extended when Yang and Lee put forward the hypothesis of parity violation in the weak interaction to explain the two decay channels of K^+ in 1956 [5]. The experimental observation of parity violation implies particular combinations of invariants in Eq. 1.3. The parity violation in the weak interaction was proved by Chien-Shiung Wu in 1957 by observing the anisotropic emission direction of electron in the decay of polarized ^{60}Co [6]. The experiment showed that only left-handed electrons are created in the β decay. To include the parity violation in weak interaction theory, the weak vector and axial vector terms must be combined into the weak currents

$$j = j_V + j_A = \overline{u}_1 O_i u_2 + \overline{u}_1 O_i C_i \gamma_5 u_2 = \overline{u}_1 O_i (1 + C_i \gamma_5) u_2 \tag{1.9}$$

The later development of particle physics experiments and theories indicate that the four-fermion vertex is actually two separate vertices joined by the propagator of very heavy $W^{\pm}$ or Z^0 bosons [7]. Thus, Eq. 1.3 in modern notation is written

$$\mathcal{L} = \sum_i G_i (\overline{u}_p O_i (1 + C_i \gamma_5) u_n) \frac{-i(g_{\mu\nu} - q_\mu q_\nu / M^2)}{q^2 - M^2} (\overline{u}_{e^-} O^i (1 + C_i \gamma_5) u_\nu) + h.c. \tag{1.10}$$

where G_i is the coupling constant of different bilinear forms. $(-i(g_{\mu\nu} - q_\mu q_\nu / M^2)/(q^2 - M^2)$ is the intermediate vector boson propagator. M is the mass of the mediator, q is the exchange of the momentum in weak interactions. $C_i = -1$ is determined by experimental results. Experimental results to date imply that the fundamental weak interaction only includes $i = V, A$ terms. In nuclear physics, the $i = V, A$ terms are known as the Fermi transition and the Gamow-Teller transition [8], respectively.

Eq. 1.10 is for "charged current" weak interactions in which the lepton charge changes, which are mediated by the charged bosons $W^{\pm}$. Neutral weak currents also exist, though not relevant to HUNTER. These allow leptons to interact without changes of electric charge and are mediated by the Z^0 boson with different coefficients as shown in Eq. 1.11

$$j_{Z^0} = \overline{u}_1 \gamma^\mu (c_V - c_A \gamma^5) u_2 \tag{1.11}$$

The definition of c_V and c_A are determined by the unification of the electromagnetic interaction and weak interaction [9, 10, 11].

1.2 Neutrino Physics

In the SM, Higgs bosons are introduced to explain the mass of charged fermions, but the mass of neutrinos was taken to be zero. Terrestrial observations of the solar electron neutrino deficit in the 1990s [12, 13, 14] were ultimately explained by the fact that neutrinos are massive. The solar electron neutrino flux is determined by the nuclear fusion reactions happening in the Sun, which produce the Sun's energy, which can be computed from the Sun's total energy output. However, only one third of the predicted solar electron neutrino flux was observed on the Earth. The solar electron neutrino deficit is explained by the transformation of neutrino flavor eigenstates along the propagation path, which is called “neutrino oscillation”. Neutrino oscillations postulate that the neutrino flavor eigenstate emitted in a charged-current weak interaction is a mixture of different mass eigenstates, which mix with one another and dephase due to their Heisenberg wave function evolution. The later nuclear reactor neutrino experiments [15], accelerator neutrino experiments [16, 17], and atmospheric neutrino experiments [18, 19] conclusively proved the existence of neutrino oscillations.

To understand the neutrino oscillation theory, we start by writing the three neutrino flavor eigenstates as the linear combination of the mass eigenstates in a matrix form as shown in Eq. 1.12

$$\begin{pmatrix} \nu_e \\ \nu_\mu \\ \nu_\tau \end{pmatrix} = U_{PMNS} \begin{pmatrix} \nu_1 \\ \nu_2 \\ \nu_3 \end{pmatrix} = \begin{pmatrix} U_{e1} & U_{e2} & U_{e3} \\ U_{\mu 1} & U_{\mu 2} & U_{\mu 3} \\ U_{\tau 1} & U_{\tau 2} & U_{\tau 3} \end{pmatrix} \begin{pmatrix} \nu_1 \\ \nu_2 \\ \nu_3 \end{pmatrix} \tag{1.12}$$

The transformation matrix U_{PMNS} is called the Pontecorvo-Maki-Nakagawa-Sakata (PMNS) matrix which is conceptually similar to the Cabibbo–Kobayashi–Maskawa (CKM) matrix for quarks [20]. The PMNS matrix can be parameterized without loss of generality as shown in Eq. 1.13

$$U_{PMNS} = \begin{pmatrix} c_{12}c_{13} & s_{12}c_{13} & s_{13}e^{-i\delta} \\ -s_{12}c_{23} - c_{12}s_{23}s_{13}e^{i\delta} & c_{12}c_{23} - s_{12}s_{23}s_{13}e^{i\delta} & s_{23}c_{13} \\ s_{12}s_{23} - c_{12}c_{23}s_{13}e^{i\delta} & -c_{12}s_{23} - s_{12}c_{23}s_{13}e^{i\delta} & c_{23}c_{13} \end{pmatrix} \tag{1.13}$$

where $c_{ij} = \cos\theta_{ij}$, $s_{ij} = \sin\theta_{ij}$, and θ_{ij} are three real-valued mixing angles. δ is the Dirac phase factor.

To illustrate the neutrino oscillation theory, we write a neutrino flavor state at $t = 0$ as

$$|\nu_\alpha\rangle = \sum_{k=1}^{3} U_{\alpha k} |\nu_k\rangle \tag{1.14}$$

where $|\nu_\alpha\rangle$ is the neutrino flavor eigenstate at $t = 0$. $U_{\alpha k}$ is the corresponding element in the PMNS matrix. $|\nu_k\rangle$ is the k-th neutrino mass eigenstate at $t = 0$. The Heisenberg time evolution of $|\nu_k\rangle$ is

$$|\nu_{k(t)}\rangle = \exp\left(-iE_k t\right) |\nu_k\rangle \tag{1.15}$$

where $E_k^2 = |\vec{p}|^2 + m_k^2$ is the total energy of $|\nu_k\rangle$. Thus, the time evolution of the neutrino flavor eigenstate is the superposition of the time evolution of neutrino mass eigenstates,

$$\begin{aligned} |\nu_{\alpha(t)}\rangle &= \sum_{k=1}^{3} U_{\alpha k} |\nu_{k(t)}\rangle \\ &= \sum_{k=1}^{3} U_{\alpha k} \exp\left(-iE_k t\right) |\nu_k\rangle \end{aligned} \tag{1.16}$$

Neutrino detection is based on the inverse beta decay or other charged-current weak interactions, which transform the neutrino into a visible charged lepton, thereby collapsing its wave function into a flavor eigenstate. The mixing coefficient of neutrino flavor eigenstate can be evaluated by developing the inverse transformation of Eq. 1.14 to the Eq. 1.16. The inverse transformation is shown in Eq. 1.17

$$|\nu_k\rangle = \sum_{\beta=e,\mu,\tau} U^*_{\beta k} |\nu_\beta\rangle \tag{1.17}$$

The neutrino flavor eigenstate at time t expressed in terms of flavor eigenstates is

$$|\nu_{\alpha(t)}\rangle = \sum_{k=1}^{3} \sum_{\beta=e,\mu,\tau} U_{\alpha k} U^*_{\beta k} \exp\left(-iE_k t\right) |\nu_\beta\rangle \tag{1.18}$$

The probability of finding the neutrino in a different flavor eigenstate $|\nu_\beta\rangle$ after propagating through a distance L is

$$\begin{aligned} P_{\alpha\beta} &= |\sum_{k=1}^{3} U_{\alpha k} U^*_{\beta k} \exp\left(-iE_k t\right)|^2 \\ &= \sum_{k=1}^{3} \sum_{j=1}^{3} U_{\alpha k} U^*_{\beta k} U^*_{\alpha j} U_{\beta j} \exp\left(-iE_k t\right) \exp\left(iE_j t\right) \end{aligned} \tag{1.19}$$

The simplification of neutrino energy under the ultra-relativistic condition is

$$E = \sqrt{|\vec{p}|^2 + m^2} = |\vec{p}| \sqrt{1 + \frac{m^2}{|\vec{p}|^2}} = |\vec{p}| + \frac{m^2}{2|\vec{p}|} \tag{1.20}$$

Assume the neutrino is propagating with the speed of light given its tiny mass, we have $L = ct$, and $|\vec{p}| \approx E_k \approx E_j = E$ [11]. Eq. 1.19 can be written as

$$P_{\alpha\beta} = \sum_{k=1}^{3} \sum_{j=1}^{3} U_{\alpha k} U^*_{\beta k} U^*_{\alpha j} U_{\beta j} \exp -i \frac{(m_k^2 - m_j^2) L}{2E} \tag{1.21}$$

Eq. 1.21 indicates that the transformation between neutrino flavor eigenstates is governed by the differences of the squares of masses for the mass eigenstates. The results from neutrino oscillation experiments for the neutrino mass differences and mixing angles can be found in Ref. [21, 22].

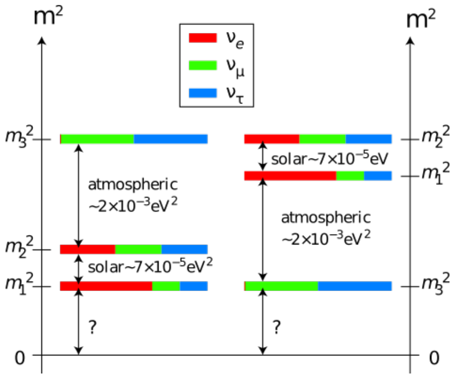

Figure 1.2: The flavor compositions of different neutrino mass eigenstates. The red, green, and blue represent e, μ, and τ neutrinos, respectively. The probability of different flavor eigenstates is represented by the length of related color overline. The two panels represent two different neutrino mass orders. The lightest mass of the neutrino and its flavor composition is unknown. The figure is from Ref. [21].

According to Eq. 1.21, neutrino oscillation experiments only provide the squared-mass differences between different neutrino mass eigenstates. The current experimental situation is shown in Fig. 1.2. Two possible mass orderings are permitted by the experimental data. The underlying mechanism of the mixing and the origins of the very small masses are not understood. The electron neutrino mass upper limit provided by the latest KATRIN experiment is $m_{\nu_e} < 1.1$ eV [23] .

In the Higgs Mechanism, the Dirac mass is the product of the Yukawa coupling constant y_D and the Higgs field v [22, 9, 24], where $v = 174$ GeV is the vacuum expectation value of a neutral Higgs field as determined from other high energy physics experiments. Considering the neutrino mass provided by KATRIN, the expected Yukawa coupling constant of a neutrino is $\sim 6 \times 10^{-12}$, which is at least 6 orders of magnitude smaller than the Yukawa coupling constant of the electron as shown in Fig. 1.3. Both the wide spread of the Yukawa coupling constants and the gaps of Yukawa coupling constants between neutrinos and other fermions imply that a new theory is required to explain the neutrino mass.

1.3 See-Saw Mechanism

Adding neutrino mass to the SM usually involves introducing a new heavy particle, a massive right-handed singlet Dirac neutrino. A Dirac neutrino is one in which the Lagrangian of the

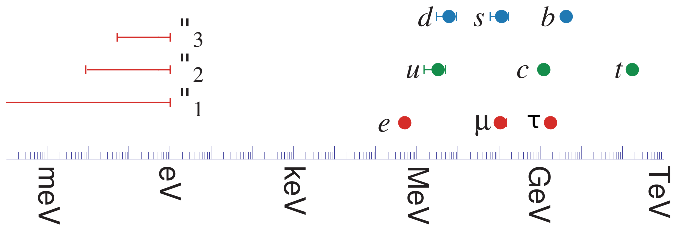

Figure 1.3: The figure is from Ref. [25]. The Yukawa coupling constants needed to produce observed particle masses simply by coupling to the Higgs field span over 12 orders of magnitude. There is a 6 order of magnitude difference between the neutrino and electron Yukawa coupling constant.

neutrino mass term is given by

$$\mathcal{L}^D_{mass} = -m_D(\overline{\nu_L}\nu_R + \overline{\nu_R}\nu_L) \tag{1.22}$$

Alternatively, mass can be introduced by assuming that neutrinos are Majorana particles. Thus, the mass term of a Majorana neutrino in the Lagrangian is the product of the left-handed Majorana neutrino and its anti-particle. The co-existence of right-handed Dirac neutrinos and left- and right-handed Majorana neutrinos proposed by Takehiko Asaka and Mikhail Shaposhnikov in 2005 [26] extends the SM to an upgraded model called the neutrino minimal standard model (νMSM). Details of the mass generation process with both Dirac and Majorana masses are given in the following subsections. For simplicity, only the single flavor case is treated.

1.3.1 Majorana Fermions

The concept of Majorana fermions was proposed by Ettore Majorana in 1937. Majorana fermions fulfill two conditions [3]:

1. The Majorana fermions satisfy the Dirac equation $(\gamma^\mu i\partial_\mu - m)\Psi = 0$.
2. The fermions and their anti-particles are identical $\Psi^c = \Psi$, where $\Psi^c = C\overline{\Psi}^T$ and $\Psi = \Psi_L + \Psi_L^c$. C represents the charge conjugation operation.

The charge conjugation is $C = i\gamma^2\gamma^0$. The factor $i\sigma_2$ in γ^2 has the property of flipping spin orientations. Thus, we have $\Psi_R^c = \Psi_L$, and $\Psi_L^c = \Psi_R$.

$$\begin{aligned}\Psi_R^c &= C\overline{\Psi_R}^T \\ &= i\gamma^2\gamma^0(\Psi_R^\dagger\gamma^0)^T \\ &= \frac{1}{2}i\gamma^2(1+\gamma^5)\Psi^* \\ &= \frac{1}{2}(1-\gamma^5)\Psi^c \\ &= \Psi_L\end{aligned} \tag{1.23}$$

The Lagrangian mass term of left-handed and right-handed Majorana neutrinos can be expressed as

$$\mathcal{L}^L_{mass} = -\frac{1}{2}m_L(\overline{\nu_L}\nu_L^c + \overline{\nu_L^c}\nu_L) \tag{1.24}$$

$$\mathcal{L}^R_{mass} = -\frac{1}{2}m_R(\overline{\nu_R}\nu_R^c + \overline{\nu_R^c}\nu_R) \tag{1.25}$$

The mixed Lagrangian mass terms of neutrinos, including the Dirac mass and the Majorana mass, can be simplified by applying Eq. 1.23 [27]

$$\begin{aligned}\mathcal{L}_{mass} &= \mathcal{L}^D_{mass} + \mathcal{L}^L_{mass} + \mathcal{L}^R_{mass} \\ &= -\frac{1}{2}\begin{pmatrix}\overline{\nu_L} & \overline{\nu_R^c}\end{pmatrix}\mathcal{M}^{D,M}\begin{pmatrix}\nu_L^c \\ \nu_R\end{pmatrix} - \frac{1}{2}\begin{pmatrix}\overline{\nu_L^c} & \overline{\nu_R}\end{pmatrix}\mathcal{M}^{D,M}\begin{pmatrix}\nu_L \\ \nu_R^c\end{pmatrix}\end{aligned} \tag{1.26}$$

where $\mathcal{M}^{D,M}$ is the mass matrix

$$\mathcal{M}^{D,M} = \begin{pmatrix} m_L & m_D \\ m_D & m_R\end{pmatrix} \tag{1.27}$$

Neutrino mass eigenvalues can be computed by diagonalizing the mass matrix [22, 28]. The physical mechanism giving rise to these mass terms is not specified at this level of analysis.

1.3.2 Neutrino Mass Eigenstates in the Two-Flavor Case

A unitary matrix which can diagonalize the full 2×2 neutrino mass matrix of Eq. 1.27 is

$$U = \begin{pmatrix} \cos\theta & \sin\theta \\ -\sin\theta & \cos\theta \end{pmatrix} \tag{1.28}$$

The neutrino mass eigenstate η is

$$\begin{pmatrix} \eta_{1L} \\ \eta_{2L} \end{pmatrix} = U^T N = U^T \begin{pmatrix} \nu_L \\ \nu_R^c \end{pmatrix} \tag{1.29}$$

The mass eigenstates can be evaluated by diagonalizing the mass matrix $\mathcal{M}^{D,M}$

$$U^T \mathcal{M}^{D,M} U = U^T \begin{pmatrix} m_L & m_D \\ m_D & m_R \end{pmatrix} U = \begin{pmatrix} m_1 & 0 \\ 0 & m_2 \end{pmatrix} \tag{1.30}$$

where m_1 and m_2 represent the different neutrino mass eigenvalues.

$$m_{1/2} = \frac{m_L + m_R}{2} \mp \sqrt{(\frac{m_L - m_R}{2})^2 + m_D^2} \tag{1.31}$$

The mixing angle of different neutrinos is [29]:

$$\tan 2\theta = \frac{2m_D}{m_L - m_R} \tag{1.32}$$

The tiny neutrino mass evaluated from neutrino oscillations can be achieved by choosing suitable values for m_L, m_R and m_D corresponding to the reasonably associated Yukawa coupling constants. This way of producing light neutrino from the combination of different neutrino masses is call the “see-saw mechanism”. The type I see-saw mechanism is the prevailing type, in which $m_L = 0$, $m_R >> m_D$ [22].

$$m_1 \approx -\frac{2m_D^2}{m_R}, \qquad m_2 \approx m_R \tag{1.33}$$

A Majorana phase related matrix Φ can be multiplied to the diagonalized mass matrix to convert the negative mass m_1 to positive [30].

$$\Phi = \begin{pmatrix} -i & 0 \\ 0 & 1 \end{pmatrix} \tag{1.34}$$

The neutrino mass eigenstate in Eq. 1.29 can be rewritten as

$$\begin{pmatrix} \eta_{1L} \\ \eta_{2L} \end{pmatrix} = \Phi^T U^T N \approx \begin{pmatrix} -i & 0 \\ 0 & 1 \end{pmatrix} \begin{pmatrix} 1 & -\frac{m_D}{m_R} \\ \frac{m_D}{m_R} & 1 \end{pmatrix} \begin{pmatrix} \nu_L \\ \nu_R^c \end{pmatrix} = \begin{pmatrix} -i\nu_L - i\frac{m_D}{m_R}\nu_R^c \\ \frac{m_D}{m_R}\nu_L + \nu_R^c \end{pmatrix} \tag{1.35}$$

The HUNTER experiment is partially motivated by the success of the see-saw mechanism in accounting for light neutrino masses if as-yet unobserved heavy neutrinos exist in nature. In the HUNTER experiment, the sterile neutrino will be produced by oscillation of the electron-type neutrino produced in the electron-capture decay of ^{131}Cs through mixing with active neutrinos.

CHAPTER 2

INTRODUCTION

2.1 Motivation

The development of particle physics in the 20th century unveiled the nature of matter that comprises the universe. Visible matter in the universe, formed by different atoms, consists of quarks and leptons. The quarks inside neutrons and protons are held together by gluons, the strong force mediator. The electrons (charged leptons) are attracted by the protons through the electromagnetic field, mediated by photons, to form neutral atoms. The weak interactions between charged and neutral leptons are mediated by $W^{\pm}/Z^0$ bosons. The macroscopic motion and clustering of matter is governed by gravity, including the orbits of gravitationally bound systems in the universe. The fundamental origin of mass of fundamental particles is explained by the Higgs mechanism [31]. Quarks, leptons, intermediate vector bosons, and the Higgs bosons form the Standard Model (SM) in particle physics. The consistency between the theoretical prediction and experimental results demonstrates impressive success for the SM. But just like other theories, there are still phenomena beyond the prediction of the SM.

In 1933, the Swiss astronomer Fritz Zwicky discovered the abnormal velocity dispersion of galaxies on the edge of the Coma galaxy cluster. The contradiction between the observed galaxy motion and the mathematical evaluation based on the expected gravity of luminous material in the galaxies of the cluster he proposed as an effect due to invisible (“dark”) matter at a large scale, coining the term “dark matter”. The existence of the dark matter is proved by variety of astrophysical observations, and the concept of dark matter is now widely accepted by the scientific community. The astronomical observation of the dark matter phenomenon indicates that dark matter interacts with luminous matter only gravitationally plus possibly through the weak interaction, which no SM particle can do, and makes identifying the nature of dark matter notoriously difficult. The weakly interacting massive particles (WIMPs) [32] as a promising candidate of dark matter particles have been searched for decades in the underground labs [33, 34, 35] because the low cosmic ray background in the underground labs is needed to achieve the required sensitivity. To date no uncontested evidence has been found that dark matter can be accounted for by WIMPs. This has brought to the fore the possibility that other weakly interacting particles may also be candidates for the dark matter.

Another phenomenon beyond the prediction of the SM is neutrino oscillation. The SM contains only (right-) left-handed (anti-) massless neutrinos, but the observed phenomenon of neutrino oscillation requires that neutrinos be massive. The discovery of neutrino oscillations started from the observation of the solar neutrino deficit, in experiments by R. Davis, Jr and J. N. Bahcall in the Homestake experiment in the 1960s [36]. Neutrino oscillation [37] was proposed to explain the discrepancy between the observed solar neutrino flux in the Homestake experiment and the theoretical prediction from the nuclear fusion reaction energy production in the Sun. Direct evidence of neutrino oscillation was experimentally acquired by the Super-Kamiokande Observatory [12] and the Sudbury Neutrino Observatories [13]. The later long base line neutrino experiment [38] and the Daya bay experiment [39], et al., confirmed the experimental results from the Super-Kamiokande Observatory and the Sudbury Neutrino Observatories. The theory for explaining neutrino oscillation postulates that each neutrino flavor eigenstate (ν_e, ν_ν, ν_τ) is a coherent superposition of different mass eigenstates, as discussed above in Section. 1.2. The transformation of neutrino flavors due to dephasing from the Heisenberg oscillations during propagation explains the deficit of solar neutrinos observed on Earth. The upper limit of the sum of three neutrinos' mass eigenvalues estimated by current neutrino experiments is around 0.5 eV [21, 22]. Explaining this tiny neutrino mass with the Higgs mechanism requires that the Yukawa coupling constant of neutrinos to the Higgs be at least six orders of magnitude smaller than the Yukawa coupling constants of other fermions, which is considered "unnatural" and suggests some a new physics beyond the SM.

The prevailing theory explaining neutrino mass is called the "see-saw mechanism" [40], in which additional neutrino(s) must be introduced, usually (left-) right-handed (anti-) neutrino(s) lacking charged and neutral weak interactions, and coupled to known SM particles only by mixing with ordinarily active neutrinos, as discussed above in Section. 1.3. Thus, these additional (left-) right-handed (anti-)neutrinos are called "sterile" neutrinos. The neutrino flavor eigenstate is a mixture of active neutrino mass eigenstates and the sterile neutrino(s). The small mass of active neutrinos observed in neutrino oscillation can be achieved by diagonalizing the mass matrix of the mixing. There is no theory that guides us to the mass of a sterile neutrino. The keV mass range of sterile neutrinos is studied by modelers and theorists [41].

The sterile neutrino with mass in the keV/c^2 scale is also suggested [42, 32] as a possible candidate for the warm dark matter, which is a more suitable candidate than much heavier

WIMPs (cold dark matter) based on large scale structure calculations and observations [43].

In the simplest implementations, the sterile neutrino has several decay channels resulting from its mixing with active neutrinos. One such decay is visible: decay to an active neutrino and a characteristic x-ray line at half the sterile neutrino mass [40]. The observation of x-ray fluxes from galaxies, if it is from the decay of sterile neutrinos, restricts the sterile neutrino with mass between ∼1 keV - ∼20 keV, to have a mixing with the active neutrinos less than $10^{-13} \leqslant \sin^2\theta \leqslant 10^{-7}$. The Feynman diagram of the radiative decay of a sterile neutrino is shown in Fig. 2.1. The energy of the photon produced in the decay is $m_s/2$ because of energy and momentum conservation. Considering that the sterile neutrino is a candidate for warm dark matter, the decay of the sterile neutrino in the astronomical scale would add a characteristic x-ray peak to the x-ray background spectrum from the cosmology observations. The recent observation of an unexplained 3.5 keV x-ray peak, if from the sterile neutrino decay, would correspond to sterile neutrinos with mass of 7 keV [44].

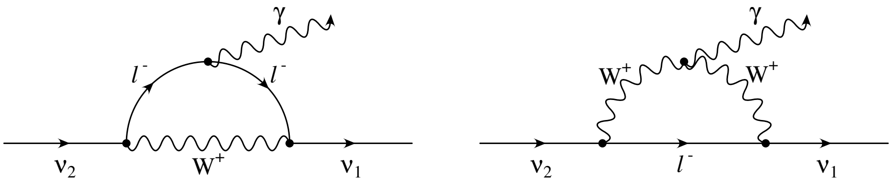

Figure 2.1: Radiative decay channel of sterile neutrino ν_2 in the mass eigenstate, with ν_1 representing the active neutrino produced in the decay. From Fig. 2 of Ref. [45]

The lifetime of a sterile neutrino is required to be longer than the age of the universe if it is to make up the present day dark matter. The lifetime is dominated by an invisible decay into three neutrinos, and can be calculated from Eq. 2.1 [45, 23]

$$\Gamma_\gamma \approx 6.8 \times 10^{-33} s^{-1} (\frac{\sin^2 2\theta}{10^{-10}})(\frac{m_s}{1\text{keV}})^5 \tag{2.1}$$

where Γ_γ is the decay rate of a sterile neutrino. The lifetime consideration defines a line in the m_ν vs. $\sin^2\theta$ plane above which sterile neutrino dark matter is not possible.

The limits provided by astronomical x-ray observations with assumed contributions of sterile neutrinos as dark matter are shown in orange in Fig. 2.2. Laboratory limits of the sterile neutrino mass vs. the mixing between sterile neutrinos and active neutrinos from β decay are shown in red and green in Fig. 2.2. All but two of them were "kink searches", seeking the evidence of sterile neutrinos from the deviation of the ordinary β decay energy spectrum caused by the sterile neutrinos.

In addition to solving the dark matter and neutrino oscillation problems, understanding

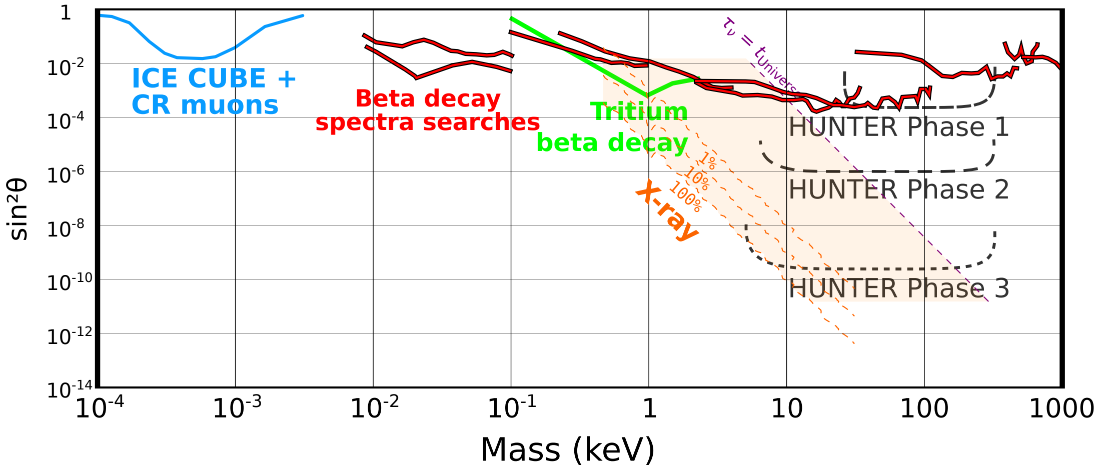

Figure 2.2: Limits on sterile neutrino coupling strength vs. mass over a wide mass range. Full lines from laboratory experiments: the limits provided by the β decay searches are in red, as summarized in Ref. [46]; blue curve is from the Ice Cube experiment [47]; the limits provided by electron energy spectra of the tritium decays are shown in green [48, 49]. Dashed lines (orange) show astrophysical limits permitting sterile neutrinos to be the galactic dark matter, from Fig. 57 of Ref. [50, 51]. These are from the non-observation of sterile neutrino decay x-rays from dark matter dominated objects, assuming 100%, 10%, 1% of the dark matter is sterile neutrinos of a single mass. Black dashed curves show projected HUNTER Phase 1 (proposed here) and possible future upgrades, which would check or surpass the astrophysical limits.

sterile neutrinos also gives the ability to solve other outstanding problems in physics, notably the baryon-antibaryon asymmetry.

2.2 HUNTER Experiment

The new physics beyond the SM, related to sterile neutrinos, brings together researchers in different fields from Temple University, UCLA, University of Houston and Princeton University in designing the HUNTER (**H**eavy **U**nseen **N**eutrinos from **T**otal **E**nergy-momentum **R**econstruction) experiment to search for sterile neutrinos in the 20-300 keV$/c^2$ mass range using energy-momentum conservation, based on the electron capture (EC) decay of ^{131}Cs in the laboratory.

The concept of the HUNTER experiment is shown in Fig. 2.3. The main apparatus consists of an ion and an electron spectrometer on opposite sides of the chamber, and a **M**agneto **O**ptical **T**rap (MOT) [52, 53, 54] system at the center of the chamber. ^{131}Cs atoms are suspended at the center of the chamber between the ion and the electron spectrometers by the MOT. The EC decay of ^{131}Cs produces an x-ray, a ^{131}Xe ion, Auger electrons, and a neutrino. These products are all detected by different detectors, except the neutrino.

Four x-ray detectors of YAP scintillator panels [55] with dimensions of 250 mm × 250 mm are deployed azimuthally around the MOT to detect the atomic x-ray signal from the ^{131}Cs decay.

The signal is read out by silicon photomultiplier (SiPM) pixel arrays with a time resolution of ∼0.8 ns and a spatial resolution of ∼50 µm. The YAP panels are placed 400 mm away from the MOT, which provides a satisfactory angular resolution in the x-ray momentum reconstruction. The expected energy resolution of the x-ray detector (∼1 keV) is sufficient to identify K-capture x-rays refilling from the M and N shells, but may be only marginally sufficient to distinguish the desired K-capture, N-refilling line at 34.43 keV from a 33.63 keV K-capture, and M-refilling x-ray. The x-ray detector will be placed in a re-entrant flange with a thin aluminum window of 125 µm because the scintillator panels and their front-end electronics are not compatible with the ultra high vacuum (UHV) of 10^{-10} Torr of the inside chamber required by the MOT. The aluminum window will attenuate the x-rays by 3%.

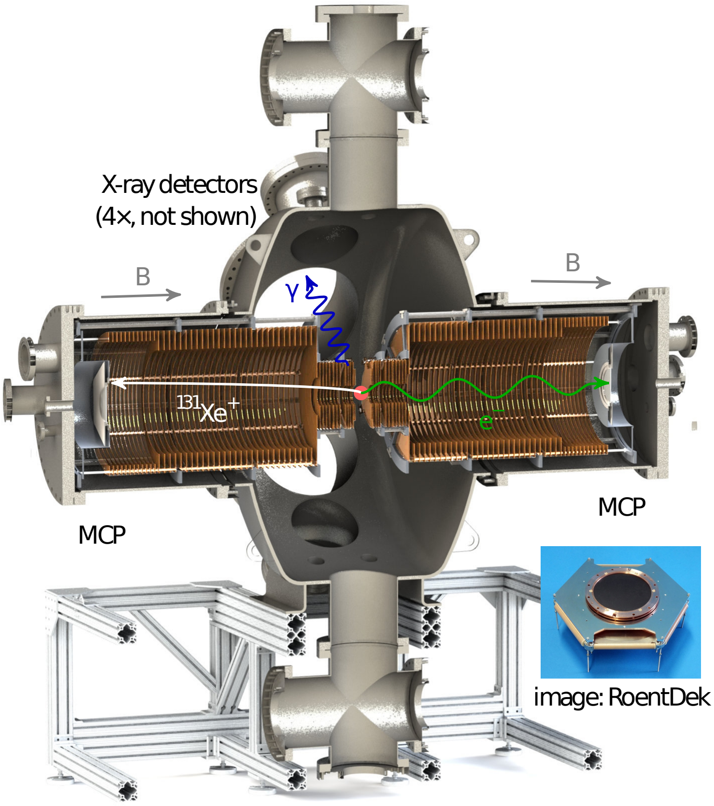

Figure 2.3: Scheme of the HUNTER apparatus. The spectrometer situated on left (right) side is for ion (Auger electron). The upper port is for pushing ^{131}Cs atoms to the MOT.

^{131}Xe ions are produced as the recoil nucleus following electron capture decays of ^{131}Cs. These are collected in 4π solid angle and accelerated to the ion detector by an electric field. Times of flight and impact positions of ions are measured by a z-stack microchannel plate (MCP) [56] placed 930 mm away from the MOT, with a time resolution of ∼0.3 ns and a spatial resolution of ∼50 µm [57]. The voltage of the front MCP stack is biased at -2500 V to achieve a high detection efficiency [58, 59], which is much higher than the potential of the first electrode facing the ion MCP. A woven mesh at the same potential as the first electrode is clamped to the electrode to stop the potential lines of the MCP from penetrating into the ion spectrometer. The simulated ion momentum resolution is ∼0.4 keV. Details of the ion spectrometer design are given in Chapter. 3.

Auger electrons are accelerated to the electron spectrometer by a uniform electric field of ∼0.4 V/mm in longitudinal direction. The transverse motion of the electron is confined by an 8 G uniform magnetic field generated by the solenoids outside the chamber. The structure of the ion and electron spectrometers are generally identical to allow the option of interchanging them for debugging purposes. The electron MCP is biased at ∼400 V to achieve the highest electron detection efficiency. A Woven mesh is not required for the electron spectrometer because the biased voltage of the electron MCP is comparable with the potential of the electrode facing it. The absence of an accelerating mesh in the electron spectrometer also improves the transmission of electrons. The electron collection efficiency is more complicated than that of the ions, All of the electrons in the energy range corresponding to two-Auger events are collected, while only 56% of single-Auger electrons with higher energies are collected. The current achieved momentum resolution for electrons is ∼0.1 KeV.

Assuming that the decaying ^{131}Cs was at rest, reconstruction of the momenta of the ^{131}Cs decay products allows the neutrino's 4-momentum, and hence the mass of the undetected neutrino, to be reconstructed. If the electron neutrino produced in the EC decay is mixed with a massive eigenstate in the sensitive range, a separate peak centered at a nonzero mass in the reconstructed mass spectrum will be discovered, as shown in Fig. 2.4.

Fig. 2.4 is a cartoon of the mass-squared spectrum of neutrinos of ^{131}Cs decays in the case that a sterile neutrino does exist. The first peak centered at zero corresponds to the decay events emitting active neutrinos. The peak at (60 keV/c^2)^2 corresponds to the decays emitting sterile neutrinos. The full width at half maximum of the peaks depend on the reconstruction resolution of the decay product momenta.

2.2.1 Choice of ^{131}Cs as Decay Source for HUNTER

In the HUNTER experiment, ^{131}Cs atoms are proposed to be trapped and suspended at the center of the apparatus by laser beams. The current technique of MOT is able to cool the ^{131}Cs to 20 µK, with 10^9 ^{131}Cs atoms in the cloud [60]. For the Phase 1 HUNTER experiment, 10^8 ^{131}Cs atoms will be trapped in a spherical cloud with the diameter of ∼2 mm. Trapping a larger

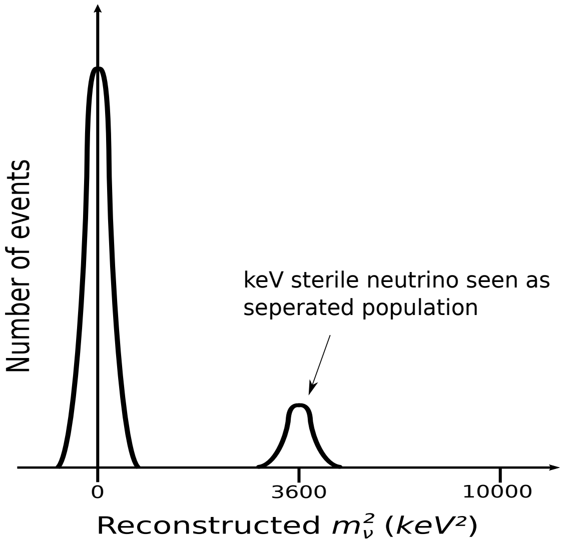

Figure 2.4: A cartoon of the reconstructed mass-squared spectrum of neutrinos in HUNTER, showing a separated population of events corresponding to production of a 60 keV$/c^2$ neutrino.

number of atom is possible [61] for the future upgrades of the HUNTER experiment.

The short half life of ^{131}Cs decays, 9.7 days, makes it possible to obtain enough reconstructed events for meaningful statistics in a reasonable time. The overall number of expected decay events in a complete one year running time is $\sim 2.1 \times 10^5$ as discussed in Chapter. 9. The ^{131}Cs decay is 100% EC, which makes it a suitable source for neutrino experiments. There is no energetic electron emitted as in $\beta^{\pm}$ decays, only a neutrino and a ^{131}Xe* with a vacancy in the inner shell of the atom. The ^{131}Xe* will de-excite in ~1 ps [62] and produce an x-ray, a ^{131}Xe ion and Auger electrons. The decay sequence is shown in Fig. 2.5.

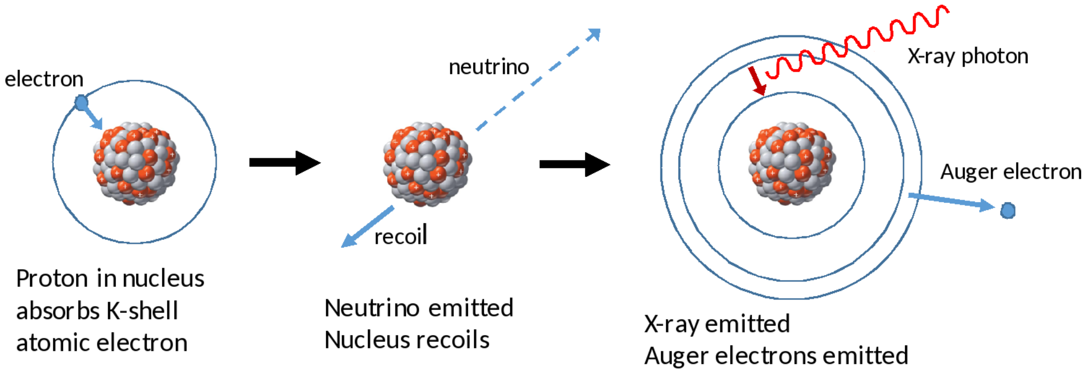

Figure 2.5: Decay sequence of ^{131}Cs

The EC decay of ^{131}Cs has been carefully studied for the HUNTER experiment (see e.g. Ref. [63]), including details of the capture orbit and the specific x-rays and Auger electrons emitted. X-ray emission from the K, L, M shell electron capture are presented in Table. 2.1. The x-ray from the refilling of the vacancy in the inner shell due to the electron capture serves as the start signal for the measurement of the time of flight (TOF) of the charged decay products.

As shown in Table 2.1, the K shell electron capture is the dominant decay channel, which generates a neutral ^{131}Xe atom in the electronically excited state having a vacancy in the K shell. The K shell vacancy refilling from the N2 or N3 shell is chosen for the HUNTER Phase 1 experiment. The energy of the x-ray generated in this process is calculated from the ^{131}Xe atomic energy levels [64]. The energies of emitted electrons are determined by the average of the energy levels of ^{131}Cs and ^{131}Xe [65] as shown in Table. 2.2

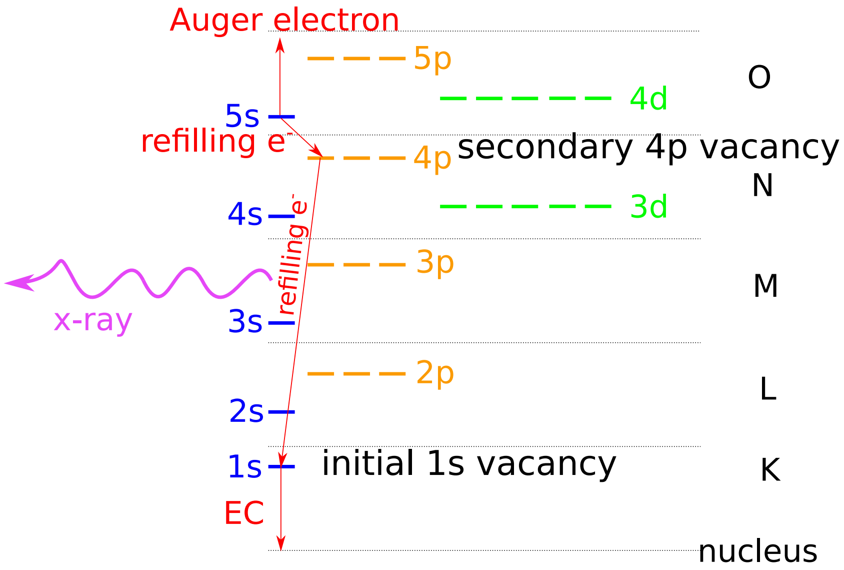

Figure 2.6: Illustration of the K shell electron capture with emission of an x-ray from the N shell refilling.

The vacancy left in the higher shell after the x-ray emission will be refilled from other higher shells, which results in the emission of Auger electrons. Auger emission transitions are specified by a specialized notation. The N2O1O1 refilling process is shown in Fig. 2.6. In this process, the K shell vacancy is refilled by a N2 shell electron, accompanied with the emission of a characteristic x-ray. The N2 shell vacancy is then refilled by an O1 shell electron, with the released binding energy appearing as emission of the other O1 shell electron instead of a photon. Other refilling processes may result in producing two or more Auger electrons. In the Phase 1 HUNTER experiment, only the K-shell EC followed by N-shell x-ray emission will be considered in the data analysis, because of the low Auger multiplicity (only 1 or 2 per decay) and the lowest Auger energies. These features of the decay are necessary to achieve efficient and precise reconstruction in a HUNTER-style experiment.

The branching ratio of the refilling channel is computed by assuming that each electron sublevel has an equal probability of transition. So, the multiplicity (number of refilling channel) of the N2O1O1 refilling process is $2 \times 2 \times 1 = 4$. The probability of emitting single Auger in a

	electron captured from shell		
	K	L	M
	85%	12.5%	2.5%
x-rays from shell			
L	69.5%		
M	13.0%	10.0%	
N	2.5%	2.5%	2.5%
x-ray energy range (keV)			
L	29.46 - 29.78		
M	33.56 - 33.63	4.32 - 4.45	
N	34.43	5.32	0.87
Auger ranges from N shell (keV)			
type NNO	0.02 - 0.06	0.02 - 0.06	
type NOO	0.10 - 0.12	0.10 - 0.12	

Table 2.1: Energies of x-rays and Auger electrons emitted in a ^{131}Cs decay and the corresponding branching ratios are listed in the table. The refilling channels and Auger energies are taken from Ref. [65]. The Auger "type" notation NNO and NOO are the same as N2O1O1 without specifying the electron numbers in the corresponding shells.

decay is the quotient of the multiplicity of this electron and the sum of the multiplicities of all the possible Auger electrons in a single Auger decays. The probability of the second Auger in a multiple Auger decay is a conditional probability based on the probability of the first Auger electron. The refilling processes and the associated multiplicities can be computed from the table in Ref. [65], which leads to the probability of the single and double Auger events as about 40% and 60%, respectively.

shell	population	^{131}Xe (eV)	^{131}Cs (eV)
K	2	34561	35985
L1	2	5453	5714
L2	2	5107	5359
L3	4	4786	5012
M1	2	1148.7	1211
M2	2	1002.1	1071
M3	4	940.6	1003
M4	4	689	740.5
M5	6	676.4	726.6
N1	2	213.2	232.3
N2	2	146.7	172.4
N3	4	145.5	161.3
N4	4	69.5	79.8
N5	6	67.5	77.5
O1	2	23.3	22.7
O2	2	13.4	14.2
O3	4	12.1	12.1

Table 2.2: Table shows the energy levels of ^{131}Cs and ^{131}Xe [66]

2.3 ^{131}Cs Decay Kinematics

In the HUNTER experiment, the precisions required for the different measurements in order to attain a desired missing mass resolution can be understood from the kinematics of the ^{131}Cs decay. The ^{131}Cs decay sequence is shown in Eq. 2.2

$$\begin{aligned} {}^{131}Cs &\rightarrow {}^{131}Xe^{*} + \nu \\ {}^{131}Xe^{*} &\rightarrow \begin{cases} {}^{131}Xe^{+} + e^{-} + \gamma \\ \\ {}^{131}Xe^{2+} + 2e^{-} + \gamma \end{cases} \end{aligned} \tag{2.2}$$

here the $^{131}Xe^{*}$ is electronically excited, having a 1s vacancy. For ^{131}Cs atoms trapped at 20 µK [60], the associated kinetic energy is $\sim k_B T \approx 1.7 \times 10^{-9}$ eV. The four-momentum of ^{131}Cs can be written as $p_{Cs} = (m_{Cs}, 0, 0, 0)$ assuming the atoms decay at rest. The four-momentum of ^{131}Xe* and neutrino can be written as Eq. 2.3 considering momentum conservation.

$$\begin{aligned} p_{Xe^{*}} &= \left(\sqrt{m_{Xe^{*}}^{2} + |\mathbf{P}_{\nu}|^{2}}\ ,\quad -\mathbf{P}_{\nu}\right) \\ p_{\nu} &= \left(\sqrt{m_{\nu}^{2} + |\mathbf{P}_{\nu}|^{2}}\ ,\quad \mathbf{P}_{\nu}\right) \end{aligned} \tag{2.3}$$

We consider the case when $^{131}Xe^{*}$ de-excites by emission of a K x-ray followed by one Auger electron. The four-momenta of de-excitation products of ^{131}Xe* are

$$\begin{aligned} p_{Xe^{+}} &= \left(\sqrt{m_{Xe^{+}}^{2} + |\mathbf{P_{Xe^{+}}}|^{2}}\ ,\quad \mathbf{P_{Xe^{+}}}\right) \\ p_{e^{-}} &= \left(\sqrt{m_{e^{-}}^{2} + |\mathbf{P_{e^{-}}}|^{2}}\ ,\quad \mathbf{P_{e^{-}}}\right) \\ p_{\gamma} &= \left(|\mathbf{P}_{\gamma}|\ ,\quad \mathbf{P}_{\gamma}\right) \end{aligned}$$

According to four-momentum conservation, we have

$$p_{Cs} = p_{\nu} + p_{Xe^{+}} + p_{e^{-}} + p_{\gamma} \tag{2.4}$$

Rearranging Eq. 2.4 and applying the rule of scalar product to calculate the mass square of the neutrino:

$$
\begin{aligned}
m_\nu^2 &= (p_{Cs} - p_{Xe^+} - p_{e^-} - p_\gamma)^2 \\
&= m_{Cs}^2 + m_{Xe}^2 + m_e^2 - 2m_{Cs}\left(\sqrt{m_{Xe^+}^2 + |\mathbf{P}_{\mathbf{Xe}^+}|^2} + \sqrt{m_{e^-}^2 + |\mathbf{P}_{\mathbf{e}^-}|^2} + |\mathbf{P}_\gamma|\right) \\
&\quad + 2\left(\sqrt{m_{Xe^+}^2 + |\mathbf{P}_{\mathbf{Xe}^+}|^2}\sqrt{m_{e^-}^2 + |\mathbf{P}_{\mathbf{e}^-}|^2} + |\mathbf{P}_\gamma|\sqrt{m_{Xe^+}^2 + |\mathbf{P}_{\mathbf{Xe}^+}|^2} + |\mathbf{P}_\gamma|\sqrt{m_{e^-}^2 + |\mathbf{P}_{\mathbf{e}^-}|^2}\right) \\
&\quad - 2(\mathbf{P}_{\mathbf{Xe}^+}\mathbf{P}_{\mathbf{e}^-} + \mathbf{P}_{\mathbf{Xe}^+}\mathbf{P}_\gamma + \mathbf{P}_{\mathbf{e}^-}\mathbf{P}_\gamma) \\
&= m_{Cs}^2 + m_{Xe}^2 + m_e^2 - 2m_{Cs}\left(\sqrt{m_{Xe^+}^2 + |\mathbf{P}_{\mathbf{Xe}^+}|^2} + \sqrt{m_{e^-}^2 + |\mathbf{P}_{\mathbf{e}^-}|^2} + |\mathbf{P}_\gamma|\right) \\
&\quad + \left[\left(\sqrt{m_{Xe^+}^2 + |\mathbf{P}_{\mathbf{Xe}^+}|^2} + \sqrt{m_{e^-}^2 + |\mathbf{P}_{\mathbf{e}^-}|^2} + |\mathbf{P}_\gamma|\right)^2 - (m_{Xe}^2 + |\mathbf{P}_{\mathbf{Xe}^+}|^2) - (m_e^2 + |\mathbf{P}_{\mathbf{e}^-}|^2) - |\mathbf{P}_\gamma|^2\right] \\
&\quad - 2(\mathbf{P}_{\mathbf{Xe}^+}\mathbf{P}_{\mathbf{e}^-} + \mathbf{P}_{\mathbf{Xe}^+}\mathbf{P}_\gamma + \mathbf{P}_{\mathbf{e}^-}\mathbf{P}_\gamma) \\
&= \left(m_{Cs} - \sqrt{m_{Xe^+}^2 + |\mathbf{P}_{\mathbf{Xe}^+}|^2} - \sqrt{m_{e^-}^2 + |\mathbf{P}_{\mathbf{e}^-}|^2} - |\mathbf{P}_\gamma|\right)^2 - (\mathbf{P}_{\mathbf{Xe}^+} + \mathbf{P}_{\mathbf{e}^-} + \mathbf{P}_\gamma)^2 \\
&\approx (m_{Cs} - m_{Xe^+} - m_{e^-} - E_{Xe^+} - E_{e^-} - E_\gamma)^2 - (\mathbf{P}_{\mathbf{Xe}^+} + \mathbf{P}_{\mathbf{e}^-} + \mathbf{P}_\gamma)^2
\end{aligned}
\tag{2.5}
$$

where E_{Xe^+}, E_{e^-} and E_γ are the kinetic energies of Xe^+, e^- and x-ray, respectively. The last line neglects the high order terms of the Taylor expansions of $\sqrt{m_{Xe^+}^2 + |\mathbf{P}_{\mathbf{Xe}^+}|^2}$ and $\sqrt{m_{e^-}^2 + |\mathbf{P}_{\mathbf{e}^-}|^2}$. Only one Auger electron is included in the derivation, but the derivation for the decay producing two Auger electrons is similar.

The standard tabulated nuclear Q value is defined as

$$Q = m_i - m_f = m_{Cs} - m_{Xe} - m_\nu \tag{2.6}$$

where m_i (m_f) represents the total mass of the neutral atoms before (after) the nuclear interaction. m_{Cs} and m_{Xe} are the atomic masses of ^{131}Cs and ^{131}Xe in their ground states, respectively. Eq. 2.5 can be further simplified by ignoring the small terms in the first parenthesis given that $E_{Xe^+} + E_{e^-} + E_\gamma \approx 34.5$ keV if the energy of x-ray from N-shell refilling is considered in the calculation, is only one tenth of $(m_{Cs} - m_{Xe}) \approx (m_{Cs} - m_{Xe^+} - m_{e^-}) \approx 355$ keV [67, 68, 69]. Thus, Q is a constant under this approximation.

$$m_\nu^2 \approx Q^2 - (\mathbf{P}_{\mathbf{Xe}^+} + \mathbf{P}_{\mathbf{e}^-} + \mathbf{P}_\gamma)^2 \tag{2.7}$$

For the decay producing massless neutrino, we have

$$|\mathbf{P}_\nu| = |\mathbf{P}_{\mathbf{Xe}^+} + \mathbf{P}_{\mathbf{e}^-} + \mathbf{P}_\gamma| = Q \tag{2.8}$$

The variation of the mass square of neutrino in the presence of uncertainty can be approximately written as Eq. 2.9 by ignoring the angle between $\mathbf{P}_\nu$ and $d\mathbf{P}_\nu$

$$\begin{aligned} \delta m_\nu^2 &\approx 2 \cdot |\mathbf{P}_{\mathbf{Xe}^+} + \mathbf{P}_{\mathbf{e}^-} + \mathbf{P}_\gamma| \cdot dP \\ &= 2 \cdot Q \cdot dP \end{aligned} \tag{2.9}$$

where dP is the magnitude of the total reconstruction precision of the secondary particles.

To achieve the desired low limit of the sterile neutrino mass in HUNTER, the required momentum resolution is

$$dP = \delta m_\nu^2 / (2 \cdot Q) \approx 0.6 \text{ keV} \tag{2.10}$$

CHAPTER 3

THE HUNTER ION SPECTROMETER

Reaction **I**on **M**icroscopes (RIMs) are axial-field electrostatic spectrometers extensively used in atomic physics to study few-body reactions [70]. The high resolution and 4π solid angle acceptance achievable with these devices have made them essential tools for studies in atomic physics. The sources of reacting particles in such studies are often spatially extended MOT (or supersonic gas jets), requiring the spectrometers to focus in both the longitudinal and transverse directions to avoid a loss of resolution. The necessary design conditions for combining longitudinal (Wiley-McLaren) [71] and transverse focusing have been described in the literature and are employed by a number of chemical physics groups. However, a unified and systematic framework for optimizing the several competing requirements for such spectrometers has not been described.

This chapter describes such a framework, developed to design the HUNTER electrostatic spectrometer. A multi-step optimization procedure in which the *lua* programming language directing particle tracking with the **SIMION** package is applied. Using this technique to optimize the spectrometer design, a design has been achieved for ^{131}Xe recoils from ^{131}Cs decays with a simulated recoil momentum resolution of $\sim$0.4 keV$/c$. The simulated Auger momentum and x-ray resolutions of the HUNTER apparatus are $\sim$0.1 keV$/c$ and $\sim$0.03 keV$/c$, respectively.

3.1 Wiley-McLaren Spectrometer

The resolution of a time of flight spectrometer is obviously limited by variations of the flight path length if the source of particles is spatially extended along the direction of travel. The concept of “time focusing” to improve the longitudinal momentum ($p_{\|}$) resolution for spectrometers with longitudinally extended sources was introduced by Wiley and McLaren [71] in 1955. In this time-focusing spectrometer design, a uniform electric field region is followed by a field free drift region as shown in Fig. 3.1. Charged particles starting at different positions traverse the field region in different TOF, which can be compensated by the TOF of the charged particles traversing the drift region, if a 2:1 length ratio of drift region and field region is chosen.

The total TOF of charged particles passing through the field region with length s and the

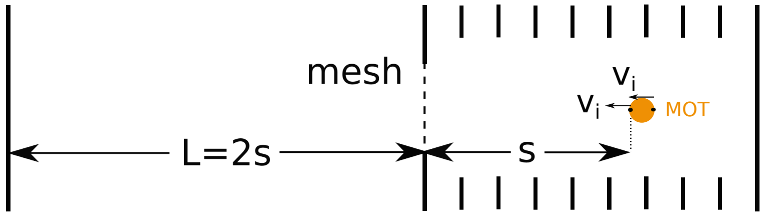

Figure 3.1: An illustration of the Wiley-McLaren model for producing a time-focusing spectrometer. Particles emitted from the extended MOT are accelerated by a uniform electric field over the region with MOT located.

drift region with length L is

$$t = t_1 + t_2 = \frac{v_f - v_i}{a} + \frac{L}{v_f} \tag{3.1}$$

where t_1 is the TOF in the field region, t_2 is the TOF in the drift region. a is the acceleration of the particles in the field region. v_i is the longitudinal component of the initial velocity. $v_f = \sqrt{v_i^2 + 2as}$ is the speed when the charged particles depart the field region. The ratio of L/s for achieving time focusing can be computed by setting the derivative of t with respect to s to zero

$$\frac{\partial t}{\partial s} = \frac{-aL}{(2as + v_i^2)^{3/2}} + \frac{1}{\sqrt{2as + v_i^2}} = 0 \tag{3.2}$$

which gives $L = (2as + v_i^2)/a \approx 2s$ since v_i^2/a is a small term.

The calibration relation between TOF and $p_{\|}$ can also be derived by taking derivative of t with respect to v_i

$$\begin{aligned} \frac{\partial t}{\partial v_i} &= \frac{v_i}{a\sqrt{2as + v_i^2}} - \frac{1}{a} - \frac{v_i L}{(2as + v_i^2)^{3/2}} \\ &\approx \frac{1}{a}(\frac{v_i}{\sqrt{2as}} - 1) - \frac{v_i L}{(2as)^{3/2}} \\ &\approx -\frac{1}{a} \end{aligned} \tag{3.3}$$

where $v_i^2 << 2as$ is used in simplifying Eq. 3.3. This result has both favorable and unfavorable implications. The TOF is highly linear in initial velocity, which is favorable. However, the slope (and hence the resolution for fixed timing resolution) is inversely proportional to the accelerating field strength. Very weak fields (i.e. very high resolution) are mechanically and electrically difficult to produce.

3.2 Transverse-Focusing Spectrometer

Given that the MOT cloud is also extended in the transverse direction, high resolution spectrometer design requires to focus the ions emitted in the transverse direction with the same initial momentum. This transverse-focusing spectrometer is achieved by introducing an electrostatic lens [72] as shown in Fig. 3.2.

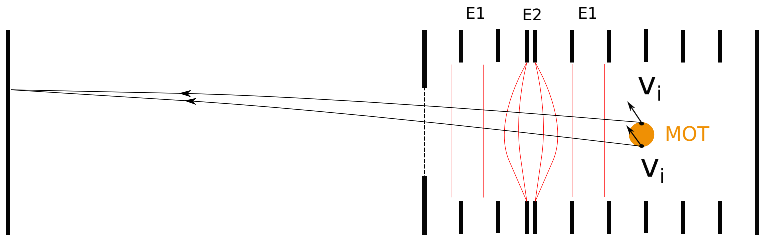

Figure 3.2: An illustration of the transverse focusing spectrometer with an electro-static lens. The red lines are the equipotential lines of the electric fields. E1 and E2 are the electric fields for producing the electrostatic lens, where E2 $>$ E1.

The transverse-focusing spectrometer consists of a field region and a drift region. In the field region, there should be at least two electric fields with different values to form an electrostatic lens. In Fig. 3.2, the pair of electrodes with small gap is for producing a strong electric field E2. The electric field E1 formed by the electrodes on each side of E2 should be weaker than E1, so that the equipotential lines of E1 and E2 form a lens shape.

Particles passing through the electrostatic lens at different radii have different transverse momentum kicks because of different ratios of longitudinal and transverse components of the electric field. The ions passing through the lens region far away from the central axis will experience a weaker transverse component of the electric field than the paraxial ions, and depart the lens with smaller transverse velocities than the paraxial ones. The difference of the transverse velocity gives rise to spatial focusing when they depart the lens.

The impact radius (IR) of the ion at the ion MCP detector turns out to be linearly dependent on transverse momentum ($p_\perp$) of the charged particle since IR is determined by the constant-speed transverse displacement over the flight path after the lens.

3.3 HUNTER Double-Focusing Spectrometer

The Wiley-McLaren configuration usually incorporates a grid to separate a uniform field "extraction region" from the field-free drift region. In HUNTER, use of a field-delimiting grid would be undesirable, because it would interfere with at least one of the trapping laser beams.

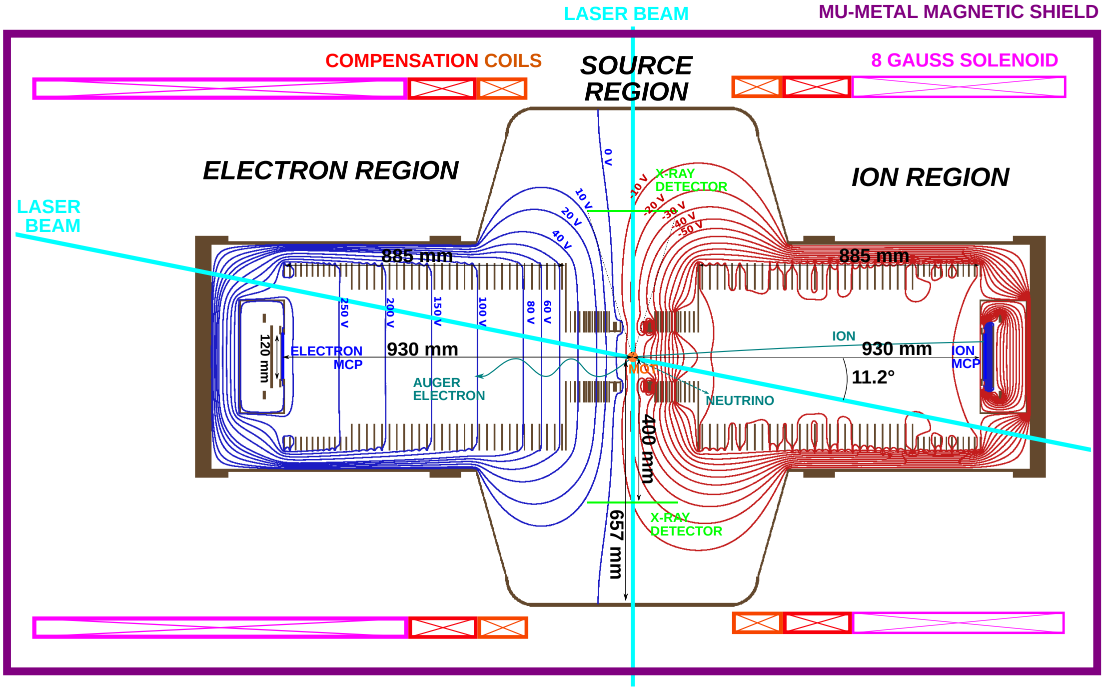

Figure 3.3: Plan view of the HUNTER apparatus, not to scale. Tracks for electrons (helical track heading to the left) and ions (heading to the right) are schematically shown, originating from the MOT (red ball at the center). Red and blue contours are optimized equipotentials simulated using SIMION with contour interval labeled in the figure.

Additionally, the pure Wiley-McLaren design has no transverse focusing to improve the $p_\perp$ resolution ($\delta p_\perp$) in the presence of a transversely extended particle source. RIMS measure $p_\perp$ from the radial IR of particles at the end of the flight path. Clearly, this would limit the resolution unless there is transverse focusing of the preceding section as well as the longitudinal focusing. Given the anticipated extension of the MOT, with a radius of 1 mm in HUNTER, transverse focusing is necessary to achieve the required momentum resolution. Therefore, HUNTER needs a gridless, double-focusing configuration, as has been previously described in Refs. [73, 74, 75].

The spectrometer layout arrived at after a lengthy design process to satisfy the HUNTER requirements is shown in Fig. 3.3. The key dimensions are marked in the drawing. Equipotential lines corresponding to the final optimized potentials are drawn to show the final electrostatic configuration. Three MOT laser beams pass through the source region, each with a keep-out diameter of 60 mm. Two beams are shown in light blue, while the third beam is perpendicular to the plane of the figure and is not shown. The rectangular red and magenta boxes outside the vacuum chamber represent solenoids to generate the magnetic field needed for the Auger electron spectrometer.

In general, the spectrometer consists of three major sectors: the ion arm (right half in Fig. 3.3), the electron arm (left half), and the central source region containing the MOT, which is common to both spectrometers.

The ion spectrometer sector contains 42 annular electrodes with an outer radius of 248 mm. The first one, which is closest to the common source region, has an inner radius of 66 mm. The inner radii of subsequent electrodes increase stepwise to accommodate the tilted laser beam. The last electrode before the MCP ion detector has an inner radius of 60 mm, matching the radius of the active region of the MCP. Technical limitations required the use of a 1 mm thickness for all electrodes in the simulations, although the actual electrode thicknesses are 0.3 mm and 0.6 mm for electrodes in the common source region and the ion arm, respectively.

The configuration of the electron spectrometer is identical to that of the ion spectrometer. However, the electric field in the electron spectrometer is not a double-focusing design, because of complications presented by the axial magnetic field, needed to confine the electron trajectories within the 60 mm MCP detector radius. The resulting degradation of the electron momentum resolution is tolerable in HUNTER because the electron momenta are much smaller than the ions', and therefore do not contribute as much to the neutrino mass resolution.

The source sector consists of 30 annular electrodes with an outer radius of 120 mm, 4 annular electrodes with an outer radius of 91 mm, plus 4 electrodes with an L shaped cross-section needed to form the MOT coil holders, as shown in Fig. 3.4. The inner radii of electrodes in this region are 66 mm. The smaller outer radii of electrodes on two sides of the MOT are necessary to provide adequate clearance for x-rays emitted in the ^{131}Cs decay. Near the end of the source region, toward the MCP side, a pair of electrodes separated by 2 mm, marked in the Fig. 3.4, are used on the ion side to produce the electrostatic lens, described in the preceding subsection. The two pairs of L-shaped electrodes in mirror symmetry within the source sector are the holders of anti-Helmholtz coils for generating a quadrupole magnetic field that is required by the MOT [74]. Fan sections are cut off from the coil holders and the electrode is sandwiched between them to suppress the eddy current produced in these electrodes. Given the floating potentials of the MOT coils, the coil holders and the electrode between them are grounded. The design of the electrodes can be found in Appendix A.

The full ion spectrometer consists of three field regions. The "extraction region" is a uniform field region in the source sector, which is common to both the electron and ion spectrometers. Following the extraction region, ions enter a non-uniform field region within the source sector, which acts as an electrostatic lens. This produces the transverse focusing. The ion sector follows, which is essentially a "drift region" with a tailored low field, fine-tuning the trajectories and bringing the particles to impact on the MCP.

As previously stated, the ion spectrometer must be simultaneously "time focusing" in the

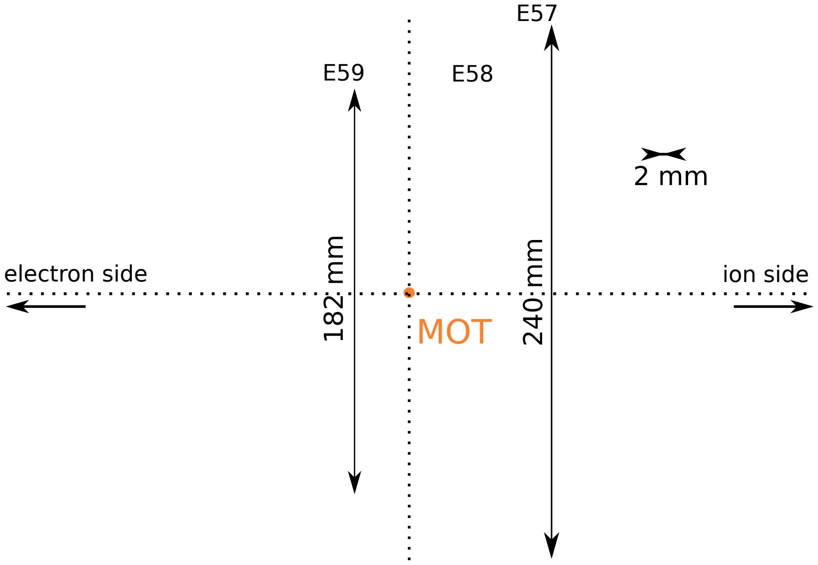

Figure 3.4: Enlarged view of the source region of the spectrometer. Voltage settings for the electrodes labeled E55-57 will be described in Section. 3.5.1. Electrodes E48 and E49 with a gap of 2 mm generate the electrostatic lens needed for transverse (spatial) focusing.

longitudinal direction and “spatially focusing” in the transverse direction. The time focus condition is that particles with a given initial $p_{\|}$, but originating at different axial positions, have the same TOF to their impact on the MCP. The transverse focus condition is that particles with a given initial $p_{\perp}$, but originating at different transverse positions, have the same IR on the MCP. Double focusing spectrometers have been described before, e.g. in Ref. [76, 74, 77, 78]. Double focusing is achieved by judicious choices of the extraction field value and length, the ratio of extraction distance to drift distance, and the electrostatic lens characteristics. In the present work, the optimization has allowed us to satisfy these conditions without the need for a grid between the “extraction region” and the “drift region”.

3.4 Estimate of Required Ion Spectrometer Resolution

For EC decay of a nucleus at rest in a laboratory, the neutrino mass can be computed from measurements of the energy and vector momenta of the final-state particles, the ionized nucleus, the atomic x-rays emitted as the EC vacancy fills, and one (for simplicity) Auger electron. Conservation of energy and momentum gives Eq. 2.5. Resolution contributions from the first parenthesis in the last line of Eq. 2.5 are very small and can be neglected, because the masses are constants and the energies are very small. Using partial differentiation and combining independent resolution contributions in quadrature yields

$$\delta(m_\nu^2) = 2|\mathbf{P}_e + \mathbf{P}_{Xe^+} + \mathbf{P}_\gamma| \times \sqrt{|\delta\mathbf{P}_e|^2\cos^2\theta_1 + |\delta\mathbf{P}_{Xe^+}|^2\cos^2\theta_2 + |\delta\mathbf{P}_\gamma|^2\cos^2\theta_3} \tag{3.4}$$

here θ_1, θ_2 and θ_3 are the angles between $(\mathbf{P}_e + \mathbf{P}_{Xe^+} + \mathbf{P}_\gamma)$ and $\delta\mathbf{P}_e$, $\delta\mathbf{P}_{Xe^+}$ and $\delta\mathbf{P}_\gamma$, respectively.

In the HUNTER experiment, the x-ray detector is placed 400 mm away from the MOT, so $\delta\mathbf{P}_\gamma$ is much smaller than $\delta\mathbf{P}_{Xe^+}$ and $\delta\mathbf{P}_e$, considering the spatial resolution of the x-ray detector. The HUNTER Q value (^{131}Cs) is $Q = (m_{Cs} - m_{Xe} - m_\nu) \approx (m_{Cs} - m_{Xe^+} - m_e - m_\nu)$, which is 355.4 keV [68] for a zero neutrino mass. Only the decay emitting a 34.4 keV x-ray will be considered in the Phase 1 HUNTER experiment. Therefore, $-\mathbf{P}_\nu = \mathbf{P}_e + \mathbf{P}_{Xe^+} + \mathbf{P}_\gamma \approx 321$ keV, considering the kinetic energies of the x-ray, Xe$^+$, and Auger electron. Eq. 3.4 can be re-written as

$$\delta(m_\nu^2) = 642\sqrt{|\delta\mathbf{P}_e|^2\cos^2\theta_1 + |\delta\mathbf{P}_{Xe^+}|^2\cos^2\theta_2} \tag{3.5}$$

Assuming for purposes of estimation, that $|\delta\mathbf{P}_e|$ and $|\delta\mathbf{P}_{Xe^+}|$ have the same value, the average of $\cos^2\theta_1$ and $\cos^2\theta_2$ are 0.5. With these values, an ion momentum resolution of 0.31 keV$/c$ ($\delta p/p \sim 0.001$) is required to achieve the standard deviation of neutrino mass square of 200 (keV$/c^2$)^2. This turns out to be achievable.

3.4.1 Limits to Wiley-McLaren Time Focusing

The $p_\parallel$ resolution ($\delta p_\parallel$) is dependent on Wiley-McLaren time focusing, but there are limits to the accuracy with which time focusing can be achieved. Consider a Wiley-McLaren spectrometer (one or two acceleration regions followed by field-free drift, no lens) and let n ions be emitted with the same initial $p_\parallel$ directed along the symmetry axis toward the ion MCP, with starting positions increasingly farther from the MCP as the index n increases. Denote the flight times to the MCP as t_1, t_2, ... , t_n. The first ion experiences a shorter time of extraction-field acceleration than the last one, so the last ion has a higher velocity when it departs the field region. In the Wiley-McLaren configuration, the extraction/drift distance ratio is chosen so as to give roughly the same source-to-MCP flight times for all of these ions. Ideally, the distribution of flight times would be a delta function.

However, it can be shown that in such a spectrometer, a similar group of ions with different initial $p_\parallel$ will also have a time focus, but at a different axial positions. The difference has two

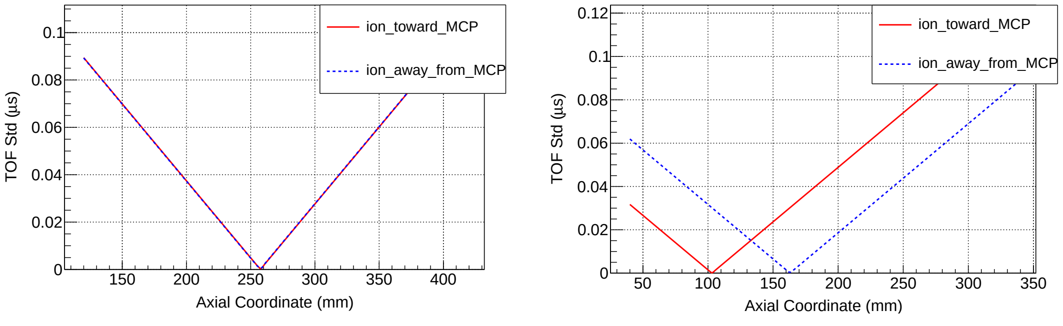

(a) (b)

Figure 3.5: (a): Flight time standard deviation vs. axial coordinate when the electric field around the MOT is uniform. The solid (dashed) line is for ions with an initial momentum toward (away from) the MCP. The electric field is 0.11 V/mm. (b): Same as (a), but for the nonuniform field at the MOT caused by the introduction of the electrostatic lens. The fringe field of the electrostatic lens changes the field at the MOT to 0.12 V/mm, with a field gradient of around 10^{-3} V/mm^2. The uniform electric field strength and the lens field strength used in this simulation are arbitrarily chosen as an example.

causes: first, the different initial $p_{\|}$ itself; second, any slight non-uniformity of the electric field at the MOT. The first reason is called chromatic aberration and there is no good way to fix it in a simple design [79]. For realistic design, this term is small compared to that resulting from field non-uniformity at the MOT.

To understand the second contribution, consider again the flight times of ions with the same initial $p_{\|}$ forward, given by t_1, t_2, ... , t_n. Ions with the same magnitude of initial $p_{\|}$, but directed away from the MCP, will have flight times $t_1 + \Delta t_1$, $t_2 + \Delta t_2$, ... , $t_n + \Delta t_n$. If $\Delta t_1 = \Delta t_2 = ... = \Delta t_n$, then these two flight time distributions will have the same standard deviation because adding a constant to a distribution doesn't change standard deviation. The condition $\Delta t_1 = \Delta t_2 = ... = \Delta t_n$ will be achieved if the electric field around the MOT is perfectly uniform. In a uniform electric field, all ions with a given initial $p_{\|}$ take the same time to reverse their velocities, at which time they will have the same characteristics as the initially MCP-directed set of ions. Fig. 3.5a illustrates the invisibly small chromatic aberration for a uniform electric field at the MOT approximating the HUNTER case.

For a nonuniform extraction field, which will result from including a lens for transverse focusing, Fig. 3.5b shows the situation. The two sets of ions each exhibit time focusing, but at different axial positions. This is unsatisfactory since the MCP cannot be placed so as to satisfy the time focusing condition for both sets of ions simultaneously.

Therefore the requirement that the electric field in the vicinity of the MOT be uniform is crucial for achieving the uniform time-focusing condition.

3.4.2 Extraction Field Strength and Longitudinal Momentum Resolution

The inverse relationship between TOF calibration constant and accelerating field strength was introduced in Section. 3.1 above. The momentum resolution $\delta p_{\|}$ can be calculated from the achievable TOF standard deviation σ (a characteristic of the x-ray detectors which give the TOF start signal) using

$$\delta p_{\|} = \frac{\sigma}{\left(\frac{\partial t}{\partial p}\right)} \tag{3.6}$$

here σ is the standard deviation of the ion flight time measurement. The denominator $\partial t/\partial p$ is the magnitude of the slope of TOF vs. $p_{\|}$.

In the HUNTER experiment, the flight time standard deviation is determined by three factors:

1. The flight time resolution of the TOF START signal derived from the x-ray detector, which is expected to be 0.8 ns based on the photoelectron timing of the x-ray scintillators.
2. The flight time resolution of the ion MCP detector itself, which is expected to be 0.3 ns
3. The flight time spreading produced by the spectrometer field configuration and the MOT size. The target value for this factor is 0.1 ns chosen to be smaller than the other two factors. This determines the initial value of the extraction field. After optimization this term turns out to be about 0.5 ns on average.

Note that in the case of HUNTER, the TOF standard deviation is actually dominated by the flight time standard deviation of the x-ray detector, rather than the flight time standard deviation of the ion MCP or the spectrometer characteristics.

Combining these standard deviations in quadrature, the overall standard deviation of flight time in the real experiment should be around 0.9 ns. Since the overall ion momentum resolution required for HUNTER to achieve a neutrino mass square of 200 $(\mathrm{keV}/c^2)^2$ is about 0.31 keV$/c$ (Section. 3.4 above), and assuming for purposes of estimation that the $p_{\|}$ and $p_{\perp}$ are the same, so the $\delta p_{\|}$ should be $0.31/\sqrt{2} = 0.22$ keV$/c$. Inserting these values into Eq. 3.6 gives

$$\left(\frac{\partial t}{\partial p}\right) = 4.1\frac{\mathrm{ns}}{\mathrm{keV}/c} \tag{3.7}$$

Therefore this is the TOF - momentum calibration constant required in order to achieve the desired momentum resolution with the stated flight time standard deviation. This slope dictates the extraction field strength, as shown below.

If the TOF of an ion starting from the center of the MOT is defined as the average TOF, and the TOF of an ion with velocity v flying forward is t, the TOF of ion with velocity v flying backward is $t + \Delta t$. Because the electric field around the MOT is nearly uniform,

$$\Delta t = \frac{2v}{a} = \frac{2v}{\frac{qE}{m}} = \frac{\Delta p}{qE} \tag{3.8}$$

where a is the acceleration, q is the ion charge, E is the extraction field and m is the ion mass. Evidently,

$$\left(\frac{\partial t}{\partial p}\right) = \frac{1}{qE} \tag{3.9}$$

where, for the doubly-charged ions expected to dominate in HUNTER, $q = 2e = 2 \times 1.6 \times 10^{-19}$ C. Therefore, the extraction field must be no greater than E = 0.41 V/mm for achieving desired momentum resolution, given the expected TOF standard deviation dominated by the x-ray START signal.

The extraction field at the MOT is the superposition of the fringing field of the electrostatic lens and the field generated by the electrodes around the MOT. In order to achieve the desired momentum resolution, the extraction field cannot be larger than 0.41 V/mm, and it was initially manually adjusted to 0.41 V/mm in the optimization process described below.

3.5 Optimization Scheme

Starting from the basic analytical considerations given above, a systematic framework has been developed to optimize the voltages and electrode geometry to achieve the best possible overall performance, using the SIMION [80] commercial software package. SIMION both evaluates the potential distributions produced by given electrode geometry and voltages, and accurately tracks ions through these potential distributions.

The SIMION package provides a set of fully worked examples with code and detailed explanations. Several of the examples therein were particularly important in developing the codes for the optimization procedures. The example "tune.iob" shows how to iteratively run SIMION to simulate a group of trajectories, and tune the electrode potentials based on the resulting trajectories. In addition, "einzel.iob" shows how to set up arbitrarily located test-planes on which trajectory intersections can be logged and used for optimization of electrode potentials.

Finally, “random.iob” shows how to adjust the characteristics of ions to be tracked, store them in a “FLY2” file, and reload the file from a SIMION workbench user program. This facilitates switching the trajectory groups as required for different optimization steps.

The optimization procedure consists of two steps: a preliminary manual optimization, followed by an automated brute-force optimization. In the preliminary optimization, the potentials of electrodes in the extraction and lens regions are manually varied to find values which approximate the double focusing condition at the MCP, consistent with considerations of the preceding section.

The population of ions traced to carry out the two optimization steps includes three different sets:

Set **A** Ions are chosen with initial positions on a grid of 10 points uniformly distributed over the surface of a spherical source (the MOT) with a radius of 1 mm. From each of these positions, ions with a total momentum of 330 keV/c, corresponding to the ^{131}Cs decay from the initial ^{131}Xe with a K-shell vacancy, are flown each with ten initial polar angles varied by 22 degrees from 0 to 88 degrees and from 92 degrees to 180 degrees, giving 10 values of $p_{||}$ and $p_{\perp}$ for each starting position.

Set **B** Ions all originate at the center of the MOT. There are 4 groups of ions in the set, each group contains 4 ions. Each group of 4 ions has a fixed $p_{||}$, increasing from 0 to 330 keV/c in successive groups. The $p_{\perp}$ within each group starts with a value giving a total momentum of 330 keV/c and successively decreases by factors of 2 from the largest value.

Set **C** Ions all originate at the center of the MOT. The momenta are chosen in a manner conjugate to that of Set B, again with 4 groups of 4 ions. The $p_{\perp}$ of ions in each group is fixed, with values increasing uniformly from 0 to 330 keV/c in successive groups. The $p_{||}$ varies by successive factors of 2 within each group, with the total momentum corresponding the $p_{\perp}$, and the largest $p_{||}$ being 330 keV/c.

In total, 132 ions were repeatedly flown to optimize the potentials in SIMION.

3.5.1 Preliminary Optimization Procedure

First a preliminary optimization is performed to arrange for an initial configuration with several characteristics:

- a uniform field in the vicinity of the MOT.

	MOT Radius (mm) (r = 0 at MOT center)	Initial $p_{\parallel}$ (keV/c)	Initial $p_{\perp}$ (keV/c)
Set **A**	r = 1	$p_{\parallel} = 330\sin(22(n-1))$ n = 1, 2, ... 5	$p_{\perp} = \sqrt{330^2 - p_{\parallel}^2}$
		$p_{\parallel} = 330\sin(180-22(n-1))$ n = 1, 2, ... 5	$p_{\perp} = \sqrt{330^2 - p_{\parallel}^2}$
Set **B**	r = 0	$p_{\parallel} = \frac{330(n-1)}{4}$ n = 1, 2, 3, 4	$p_{\perp} = \frac{\sqrt{330^2 - p_{\parallel}^2}}{2^m}$ m = 1, 2, 3, 4
Set **C**	r = 0	$p_{\parallel} = \frac{\sqrt{330^2 - p_{\perp}^2}}{2^m}$ m = 1, 2, 3, 4	$p_{\perp} = \frac{330(n-1)}{4}$ n = 1, 2, 3, 4

Table 3.1: The table lists the algorithms for generating ion kinematic characteristics for the optimization.

- time- and transverse-displacement focusing.
- a "double focusing" condition in which the above time- and transverse-displacement focusing both occur at a single source-detector distance.

The parameters chosen to be varied in the preliminary optimization are:

- E_R, the electric field between electrodes on the ion side within the common source region, upstream of the electrostatic lens. This is mainly determined by the voltages on E50 to E59.
- ΔV_{lens}, the potential step between the two electrostatic lens electrodes E48 and E49.
- E_D, the decelerating electric field, which is in the opposite sign as E_R, on the downstream side of the lens pair. This has the effect of adjusting both time- and position- focal lengths. This is mainly determined by the voltages on E42 to E45.
- $V58$ and $V59$, the independently-variable potentials of the electrodes E58, E59 shown in Fig. 3.4. These optimize the field in the vicinity of the MOT.

The general idea of the preliminary optimization is to run SIMION simulations with ΔV_{lens} varying on a grid with a 1 or 2 Volts step size. For each value, $V58$ and $V59$ are automatically varied using the negative-gradient method, to minimize the standard deviation of the on-axis electric field away from the expected mean value of 0.41 V/mm at nine adjacent points in the vicinity of the MOT, spanning 8 mm. For the ions in Set **A** described above, the flight time and radial position are computed on a grid of axial positions and the standard deviations of flight time and radial position are plotted vs. flight distance for each set of potential assignments. It turns out that there is a set of optimum values for E_R, ΔV_{lens}, and E_D that fulfills the three conditions given above, i.e. places all the standard deviation minima at the same flight distance, as shown in Fig. 3.6a. This is where the MCP is placed. More details of this procedure are given in the following.

1. Manually choose starting electrode potentials in the source region to initialize E_D, E_R, and ΔV_{lens}: The lens potential step is set on a linear grid. E_D and E_R are approximately set on a grid of values by choosing the voltage difference between successive electrodes on the ion side of the common source region.

2. Field Uniformity Initialization: For each set of E_D, E_R, and ΔV_{lens} values, the uniformity of the on-axis electric field must be optimized, since accurate time focusing requires a uniform electric field that covers the vicinity of MOT. To achieve this, the on-axis electric field is computed with SIMION at nine adjacent points covering this range, spanning 8 mm, and the standard deviation of the difference between these fields and the desired extraction field of 0.41 V/mm is computed. This standard deviation is called ΔE.

3. Field Uniformity Gradients Initialization: The partial derivatives $\partial(\Delta E)/\partial V_i$ are computed numerically with respect to the voltages on the central region electrodes E58, E59. The values are stored in a vector $\mathbf{n}$.

4. Gradient-Method Field Uniformity Optimization Start: $V58$ and $V59$ are incremented according to $V_{i;new} = V_{i;old} + 2 \times n_i$, where n_i is the i-nth element of the derivative calculated in the preceding step and 2 is the initial step size.

5. Field Uniformity Optimization Step: Re-calculate ΔE with $V_{i;new}$. If the new ΔE is smaller than the previous one, the uniform step size is increased by a factor of 1.2. Otherwise, the uniform step size is decreased by a factor of 1.4. The step sizes for E58 and E59 are always all the same.

6. Gradient-Method Optimization completion: Repeat steps 2 - 5 until the change of ΔE is less than 1×10^{-6} V/mm, or for 50 iterations.

7. 200 SIMION trajectory sampling test planes are placed equally spaced along the symmetry axis. This allows the flight time and radial position data to be recorded when ions pass through each test plane. Ten groups of ions described in Set **A** are flown, and the TOF and IR standard deviation of each group is computed at each test plane. The slope of $\partial(TOF)/\partial p_{||}$ is evaluated using the average TOF of the third group of ions flying toward and away from MCP in Set **A**. Plots of the standard deviations as a function of axial position are shown in Fig 3.6a. If a minimum of the standard deviations occur at a

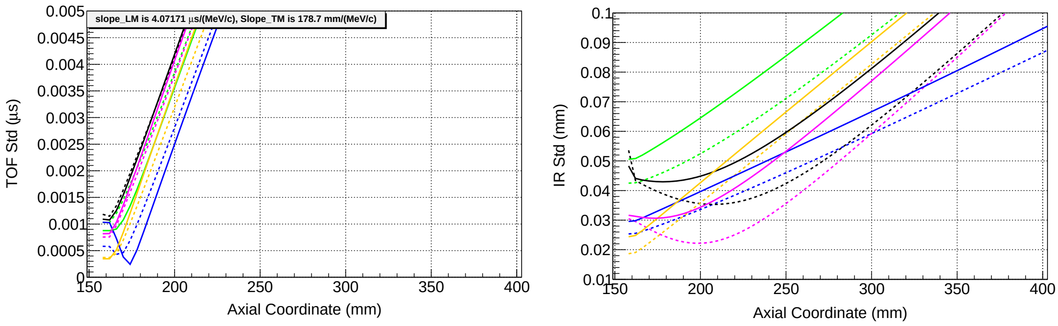

(a) (b)

Figure 3.6: This figure shows the success of the final brute-force optimization at achieving double focusing for the source size used in HUNTER. Plotted are the standard deviations of TOF in (a) and IR in (b), as a function of the axial coordinate. The MOT center is located at an axial coordinate of 1090 mm. The MCP would be placed at an axial coordinate of 158 mm. All ions have the same total momentum (330 keV/c) but different emission angles as indicated by the different colors. Dashed lines show results after the preliminary optimization but before the final optimization. Solid lines show results after the final optimization. Only 5 different emission angles are shown for clarity and the emission angles are: 0, 44, 88, 114, 158 degrees. The standard deviation minima (time focus positions) are seen to be located close to the MCP position. The minimum values are all nearly the same depending on the performance of the preliminary optimization. (Points beyond the MCP cannot be plotted for technical reasons - the field beyond the MCP corresponds to the internal MCP amplification field, and cannot be changed without subtly affecting the focusing results.)

reasonable ion MCP position, and the slope comes out close to the value derived in Section 3.4, then the preliminary optimization has converged. Otherwise, go to the next step.

8. Repeat the above procedure, stepping the lens strength ΔV_{lens} over a range of values separated by 1 or 2 Volts. For each lens strength, change the values of E_D and E_R manually to adjust the time- and position- focal lengths. Repeat the whole process again until the convergence criterion of step. 7 is fulfilled.

For the HUNTER ion spectrometer, suitable values after manual adjustment are: $E_R =$ 0.6 V/mm, $\Delta V_{lens} = 38.7\ V$, and $E_D = -0.52$ V/mm. Fig 3.6a and Fig 3.6b show that the minima of the flight time and radial position standard deviations occur close to $x = 158$ mm, which is a suitable MCP position.

Note that $E_R = 0.6$ V/mm is larger than the evaluated 0.41 V/mm at the MOT because of a decelerating field, which has opposite sign as E_R, between the first electrode facing the MOT and the coil holder next to it. The field strength at the MOT is the superposition of E_R and the decelerating field.

The preliminary optimization provides initial electrode potentials for start of the brute-force optimization, which further optimizes the double focusing and the ion momentum resolution. One of the key issues in the brute-force optimization is to understand the quantities that should be minimized. These quantities comprise the objective function.

3.5.2 Description of Objective Function

The preliminary optimization described above is followed by a brute-force optimization, which consists of minimizing a multivariable objective function expressing all the desired outcomes. The additive terms in the objective function are constructed to all have dimensions of momentum. The objective function consists of three parts:

1. The double focusing condition is imposed using ion Set **A**, all with the same total momentum corresponding to the recoil of ions expected in HUNTER. Each group contains 10 ions originating from different positions within the assumed spherical MOT of radius 1 mm, and each group has a different emission angle and hence different $p_\perp$. The standard deviations of IR and TOF at the MCP have to be minimized for each group. If this minimization were perfect (i.e. converged to give a delta function of TOF for each $p_\parallel$ and a delta function of IR for each $p_\perp$), the system would be perfectly double focusing. The initial $p_\parallel$ could be determined exactly from only the TOF, and $p_\perp$ could be determined exactly from only the IR.

   For computational reasons, each term in the objective function is to be expressed with dimension of momentum. To express conditions on the TOF and IR in this way, the approximated linear relations between the initial $p_\parallel$ ($p_\perp$) and measured TOF (IR) are used. This is derived, for example, in Ref. [70] for a simplified field geometry, and keeping only the lowest order terms of the kinematics formulas for TOF (IR) vs. $p_\parallel$ ($p_\perp$) derived. These linear relations can be written as

$$t = s_l \times p_\parallel + a \tag{3.10a}$$

$$i_r = s_t \times p_\perp + b \tag{3.10b}$$

   where t and i_r represent TOF and IR, respectively. s_l and s_t are the slopes, and a and b are the intercepts. The corresponding momentum resolutions can be expressed as in Eq. 3.11 by applying a variational method

$$\delta p_{\parallel,A} = \frac{\delta t}{s_l} \tag{3.11a}$$

$$\delta p_{\perp,A} = \frac{\delta i_r}{s_t} \tag{3.11b}$$

where $\delta p_{\|,A}$ and $\delta p_{\perp,A}$ express the momentum resolutions associated with the finite TOF and IR standard deviations due to the MOT size and spectrometer characteristics. The slopes are evaluated at each iteration using the ion groups in Set **A** all together. The sum of $\delta p_{\|,A}$ and $\delta p_{\perp,A}$ is then added to the objective function to be minimized.

2. One wishes to be able to determine $p_{\|}$ from the TOF alone, and $p_{\perp}$ from the IR alone. However, the TOF focusing and IR focusing are achieved by non-uniform electric fields. These produce axial and radial accelerations which are not constants, leading to correlations between $p_{\perp}$ and TOF, or $p_{\|}$ and IR. Effects of this type have also been considered in Ref.[81]. Fortunately, these effects can be effectively suppressed by the optimization.

   To suppress the undesired correlations, additional terms are introduced into the objective function. These depend on the standard deviation of the TOF (IR) for ions with a given $p_{\|}$ ($p_{\perp}$) and different $p_{\perp}$ ($p_{\|}$). For these terms, ion Set **B** (Set **C**) were simulated. Each group contains ions with a fixed $p_{\|}$ ($p_{\perp}$), varying $p_{\perp}$ ($p_{\|}$), and origin at the center of the MOT.

   To express these terms with units of momentum, the slopes s_l (s_t) in Eq. 3.10 are again used.

$$\delta p_{\|,B} = \frac{\delta t'}{s_l} \tag{3.12a}$$

$$\delta p_{\perp,C} = \frac{\delta i'_r}{s_t} \tag{3.12b}$$

   where $\delta t'$ ($\delta i'_r$) represents the standard deviation of flight time (IR) of ions with a given $p_{\|}$ ($p_{\perp}$) but varying $p_{\perp}$ ($p_{\|}$). The sum of $\delta p_{\|,B}$ and $\delta p_{\perp,C}$ must be of the order 1×10^{-2} keV$/c$ to achieve the neutrino mass reconstruction resolution desired for HUNTER.

3. The standard deviations of $p_{\|}$ ($p_{\perp}$) in Eq. 3.11 have different values. It would be preferable to have the same reconstructed $\delta p_{\|}$ ($\delta p_{\perp}$) for ions emitted in 4π angle. Therefore other terms for minimizing the difference between the standard deviations are introduced into

the objective function.

$$\sigma_{\delta p_{\parallel,A}} = \sqrt{\frac{1}{10}\sum_{i=1}^{10}(\delta p_{\parallel,A,i} - \overline{\delta p_{\parallel,A}})^2} \tag{3.13a}$$

$$\sigma_{\delta p_{\perp,A}} = \sqrt{\frac{1}{10}\sum_{i=1}^{10}(\delta p_{\perp,A,i} - \overline{\delta p_{\perp,A}})^2} \tag{3.13b}$$

where $\sigma_{\delta p_{\parallel,A}}$ ($\sigma_{\delta p_{\perp,A}}$) and $\overline{\delta p_{\parallel,A}}$ ($\overline{\delta p_{\perp,A}}$) represent the standard deviation and the mean value of the reconstructed $\delta p_{\parallel}$ ($\delta p_{\perp}$) of 10 groups of ions, respectively.

The final expression for the objective function is

$$\begin{aligned} f &= \delta p_{\parallel,A} + \delta p_{\perp,A} + \delta p_{\parallel,B} + \delta p_{\perp,C} + \sigma_{\delta p_{\parallel,A}} + \sigma_{\delta p_{\perp,A}} \\ &= \sum_{i=1}^{10}(\frac{\delta t_i}{s_l} + \frac{\delta i_{r,i}}{s_t}) + c\sum_{j=1}^{4}(\frac{\delta t_j^{'}}{s_l} + \frac{\delta i_{r,j}^{'}}{s_t}) + \sqrt{\frac{1}{10}\sum_{i=1}^{10}(\frac{\delta t_i}{s_l} - \overline{\frac{\delta t}{s_l}})^2} + \sqrt{\frac{1}{10}\sum_{i=1}^{10}(\frac{\delta i_{r,i}}{s_t} - \overline{\frac{\delta i_r}{s_t}})^2} \end{aligned}$$

here δt_i is computed by combining the standard deviation of the TOF of the i-th group ions in Set **A**, the MCP flight time standard deviation, and the x-ray detector flight time standard deviation. The term $\delta i_{r,i}$ is computed by combining the IR standard deviation of the i-th ion group in Set **A**, the MCP spatial resolution, and the x-ray detector spatial resolution. The slope s_l (s_t) is the slope of $p_{\parallel}$ ($p_{\perp}$) vs. TOF (IR). $\delta t_j^{'}$ and $\delta i_{r,j}^{'}$ are the standard deviation of flight time and the standard deviations of IR, respectively. Finally, $\overline{\frac{\delta t}{s_l}}$ ($\overline{\frac{\delta i_r}{s_t}}$) is the mean value of the reconstruction resolutions of $p_{\parallel}$ ($p_{\perp}$) of 10 groups. The constant c is a weight factor adjusting the weight of the second term, with an empirical value around 10. This value was obtained from the optimization of the ion momentum resolution.

3.6 Brute-force Optimization

The brute-force optimization fine-tunes the spectrometer by adjusting all of the electrode voltages independently in a negative-gradient scheme. The procedure is based on tracking the ions depicted in Table. 3.1. The resulting TOF and IR on the MCP are recorded event-by-event for each set of electrode voltages. These TOF and IR are then used to compute the "objective function", which encodes the desired spectrometer characteristics (double focusing, high resolution, etc.). The objective function is then minimized by iteratively changing some or all of the electrode voltages, re-tracing the population of ions, and re-calculating the objective function value.

Based on the magnitude and the sign of the objective function change, the electrode voltages are again adjusted, and the procedure is repeated until a convergence criterion is satisfied.

The procedure is as follows:

1. Simulate ion sets **A - C** with SIMION and acquire TOF and IR data on the detector plate. Compute the objective function f as described in section 3.5.2.
2. Compute the initial gradients of f with respect to all 59 electrode voltages in the spectrometer. The resulting algebraic signs and values are stored in a vector $\mathbf{n}$ of dimension 59.
3. Each electrode voltage is now incremented according to $V_{i,new} = V_{i,old} + 5 \text{ Volts} \times n_i$, in which n_i is the element of the vector calculated in the preceding step and 5 Volts is the initial step length.
4. Ion groups **A-C** are simulated again with the incremented voltages, and f is evaluated again.
5. If the new f is smaller than the previous one, the step length is increased by a factor of 1.2.
6. If the new f is larger than the previous one, the step length is reduced by a factor of 1.4.
7. Repeat steps 2 - 6 until the change in f is less than 1×10^{-7}. At this point, the search is considered to have converged and the optimization process ends.

Comment: Source Set **B** and **C** only include ions initially traveling toward the ion MCP, not those emitted in the opposite hemisphere. This is because empirically, better resolution results were obtained by optimizing only ions in the one hemisphere.

3.7 Resolution and Reconstruction

$\delta p_{\parallel}$ and $\delta p_{\perp}$ are calculated using Eq. 3.11 after the brute-force optimization. A set of ions similar to Set **A** is used in evaluating the resolution but the number of random initial positions is changed to 1000. The computed $\delta p_{\parallel}$ and $\delta p_{\perp}$ for ions with charge 2e and 1e emitted in different angles are listed in Table. 3.2. [1] Because the TOF standard deviation is dominated by the x-ray detectors' flight time standard deviation, $\delta p_{\parallel}$ would be significantly improved if the x-ray detector with higher time resolution were available. Efforts are underway to achieve this

---

[1] The potentials and the detailed resolutions are presented in Appendix B

q=2e					
Angle(degree)	0.0	22.0	44.0	66.0	88.0
$\delta p_{\parallel}$ (keV/c)	0.306	0.330	0.372	0.386	0.369
$\delta p_{\perp}$ (keV/c)	0.314	0.371	0.390	0.455	0.503
Angle(degree)	92.0	114.0	136.0	158.0	180.0
$\delta p_{\parallel}$ (keV/c)	0.360	0.293	0.248	0.226	0.216
$\delta p_{\perp}$ (keV/c)	0.496	0.397	0.319	0.312	0.305
q=1e					
Angle(degree)	0.0	11.0	22.0	33.0	44.0
$\delta p_{\parallel}$ (keV/c)	0.241	0.253	0.279	0.314	0.350
$\delta p_{\perp}$ (keV/c)	0.229	0.303	0.295	0.310	0.380
Angle(degree)	136.0	147.0	158.0	169.0	180.0
$\delta p_{\parallel}$ (keV/c)	0.147	0.126	0.118	0.113	0.111
$\delta p_{\perp}$ (keV/c)	0.259	0.216	0.219	0.237	0.217

Table 3.2: The momentum resolution of ions achieved by the optimization, for each emission angle without presence of the ~8 G uniform magnetic field produced by the outside solenoids. The standard deviations of TOF (IR) of MCP and x-ray are included in calculating $\delta p_{\parallel}$ ($\delta p_{\perp}$).

q=2e					
Angle(degree)	0.0	22.0	44.0	66.0	88.0
$\delta p_{\parallel}$ (keV/c)	0.306	0.330	0.373	0.386	0.369
$\delta p_{\perp}$ (keV/c)	0.315	0.395	0.415	0.478	0.530
Angle(degree)	92.0	114.0	136.0	158.0	180.0
$\delta p_{\parallel}$ (keV/c)	0.360	0.293	0.248	0.225	0.216
$\delta p_{\perp}$ (keV/c)	0.523	0.424	0.350	0.340	0.303
q=1e					
Angle(degree)	0.0	11.0	22.0	33.0	44.0
$\delta p_{\parallel}$ (keV/c)	0.241	0.252	0.279	0.314	0.350
$\delta p_{\perp}$ (keV/c)	0.230	0.310	0.302	0.318	0.389
Angle(degree)	136.0	147.0	158.0	169.0	180.0
$\delta p_{\parallel}$ (keV/c)	0.147	0.126	0.117	0.113	0.111
$\delta p_{\perp}$ (keV/c)	0.271	0.227	0.229	0.245	0.217

Table 3.3: The momentum resolution of ions achieved by the optimization, for each emission angle with presence of the ~8 G uniform magnetic field. The standard deviations of TOF (IR) of MCP and x-ray are included in calculating $\delta p_{\parallel}$ ($\delta p_{\perp}$).

but these are beyond the scope of the present work. However, the impact on the neutrino mass resolution would be small. The trendline of TOF (IR) vs. $p_{\parallel}$ ($p_{\perp}$) for momentum reconstruction is shown in Fig. 3.7 (Fig. 3.8).

For the simulation with the 8 G magnetic field for confining the electron trajectories, $\delta p_{\parallel}$ is unchanged because the magnetic field has no effect on the TOF, but $\delta p_{\perp}$ is degraded by ~6%, as shown in Table. 3.3

To simulate the neutrino mass-squared resolution, a C++ program was written to generate sets of particles (ion, x-ray, Auger electron(s)) satisfying the kinematics of the ^{131}Cs decay, from a MOT with a full width at a half maximum of 1 mm. The initial momenta of ions, Auger electrons, and x-rays generated by the program were exported to SIMION and the trajectories in the electric field and a uniform 8 G magnetic field were simulated, recording the TOF and IR of ions arriving at the MCP.

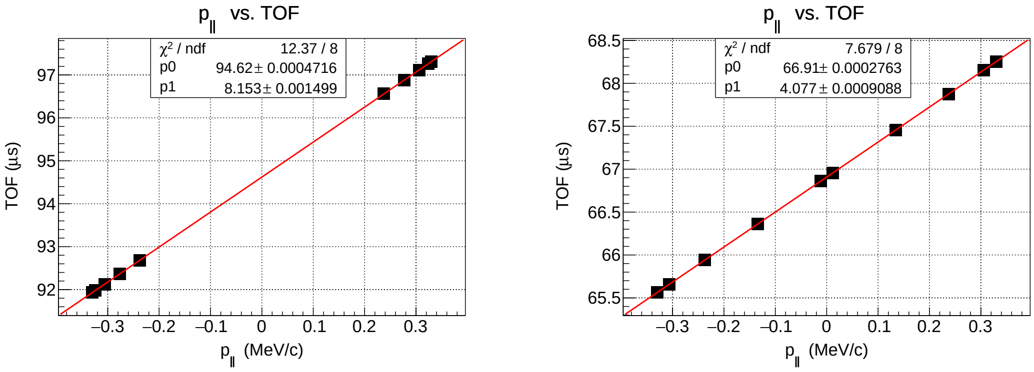

(a) TOF vs. $p_{||}$ for ions of charge 1e. (b) TOF vs. $p_{||}$ for ions of charge 2e.

Figure 3.7: The trendlines of TOF vs. $p_{||}$. A linear trendline $y = p0 + p1 \cdot x$ was used to fit the data. The parameters $p0$ and $p1$ are shown in the legends in figure (a) and (b). In (a), there is no data for ions with $p_{||}$ between -0.24 MeV/c to 0.24 MeV/c because in the present configuration, ions of charge 1e emitted in the corresponding angle range arrive at the MCP axial position with a transverse coordinate larger than the MCP radius. This could be remedied by using larger MCPs when they become available. However, the charge 1e ions are at most 40% of the ions produced in HUNTER, and still 50% of these ions are collected.

$p_{||}$ and $p_{\perp}$ were then reconstructed from the simulated TOF and IR, using the trendline functions shown in Fig. 3.7 and Fig. 3.8. The two orthogonal components of $p_{\perp}$ were reconstructed from the corrected azimuthal angle considering a constant azimuthal angular deflection of ion trajectories in the uniform magnetic field. The neutrino mass then was computed using the reconstructed values, without including the momentum resolutions of the Auger electrons and the x-ray. The resulting reconstructed mass-squared spectrum of the neutrinos is shown in Fig. 3.9.

In Section. 3.4 above, the required extraction field was estimated using a desired neutrino mass-squared resolution of 200 keV/c^2. The reconstructed mass-squared distribution has a resolution of $\sim$300 keV/c^2. There are two main reasons for this difference:

1. Eq. 3.5 used to estimate the field strength assumed average values of $\cos^2\theta_1$ and $\cos^2\theta_2$, which do not precisely reflect the angular relation between $\delta\mathbf{P}_e$ and $\mathbf{P}_\nu$, $\delta\mathbf{P}_{Xe^+}$ and $\mathbf{P}_\nu$, largely because of the small angular coverage for x-rays in HUNTER, as reflected in the ^{131}Cs decay simulation.

2. Ions emitted at large angles to the symmetry axis have trajectories which are not paraxial. This inescapably results in a worse momentum resolution than for ions emitted at small angles, as shown in Table. 3.2. A substantial number of ions have large emission angles as shown in Fig 3.10.

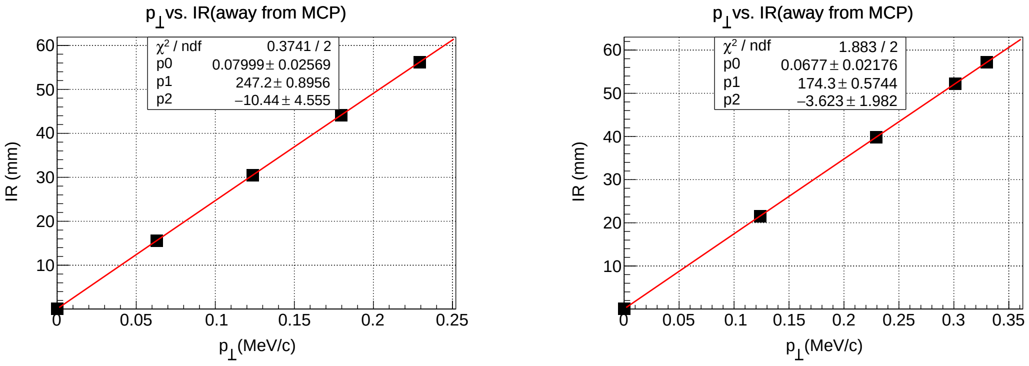

(a) IR vs. $p_\perp$ for ions of charge 1e flying away from MCP.

(b) IR vs. $p_\perp$ for ions of charge 2e flying away from MCP.

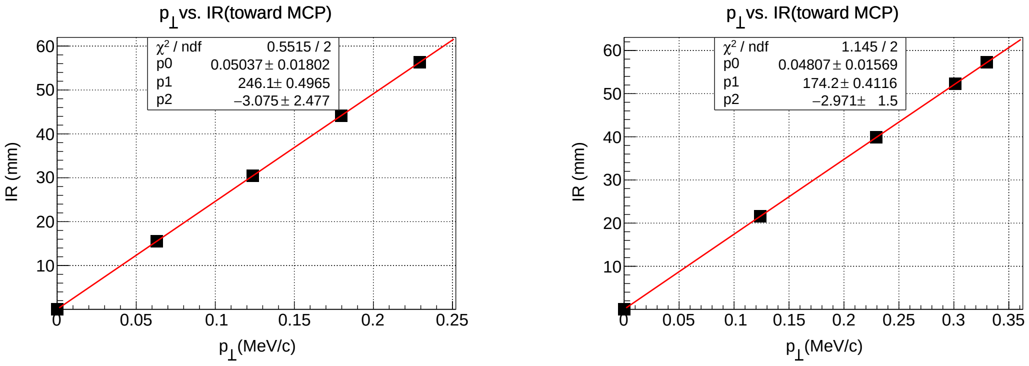

(c) IR vs. $p_\perp$ for ions of charge 1e flying toward MCP.

(d) IR vs. $p_\perp$ for ions of charge 2e flying toward MCP.

Figure 3.8: The trendlines of IR vs. $p_\perp$. A second-order polynomial trendline $y = p0 + p1 \cdot x + p2 \cdot x^2$ had to be used to give a satisfactory fit, in contrast to the first-order trends used for the $p_{||}$ cases.

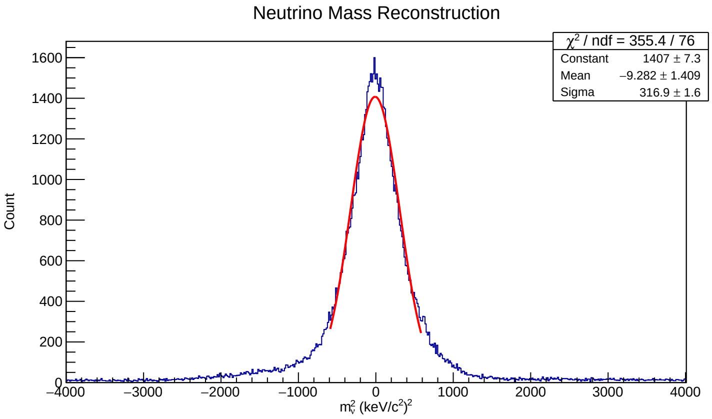

Figure 3.9: Simulation of reconstructed neutrino mass spectrum for the "high acceptance" spectrometer tune.

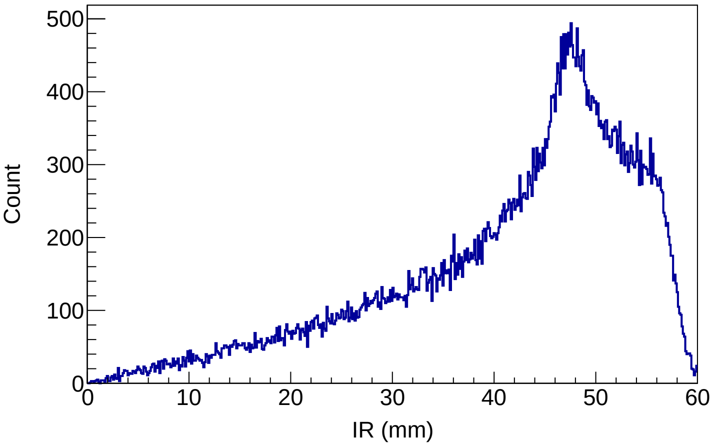

Figure 3.10: The distribution of the IR for ions with charge 2e in the high acceptance tune.

3.8 High Resolution Tune

In the optimization described above, ions are collected onto an assumed 60 mm radius MCP with 4π solid angle efficiency. This requires an extraction field set to 0.41 V/mm, which still gives a momentum resolution adequate for the first phase HUNTER experiment. Much better momentum resolution (and consequent sensitivity to lower neutrino masses) can be achieved, but to do so the ions must be spread over a larger area at the MCP position. This can easily be seen by noting that the $\delta p_\perp$ is at best given by the number of resolution bins within the MCP radius. For a radius of 60 mm and spatial resolution of 50 μm, there are ~1000 resolution bins, which corresponds closely to the resolution achieved here. At the time of writing, larger MCPs with position-sensitive readout are not available for HUNTER.

Anticipating future developments of MCP technology [82], a high resolution tune has also been obtained by the method outlined here, which would only collect ∼12% of the ions onto the largest presently-available MCP (60 mm radius). The neutrino mass goal for the high resolution tune is $\sim 50(\mathrm{keV}/c^2)^2$, set by the controversial 3.5 keV astrophysical x-ray line [83, 50] which has been attributed to dark matter sterile neutrino decay. Such a tune requires an extraction field of about 0.11 V/mm, according to Section. 3.4. A separate full optimization was carried out for this extraction field, called the "high resolution tune". The actually achieved ion momentum resolution in the simulation is ∼0.1 keV and the reconstructed neutrino mass-squared is $\sim 100\ (\mathrm{keV}/c^2)^2$, including the errors coming from ion momentum reconstruction and x-ray detector time resolution.

The ion acceptance in the high resolution tune is limited by the MCP size, which could be remedied in the future if larger MCPs become available. Eq. 3.6 shows that $\delta p_{\|}$ is determined by the TOF standard deviation and the slope of TOF vs. $p_{\|}$. In HUNTER, the TOF standard deviation is dominated by the TOF standard deviation of the x-ray detector, independent of spectrometer characteristics, and cannot be optimized. The only way to achieve higher $\delta p_{\|}$ is to increase the slope, since $\delta p_{\|}$ is inversely proportional to the slope. Following the derivation of the extraction field in Section. 3.4, it is easy to conclude that the extraction should be weaker to achieve a higher $\delta p_{\|}$. Meanwhile, the weaker extraction field means longer TOF of ions in the extraction field region and lower longitudinal velocity when they depart the extraction field region. This results in a larger transverse displacement since the transverse displacement is the product of the $p_{\perp}$ and TOF, and that is why the collection efficiency of ions is much smaller.

CHAPTER 4

SYSTEMATIC ERRORS OF THE ION SPECTROMETER

The ion momentum resolution optimization described in the preceding chapter is based on a 2-D model of the HUNTER spectrometer, in which the axial symmetry is imposed when constructing the model in SIMION to reduce the required RAM and to keep the computation time needed to simulate the hundreds of thousands of ion paths manageable for the optimization. Many asymmetric structures of the spectrometer are ignored in the 2-D model, like the ports on the central chamber for different functions, the supporting structures of the spectrometer, the possible accumulation of charges on the inner wall of the chamber, etc. Meanwhile, the parameters of the spectrometer are ideal and do not consider the systematic errors of the experiment. To evaluate the deviation of the resolution away from the 2-D optimization results, a series of 3-D simulations, including asymmetric components of the spectrometer design, were performed.

4.1 Potentials and Positions of Electrodes

The potentials of electrodes achieved from optimization have an unattainably high precision compared to the precision of the power supplies of HUNTER. In the HUNTER experiment, the potential of each electrode will be provided by an individual home-made 16-bit power supply with a unipolar output, covering potentials from 0 to ±400 V, with a precision around $400/2^{16}$ V $\approx$ 6 mV. To study the deviation of momentum resolution due to the potential precision, 2-D simulations are adequate but the optimized potentials should be rounded off to multiples of 6 mV.

Another source of the deviation of the momentum resolution is attributed to the precision of the electrodes' position, which is determined by the precision of the ceramic spacers placed between electrodes. However, to study the deviation of the momentum resolution caused by the offset of electrodes requires an unreasonable amount of computer memory and time, because the ratio of the spectrometer size and the "Potential Array" grid size of SIMION, matching the precision of the spacer dimension, is huge.

Given that the offsets of electrodes causes changes of the electric field, the effect of the offsets of electrodes can be studied indirectly by simulating the variation of the momentum resolution due to the variation of the potentials.

To evaluate the overall effect of potentials' precisions and the offsets of electrodes, all of the electrode potentials were varied by a random number in the range [-6, 6] mV. Every time the potentials were adjusted, ions of Set **A** introduced in Section. 3.5 with 1000 random initial positions were flown. The TOF and IR of each ion were recorded and the initial $p_{||}$ and $p_{\perp}$ were reconstructed by using the linear trendline functions calculated from linear regression for this set of potentials. The average TOF (μ_{TOF}) (average IR (μ_{IR})) and $\delta p_{||}$ ($\delta p_{\perp}$) for 1000 ions in each group were then calculated. Statistically meaningful results were achieved by repeating this randomly-varying potential process 5000 times. The distributions of μ_{TOF} and $\delta p_{||}$ for 10 groups of ions described in Set **A** are shown in Fig. 4.1. This study was done for doubly-charged ions.

The distributions of μ_{TOF} and $\delta p_{||}$ for 5 groups of ions emitted opposite (toward) the ion MCP are shown in Fig. 4.1a (Fig. 4.1b) and Fig. 4.1c (Fig. 4.1d), respectively. The values in the legends of the subfigures in Fig. 4.1 are listed in Table. 4.1. The mean values of μ_{TOF} ($\mu(\mu_{TOF})$) are varied by 1 or 2 ns compared to the optimized μ_{TOF} as shown in Table. A.2, which indicates that potential variation may change the μ_{TOF} by 1 or 2 ns. The standard deviations of $\delta p_{||}$ ($\delta(\delta p_{||})$) are around zero, which indicates that potential variation has limited influence on $\delta p_{||}$ in HUNTER.

Angle(degree)	0.0	22.0	44.0	66.0	88.0
$\mu(\mu_{TOF})$ (µs)	68.250	68.156	67.875	67.458	66.954
$\delta(\mu_{TOF})$ (µs)	0.002	0.001	0.002	0.001	0.001
$\mu(\delta p_{||})$ (keV/c)	0.306	0.330	0.374	0.389	0.373
$\delta(\delta p_{||})$ (keV/c)	0.001	0.001	0.001	0.000	0.000
Angle(degree)	92.0	114.0	136.0	158.0	180.0
μ_{TOF} (µs)	66.859	66.363	65.938	65.658	65.652
$\delta(\mu_{TOF})$ (µs)	0.001	0.002	0.002	0.002	0.001
$\mu(\delta p_{||})$ (keV/c)	0.364	0.295	0.249	0.226	0.215
$\delta(\delta p_{||})$ (keV/c)	0.000	0.000	0.000	0.000	0.000

Table 4.1: The values in the legends in Fig. 4.1 are listed in this table. $\mu(\mu_{TOF})$ and $\delta(\mu_{TOF})$ are the mean value and the standard deviation for the μ_{TOF} distribution, respectively. $\mu(\delta p_{||})$ and $\delta(\delta p_{||})$ are the mean value and the standard deviation for the distribution of reconstructed $\delta p_{||}$, respectively.

The distributions of μ_{IR} and $\delta p_{\perp}$ for 5 groups of ions emitted opposite (toward) the ion MCP are shown in Fig. 4.2a (Fig. 4.2b) and Fig. 4.2c (Fig. 4.2d), respectively. The values in the legends of the subfigures in Fig. 4.2 are listed in Table. 4.2. The mean values of μ_{IR} ($\mu(\mu_{IR})$) are the same as the optimized μ_{IR} as shown in Table. A.2. The standard deviations of $\delta p_{\perp}$ ($\delta(\delta p_{\perp})$)

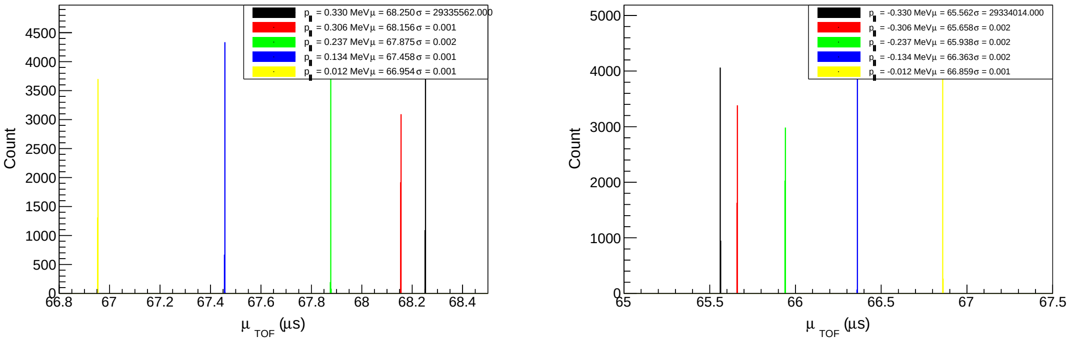

(a) μ_{TOF} distributions for 5 groups of ions emitted opposite the ion MCP.

(b) μ_{TOF} distributions for 5 groups of ions emitted toward the ion MCP.

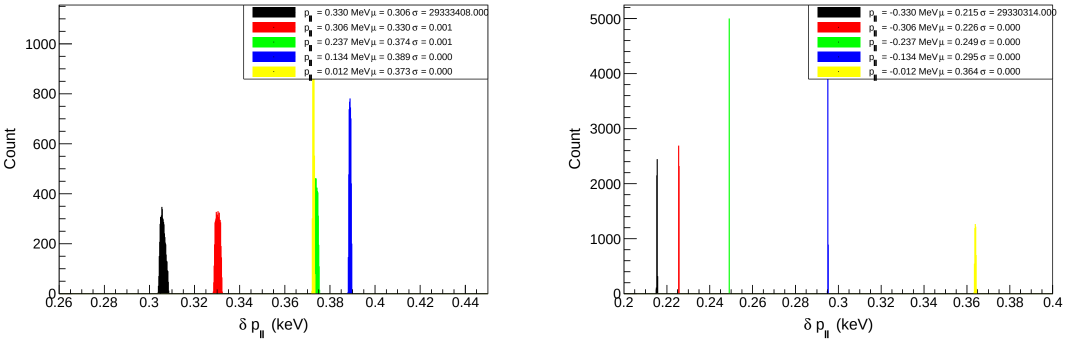

(c) $\delta p_{\|}$ distributions associated with 4.1a.

(d) $\delta p_{\|}$ distributions associated with 4.1b.

Figure 4.1: The μ_{TOF} and the associated $\delta p_{\|}$ distributions of ions emitted in 10 polar angles are shown in separate figures according to their emission directions with respect to the ion MCP. (a) and (c) show the distributions of μ_{TOF} and the calculated $\delta p_{\|}$ for 5 groups of ions emitted opposite the ion MCP direction, respectively. The initial $p_{\|}$, mean values of μ_{TOF}, and the standard deviations of the μ_{TOF} distributions are shown in the legend of (a). The initial $p_{\|}$, mean values of reconstructed $\delta p_{\|}$, and the standard deviations of the $\delta p_{\|}$ are shown in the legend of (c). (b) and (d) are the same as (a) and (c), but for 5 groups of ions emitted toward the ion MCP

are zero. Thus, the $p_\perp$ resolution will not be affected by the potential variation in HUNTER.

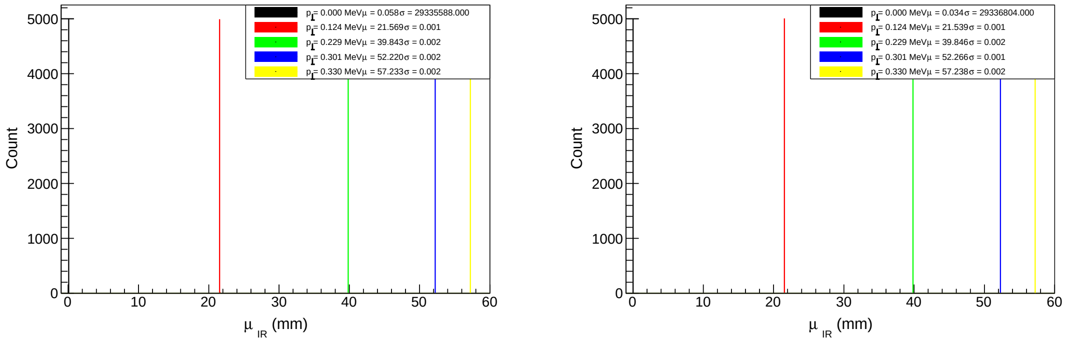

(a) μ_{IR} distributions for 5 groups of ions emitted opposite the ion MCP.

(b) μ_{IR} distributions for 5 groups of ions emitted toward the ion MCP.

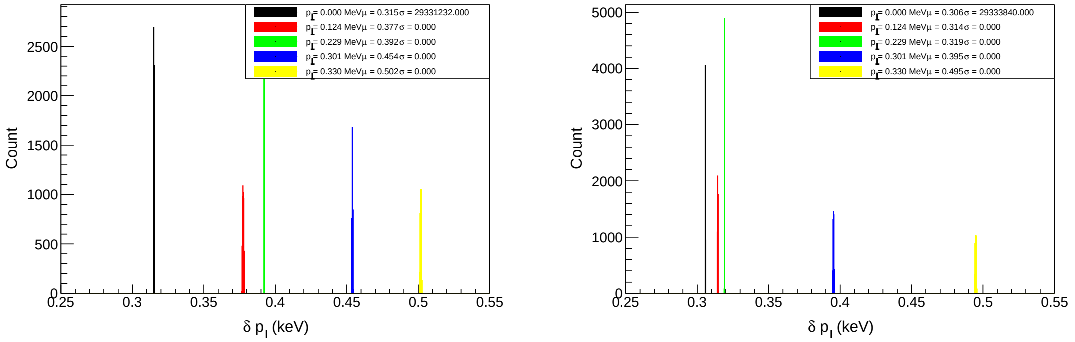

(c) $\delta p_\perp$ distributions associated with 4.2a.

(d) $\delta p_\perp$ distributions associated with 4.2b.

Figure 4.2: The μ_{IR} and $\delta p_\perp$ distributions of ions emitted in 10 polar angles are shown in these figures. (a) and (c) show the μ_{IR} distributions and calculated $\delta p_\perp$ for 5 groups of ions emitted opposite the ion MCP direction, respectively. The initial $p_\perp$, mean values of μ_{IR}, and the standard deviations of the μ_{IR} distributions are shown in the legend of (a). The initial $p_\perp$, mean values of $\delta p_\perp$, and the standard deviation of $\delta p_\perp$ are shown in the legend of (c). (b) and (d) are the same as (a) and (c), but for 5 groups of ions emitted toward the ion MCP.

Angle(degree)	0.0	22.0	44.0	66.0	88.0
$\mu(\mu_{IR})$ (mm)	0.058	21.569	39.843	52.220	57.233
$\delta(\mu_{IR})$ (mm)	0.000	0.001	0.002	0.002	0.002
$\mu(\delta p_\perp)$ (keV/c)	0.315	0.377	0.392	0.454	0.502
$\delta(\delta p_\perp)$ (keV/c)	0.000	0.000	0.000	0.000	0.000
Angle(degree)	92.0	114.0	136.0	158.0	180.0
μ_{IR} (mm)	57.238	52.266	39.846	21.539	0.034
$\delta(\mu_{IR})$ (mm)	0.002	0.001	0.002	0.001	0.000
$\mu(\delta p_\perp)$ (keV/c)	0.495	0.395	0.319	0.314	0.306
$\delta(\delta p_\perp)$ (keV/c)	0.000	0.000	0.000	0.000	0.000

Table 4.2: The values in the legends in Fig. 4.2 are listed in this table. $\mu(\mu_{IR})$ and $\delta(\mu_{IR})$ are the mean value and the standard deviation of the μ_{IR} distribution, respectively. $\mu(\delta p_\perp)$ and $\delta(\delta p_\perp)$ are the mean value and the standard deviation of the distribution of reconstructed $\delta p_\perp$, respectively.

4.2 Effect of Asymmetric Components

Another factor that can't be included in a 2-D simulation is due to asymmetric components. In order to study the deviation of the momentum resolution due to the variation of the electric field caused by different asymmetric components, a 3-D model of the HUNTER spectrometer was constructed in SIMION, including supporting rings, supporting rods traversing the supporting rings, supporting rods traversing the electrodes, brackets holding the small electrodes, etc. The 3-D model of the spectrometer constructed in SOLIDWORKS is shown in Fig. 4.3a. The ion and electron spectrometers are identical except for the mesh in front of the ion MCP. The large and small electrodes are supported by 8 and 4 thin ceramic rods, respectively, with a radius of 4 mm. 4 supporting rings made of stainless steel with a thickness of 10 mm, outer radius of 286.5 mm, and inner radius of 242 mm, traversed by 8 thick ceramic rods with a radius of 10 mm, serve as the main supporting structure. The 8 thin rods of the large electrode also traverse the 4 supporting rings to connect the large electrodes to the supporting rings. The supporting ring at the join between the large and small electrodes consists of two concentric rings connected by fingers in radial directions. The small electrodes are connected to the main supporting structure by four brackets. In order to suppress the eddy current induced in the electrodes, fan sectors are cut out from the coil holders and the electrode is sandwiched between them, as shown in Fig. 3 and Fig. 4 in Appendix A.

The axial symmetry of the electric field generated by the electrodes is broken in the region far away from the center of the MOT. The axial symmetry is preserved in the region with a radius comparable to the inner radius of the small electrodes, as shown in Fig. 4.3b.

The resolutions for the full 3-D structure with the optimized potentials from the 2-D optimization have been obtained by simulating the ions emitted in azimuthal angles -90, 0 and 90 degrees. The resulting values are shown in Table. 4.3:

There is an obvious change of the longitudinal momentum resolution compared to Table. 3.2. Including the asymmetric structures degrades $\delta p_{\parallel}$ ($\delta p_{\perp}$) by $\sim$40% ($\sim$16%). Within the physical and optical constraints of HUNTER, this degradation must be accepted. A future experimental design would concentrate on reducing these effects.

4.3 Systematic Effect of Charge Accumulation

In the HUNTER experiment, escaped ^{131}Cs atoms from the MOT may accumulate on the wall of the spectrometer chamber particularly on non-conducting surfaces like the laser windows.

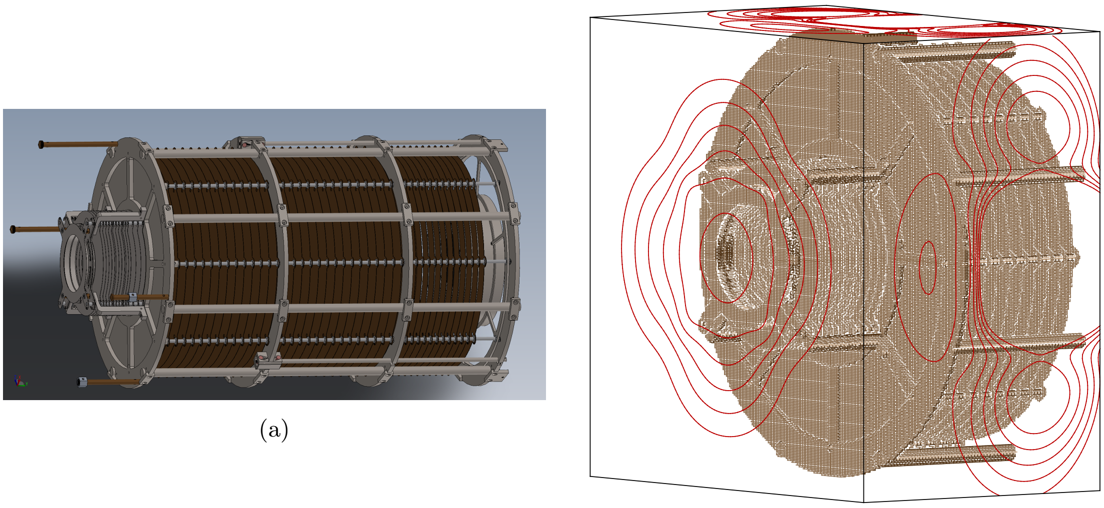

(a)

(b)

Figure 4.3: (a): Solidworks model of the spectrometer, courtesy of the HUNTER collaborators Dr. Schneider and Dr. Lamichhane. The radial distance from the axis of the spectrometer to the outside thick (inside thin) rods traversing the large electrodes is 270 mm (250 mm). The radial distance from the axis to the rods traversing the small electrodes is 126.5 mm. (b): Spectrometer 3-D model in SIMION with contour lines in red. The contour lines represent the the spatial potential distribution produced by the electrodes in those specific planes. The potential of the two innermost contour lines in the front face is -18 V and the potentials of the rest of the contour lines from the inside to outside are -16 V, -14 V, -12 V and -10 V, respectively.

			q=2e		
Angle(degree)	0.0	22.0	44.0	66.0	88.0
$\delta p_{\parallel}$ (keV/c)	0.436	0.458	0.502	0.530	0.525
$\delta p_{\perp}$ (keV/c)	0.290	0.326	0.422	0.526	0.587
Angle(degree)	92.0	114.0	136.0	158.0	180.0
$\delta p_{\parallel}$ (keV/c)	0.523	0.481	0.439	0.408	0.397
$\delta p_{\perp}$ (keV/c)	0.580	0.463	0.353	0.298	0.289
			q=1e		
Angle(degree)	0.0	11.0	22.0	33.0	44.0
$\delta p_{\parallel}$ (keV/c)	0.277	0.290	0.314	0.349	0.383
$\delta p_{\perp}$ (keV/c)	0.206	0.218	0.254	0.321	0.430
Angle(degree)	136.0	147.0	158.0	169.0	180.0
$\delta p_{\parallel}$ (keV/c)	0.285	0.262	0.246	0.236	0.233
$\delta p_{\perp}$ (keV/c)	0.300	0.231	0.208	0.208	0.208

Table 4.3: The momentum resolution of ions for each emission angle. The standard deviations of TOF, impact radius on MCP, and x-ray momentum are included in calculating $\delta p_{\parallel}$ ($\delta p_{\perp}$).

The charged decay products of ^{131}Cs atoms can stick to the wall and form a patch of a certain potential. To evaluate the influence of the charge accumulation, a patch, with a diameter of 100 mm and a potential of 10 V, was constructed in the 3-D model of the spectrometer. The patch was positioned 400 mm away from the MOT in the azimuthal direction. Only one patch was included in case of the cancellation effect of equally spaced patches along the azimuthal direction.

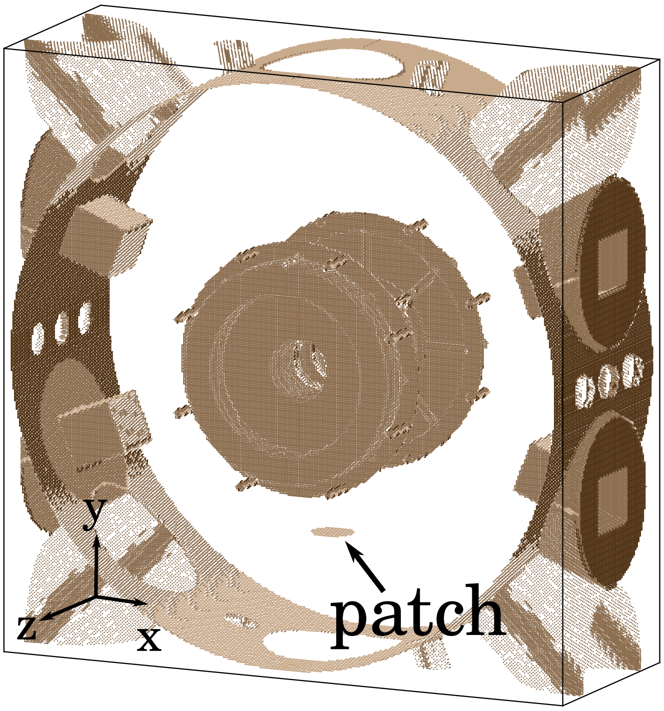

Figure 4.4: The central region of the 3-D model with a patch of 10 V simulating the charge accumulation effect. The coordinate system is shown in the lower lefthand corner.

Ten groups of ions described in Section 3.7 were flown repeatedly with three azimuthal angles of -90, 0 and 90 degrees. For ions flown on the far side of the patch, i.e. on the upper half of YZ plane, the trajectories were not affected by the patch in general. The resolution is degraded by less than 1% compared to the resolutions in Table. 4.3. The momentum resolutions are listed in Table. 4.4

For ions emitted with azimuthal angle of 0 degrees, i.e. on the right half of XZ plane, $\delta p_{\parallel}$ and $\delta p_{\perp}$ were the same as shown in Table. 4.4.

For ions emitted in the lower half of YZ plane, compared to Table. 4.3, the variations of $\delta p_{\parallel}$ and $\delta p_{\perp}$ were less than 1%. The resolutions are shown in Table. 4.5

q=2e					
Angle(degree)	0.0	22.0	44.0	66.0	88.0
$\delta p_{\parallel}$ (keV/c)	0.440	0.462	0.506	0.534	0.529
$\delta p_{\perp}$ (keV/c)	0.294	0.329	0.427	0.532	0.593
Angle(degree)	92.0	114.0	136.0	158.0	180.0
$\delta p_{\parallel}$ (keV/c)	0.527	0.485	0.442	0.411	0.399
$\delta p_{\perp}$ (keV/c)	0.586	0.467	0.356	0.300	0.292
q=1e					
Angle(degree)	0.0	11.0	22.0	33.0	44.0
$\delta p_{\parallel}$ (keV/c)	0.280	0.293	0.318	0.353	0.387
$\delta p_{\perp}$ (keV/c)	0.207	0.218	0.256	0.325	0.434
Angle(degree)	136.0	147.0	158.0	169.0	180.0
$\delta p_{\parallel}$ (keV/c)	0.287	0.264	0.248	0.238	0.234
$\delta p_{\perp}$ (keV/c)	0.304	0.233	0.208	0.208	0.210

Table 4.4: The momentum resolution of ions emitted in the upper half of YZ plane with the presence of the 10 V patch. The standard deviations of TOF (IR) of MCP and x-ray are included in calculating $\delta p_{\parallel}$ ($\delta p_{\perp}$).

q=2e					
Angle(degree)	0.0	22.0	44.0	66.0	88.0
$\delta p_{\parallel}$ (keV/c)	0.440	0.458	0.499	0.527	0.522
$\delta p_{\perp}$ (keV/c)	0.294	0.328	0.426	0.532	0.595
Angle(degree)	92.0	114.0	136.0	158.0	180.0
$\delta p_{\parallel}$ (keV/c)	0.520	0.480	0.439	0.410	0.400
$\delta p_{\perp}$ (keV/c)	0.587	0.467	0.355	0.300	0.293
q=1e					
Angle(degree)	0.0	11.0	22.0	33.0	44.0
$\delta p_{\parallel}$ (keV/c)	0.280	0.290	0.313	0.347	0.379
$\delta p_{\perp}$ (keV/c)	0.208	0.217	0.255	0.324	0.435
Angle(degree)	136.0	147.0	158.0	169.0	180.0
$\delta p_{\parallel}$ (keV/c)	0.285	0.263	0.248	0.237	0.234
$\delta p_{\perp}$ (keV/c)	0.302	0.233	0.208	0.208	0.211

Table 4.5: The momentum resolution of ions emitted in the lower half of YZ plane which is close to the path with potential of 10 V. The standard deviations of TOF (IR) of MCP and x-ray are included in calculating $\delta p_{\parallel}$ ($\delta p_{\perp}$).

4.4 Systematic Effects of Eddy Current Suppression Slots in Electrodes

In HUNTER, the MOT coils must be periodically switched on/off to allow electron data collection, because the MOT coil fields are not compatible with electron collection. This switching will induce eddy currents in the electrodes. These induced eddy currents produce a magnetic field which continues to disturb the electron trajectories. To reduce this eddy current magnetic field, electrodes were proposed to be split radially to suppress the eddy currents. In this 3-D simulation, the electrodes are split into four pieces because of the fourfold symmetry used to reduce the RAM required for the simulation.

If the electrodes were slit across the full radial extent, the edges might develop a misalignment. To guard against this, insulated metal clamps were proposed to align the corners, as shown in Fig. 4.5b. The clamps could introduce a further complication in that they disturb the electric fields. In the simulation, the radial extent of the clamp is 10 mm, the width is 10 mm, and the full thickness along the symmetry axis is 3 mm. The clamps are set to the same potential as the associated electrode to prevent the floating potential. The clamp and the associated electrode are, however, isolated from one of the contacted electrodes to suppress eddy currents. For studying the variation of the electric field due to the clamps, two 3-D models were used to simulate the electric fields:

- 3-D model with supporting structures, as shown in Fig. 4.5a. The electrodes are split, but the clamps are not applied.
- Same as above, but the clamps are applied.

To see the effects of the clamps, the electric field is studied along a pair of circles with a radius of 60 mm at 454 mm and 464 mm from the MCP (the inner radius of the electrodes at these positions is 171 mm). These circles were chosen to be larger than any particle trajectory at their respective axial positions in order to show a visible effect from the clamps. The Z coordinates of these circles are aligned respectively with an electrode, and midway between two electrodes. The electric field is extracted at points that are 3 degrees of azimuth apart along these circles. The longitudinal electric fields E$_z$ and radial electric field E$_r$ of the two 3D simulations are compared, as shown in Fig. 4.6.

The azimuthal variation of the fields, as shown in Fig. 4.6, is due to the the slits and clamps. The field increases on average by a few nanoVolts/mm when the clamps are added [1] .

---

[1] The azimuthal variation does not have a 45 degree period because of the details of the

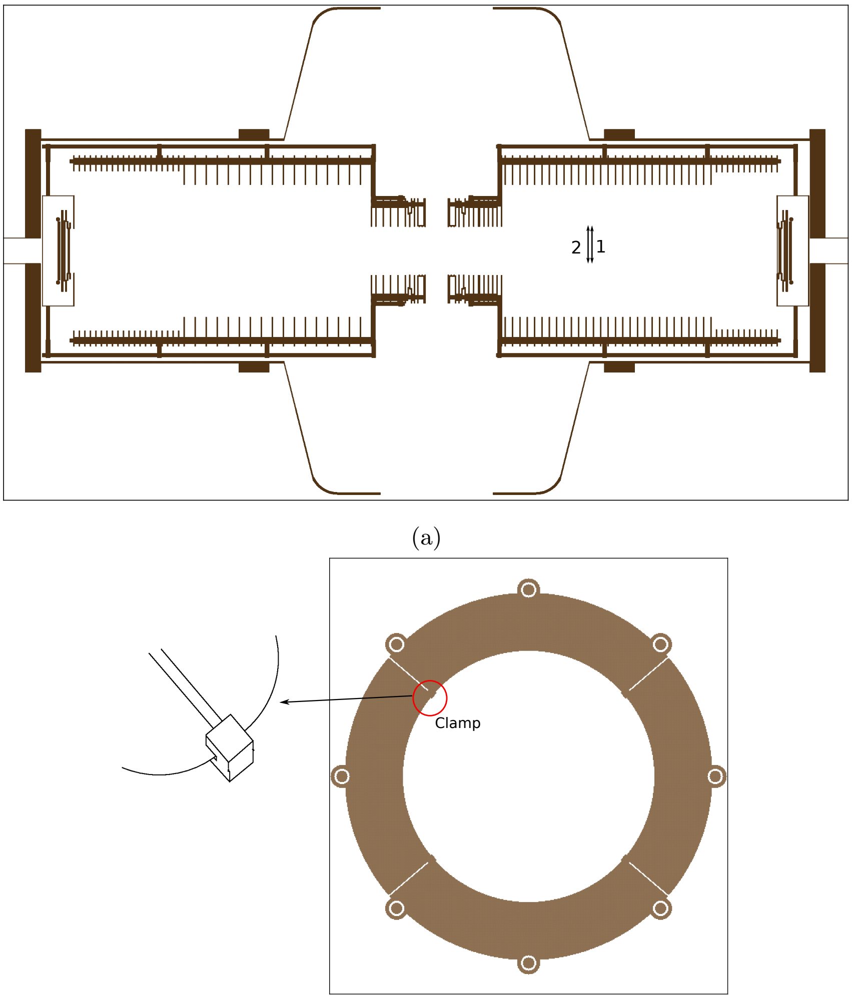

(a)

(b)

Figure 4.5: (a): Cross section of the 3-D model of the spectrometer constructed in SIMION. Two double-headed arrows are marked in the figure to indicate the positions of a pair of circles where the electric fields are extracted for studying the influence of the clamps. (b): Electrode with four slits, because of the fourfold symmetry used in constructing the model. The clamp is shown in the inset.

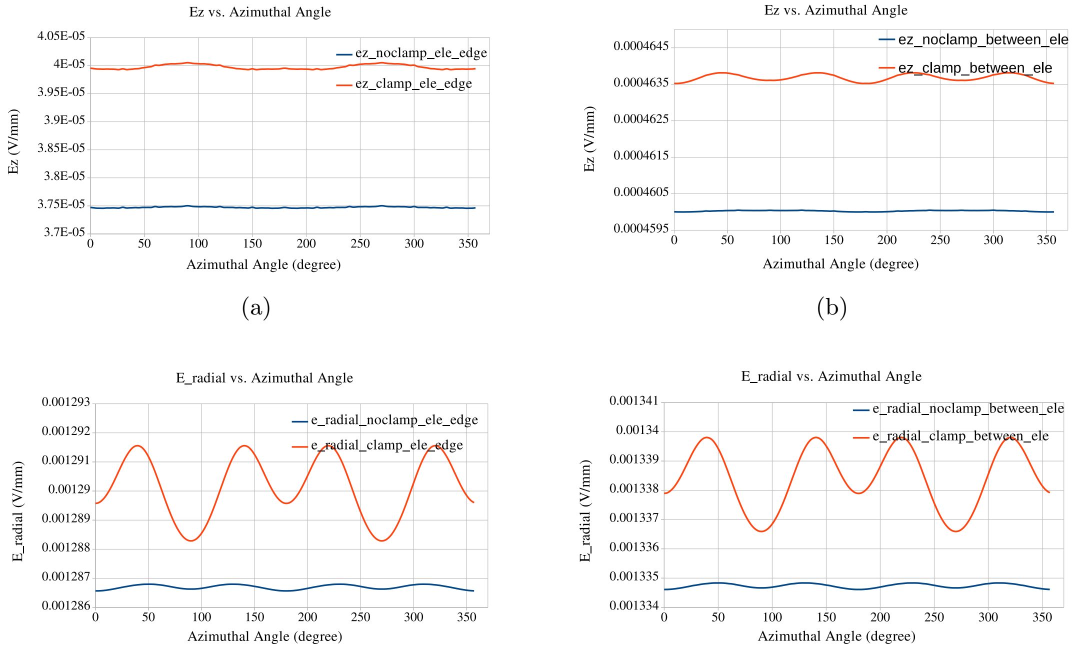

(a)

(b)

(c)

(d)

Figure 4.6: Comparisons of E_z and E_r with (orange) and without (blue) clamps. Panels (a) and (c) show the effect on a circle aligned with an electrode, while (b) and (d) show the effect midway between the two electrodes. The radial fields are the most strongly affected, but the effect is tiny, shifting on average by a few nV/mm and showing azimuthal variations of the same order.

An upper limit on the effects of these field variations on the momentum resolution was achieved by flying 2,000 ions of 352 keV/c with varying start positions in the MOT source and varying polar angles, half of them with an initial azimuthal angle of 0 degrees and half with an initial azimuthal angle of 42 degrees. These angles are associated with the crest and trough of the field variations. Ions were flown through both 3-D models described above (with and without clamps). The total momentum for the 2,000 ions was then reconstructed for both models and the resolutions were compared, as shown in Fig. 4.7. The effect on the resolution due to adding the clamps is generally small. The effect is largest for $p_\perp$ of ions emitted at 80-100 degrees to the symmetry axis, where the resolution is degraded by 30% of its value.

---

modeling. Due to the fourfold symmetry of the 3D model, only one quarter of each electrode is actually modeled. To avoid putting the slits through the lug that the supporting rods pass through, the azimuthal angle of the slit is set to 40.5 degrees. Therefore, the angle between any two slits in the fourfold-replicated electrode is either 81 degrees, or 99 degrees. Thus, the field variation due to the slits and clamps is not simply periodic.

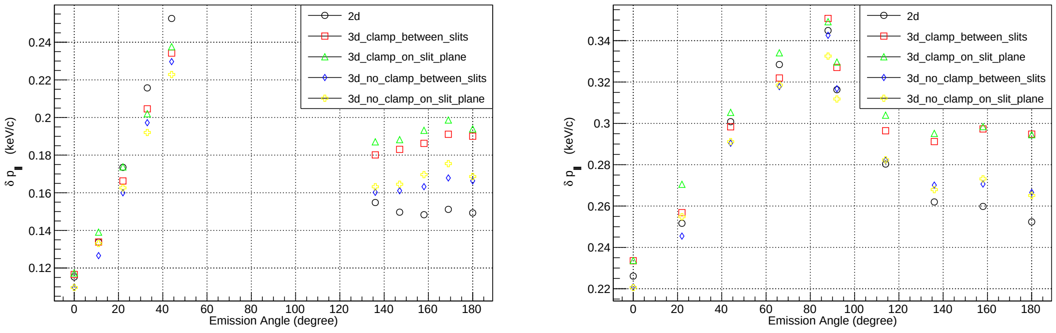

(a)
Comparison of $\delta p_{\parallel}$ of ions with charge 1e

(b)
Comparison of $\delta p_{\parallel}$ of ions with charge 2e

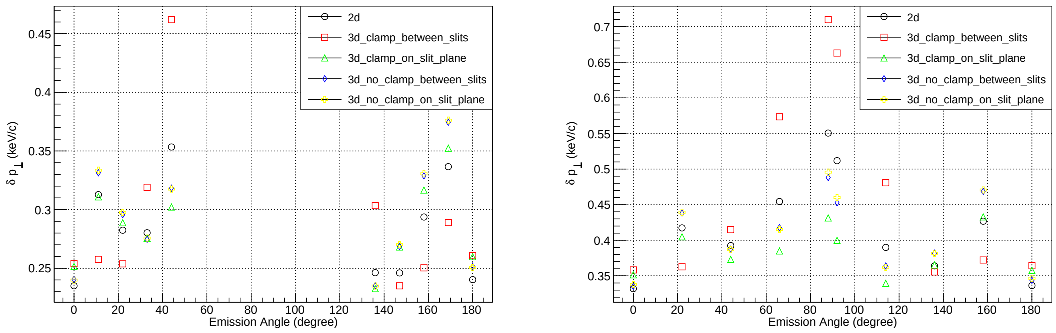

(c) Comparison of $\delta p_{\perp}$ of ions with charge 1e

(d) Comparison of $\delta p_{\perp}$ of ions with charge 2e

Figure 4.7: The comparison of the momentum resolutions calculated in the simulations listed in the legends of the figures. The labels in legends are explained below:
1. "2d" represents the data from a 2-D simulation, which serves as a reference.
2. "3d_clamp_between_slits" ("3d_clamp_on_slit_plane") represents the data for ions flown with an initial azimuthal angle of 0 (42) degree through the 3-D model with clamps.
3. "3d_no_clamp_between_slits" ("3d_no_clamp_on_slit_plane") represents the data for ions flown with an initial azimuthal angle of 0 (42) degree through the 3-D model without clamps.

4.5 Systematic Effect Due to Different Spacer Configurations

In the mechanical design of the spectrometer, spacers and washers with specific thicknesses are proposed to be placed between two electrodes to fix electrodes' positions. Three 3-D simulations with different spacer and washer combinations listed below were implemented to study their influence on the momentum resolution. The ceramic spacers were constructed in SIMION as electrodes with potential 0 (grounded). The spacer and washer configurations are described below:

1. electrode-ceramic-electrode ("ECE"): A ceramic spacer with a thickness equal to the distance between the back and front faces of two electrodes is positioned between them. The spacer is grounded to prevent floating potential.
2. electrode-metal-ceramic-electrode ("EMCE"): A metallic washer and a ceramic spacer with the thickness of half of the distance between the back and front faces of two electrodes are positioned between them. The potential of the washer is the same as the contacted electrode. The spacer is grounded to prevent floating potential.
3. electrode-metal-ceramic-metal-electrode ("EMCME"): A ceramic spacer is sandwiched between two metallic washers. The washers' potentials are the same as the contacted electrode. The spacer is grounded for the same reason.

The 10 groups of ions with different polar angles and the same azimuthal angle described in Section 3.7 were flown in these three simulations to evaluated the momentum resolution. The comparison of the resolutions for the different spacer and washer configurations is shown in Fig. 4.8

Fig. 4.8 shows that the different spacer configurations have negligible effect on the resolution for both $p_{\|}$ and $p_{\perp}$.

4.6 Systematic Effect due to Variations of Source Position

In the HUNTER experiment, ^{131}Cs atoms are suspended in a MOT formed by three pairs of counter-propagating laser beams [52, 53, 54, 84, 85]. The MOT center is supposed to be at the center of the spectrometers. However, the gravity of the ^{131}Cs atoms may shift the MOT center downward, and the forces exerted on the ^{131}Cs atoms by the laser beams may shift the

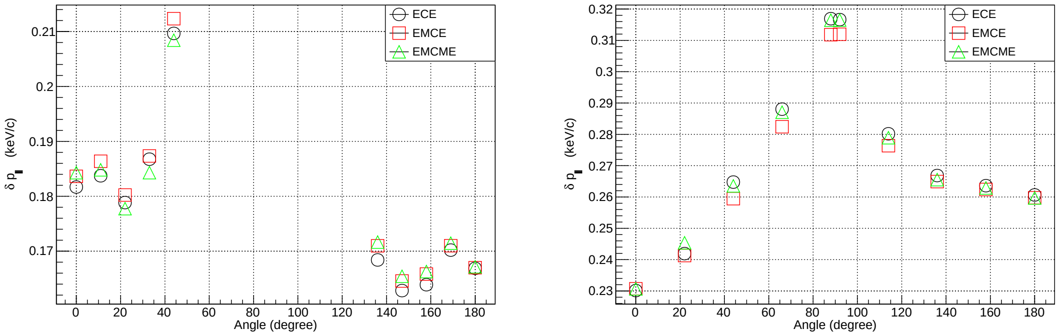

(a)
Comparison of $\delta p_{\parallel}$ of ions with charge 1e

(b)
Comparison of $\delta p_{\parallel}$ of ions with charge 2e

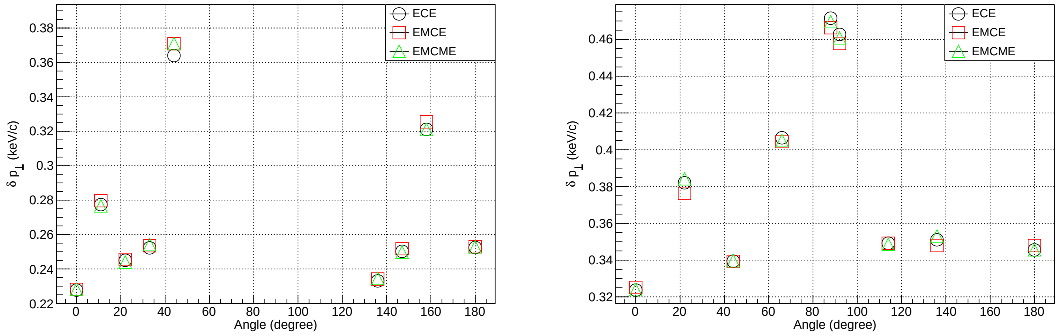

(c) Comparison of $\delta p_{\perp}$ of ions with charge 1e

(d) Comparison of $\delta p_{\perp}$ of ions with charge 2e

Figure 4.8: The comparison of the momentum resolutions for different spacer configurations.

MOT center in different directions in long term trapping. To evaluate the variation of the ion momentum resolutions due to the offset of the MOT center, 2-D simulations with the MOT center shifted by 1 mm and 2 mm in longitudinal and vertical directions were implemented. The doubly-charged ions of Set **A** introduced in Section. 3.5 with 1000 random initial positions were flown in these simulations. The average $\delta p_{||}$ and $\delta p_{\perp}$ of the 10 groups of ions in these simulations were compared to the optimized resolutions, and the variations are shown in Table. 4.6.

Longitudinal	resolution variation (%)	
	$\delta p_{\parallel}$	$\delta p_{\perp}$
+1 mm	15.1	0.02
+2 mm	32.5	12.9
-1 mm	-0.1	16.1
-2 mm	17.4	54.2
Vertical	resolution variation (%)	
	$\delta p_{\parallel}$	$\delta p_{\perp}$
+1 mm	50.4	50.3
+2 mm	111	102
-1 mm	-27.0	-19.3
-2 mm	-19.3	-17.8

Table 4.6: The variations of the ion momentum resolutions due to the offset of the MOT center are shown in the table. The positive (negative) offset in longitudinal direction means shifting the MOT center away from (toward) the ion MCP. In the vertical direction, the positive (negative) offset means shifting the MOT center opposite (along) the gravity direction. Degradation (Improvement) of the momentum resolution is represented as a positive (negative) percentage in the table.

The "Longitudinal" (upper) section of Table. 4.6 shows the variation of the ion momentum resolutions due to the offset of the MOT center in the longitudinal direction. The positive (negative) offset means shifting the MOT center away from (toward) the ion MCP. Degradation (Improvement) of the momentum resolution is represented as a positive (negative) percentage. The variation of $\delta p_{||}$ is positive because the time focusing length is optimized, so the minimum of TOF standard deviations occurs at the ion MCP. Changing the MOT center longitudinally degrades the TOF standard deviations.

The "Vertical" (lower) section of Table. 4.6 shows the variation of the ion momentum resolution due to the radial shift of the MOT center. The positive (negative) offset means shifting the MOT center opposite (along) the gravity direction. Shifting up the MOT center degrades $\delta p_{\perp}$ because it shifts the ion trajectories far away from the electro-static lens axis, which violates the paraxial approximation.

These results show that in order to maintain the neutrino mass resolution in HUNTER, the position of the MOT must be held constant to within 0.5 mm, which is feasible with the closed loop laser controls of the experiment.

4.7 Influence of Mesh

This section presents simulations of the variation of the time- and spatial-focusing due to the woven mesh in front of the ion MCP. The biased voltage of the front panel of the ion MCP must be ∼-2500 V for high ion detection efficiency. Compared to the voltage of the last spectrometer electrode facing the MCP, which is ∼ -100 V, a mesh is required to stop the electric field generated by the MCP from penetrating into the spectrometer. Theoretical estimation indicates that the micro-lens produced by the penetrating field from a small hole in a conductor extends to a range around 2-3 times the radius of the hole size [86]. In the 2-D model of the ion spectrometer, a virtual plane of thickness 0 at the same potential of the electrode facing the ion MCP was used to terminate the field lines, instead of a realistic mesh. For studying the influence of the micro-lens, the woven mesh with a center-to-center distance of 0.16 mm for the mesh cells and a wire diameter of 0.02 mm was modeled in SIMION, which is the type of woven mesh provided by RoentDek with the minimum cell size [87]. The potential array (PA) cell size of the SIMION model was set to 0.005 mm × 0.005 mm. The RAM for simulating the whole apparatus of HUNTER with such fine PA cell size is not accessible, and the computation time for such a simulation is not attainable either. Thus, five simulations with simplified structures of the spectrometer with the mentioned PA cell size were implemented to evaluate the deviation of the time- and spatial-focusing caused by the micro-lens of the mesh.

The general model used in the simulations is shown in Fig. 4.9. The electric fields in this model are comparable with the fields on both sides of the virtual mesh in the 2-D simulation. The gap between two electrodes is 0.05 mm and the thicknesses of electrodes are 0.01 mm. The potentials of the mesh and the MCP are -102 V and -2500 V respectively, according to the potential optimization. Thus, the electric field between the mesh and the MCP is ∼500 V/mm. The electric field between the endplate and the mesh is around 0.106 V/mm, which is the electric field close to the mesh in the 2-D simulation of the full HUNTER spectrometer.

In the 3-D model as shown in Fig. 4.9, the origin of coordinates for the simulation is at the center of the vertical wall of the grounded container behind the MCP. The distance from the center to the MCP is 0.3 mm and from the center to the mesh is 5.3 mm. In the first three simulations, the distance between the endplate and the mesh is changed to study the change of the field between them. In the fourth simulation, the width of the mesh is extended to be as large as L1, as shown in Fig. 4.9. In the last simulation, a similar model with larger dimension is constructed to study the variation of the field caused by the mesh.

Case 1 For the model corresponding to the data marked in blue, which is overlapped by other markers, in Fig. 4.10, the distance between the mesh and the endplate is 4 mm and the penetration of the field through the mesh changes the field in this "weak field region". The field at z = 9 mm is around 0.108 V/mm.

Case 2 For the model corresponding to the data marked in orange in Fig. 4.10, the distance between the mesh and the endplate is 9 mm, the field around z = 10.5 mm is uniform and it is equal to 0.106 V/mm.

Case 3 For the model corresponding to the data marked in yellow in Fig. 4.10, the distance between the mesh and the endplate is 19 mm, and the field z= 10.5 mm away from the mesh is uniform and equal to 0.106 V/mm.

Case 4 For the model corresponding to the data marked in gray in Fig. 4.10, the distance between the mesh and the endplate is 9 mm, but the width of the mesh is extended to L1. The field between z = 5.5 mm to z = 10.5 mm is different from the old model, but for the field beyond z = 10.5 mm, it is still around 0.106 V/mm. The model is shown in Fig. 4.11.

Case 5 For the model corresponding to the data marked in green in Fig. 4.10, the width L1 as shown in Fig. 4.9 is increased from 3 mm to $(3 + 0.16\times12)$ mm, where 0.16 mm is the cell-center

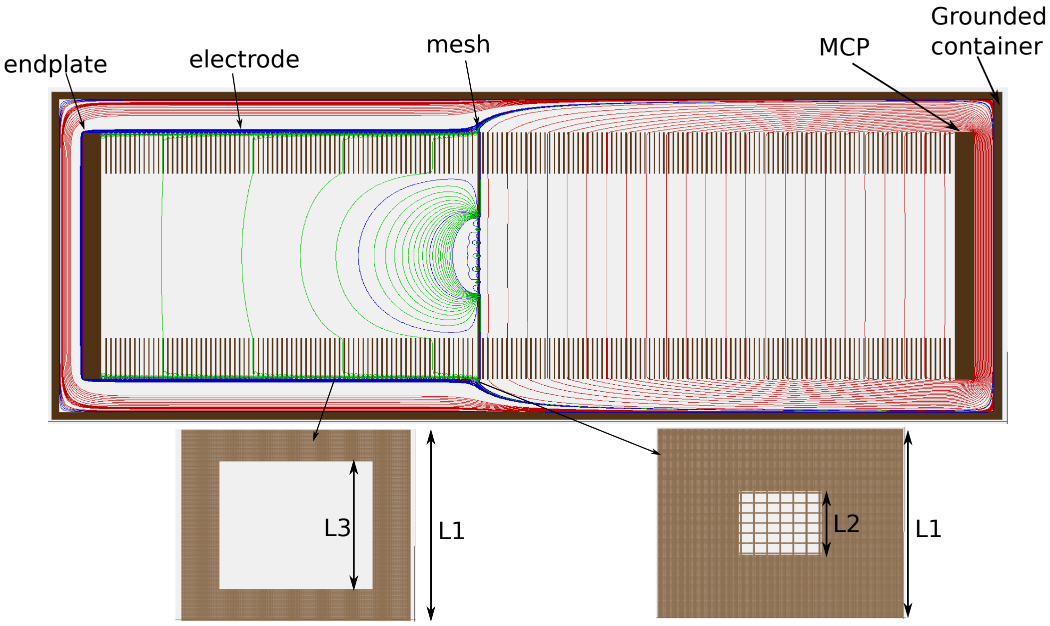

Figure 4.9: Cross section of the 3-D model. The potential differences between adjacent red, blue, green equipotentials are 100 V, 1 V, 0.1 V, respectively. The left inset is an electrode. The outer and inner side lengths are L1 and L3, respectively. The right inset is the mesh with 6×6 cells. The frame width of the mesh is (L1 - L2)/2. In the model, L1, L2 and L3 are 3 mm, 1 mm and 2 mm, respectively.

to cell-center distance of the mesh. The difference between L1 and L2, and L1 and L3 are still 2 mm and 1 mm, respectively. Thus, the cell number of the mesh in the vertical and horizontal direction have both been increased by an integer number. The model is shown in Fig. 4.12

Therefore, the conclusion of the comparison is that:

1. Introduction of mesh does not change the uniform field at the region far away from the mesh.
2. The field close to the mesh is the same in the first three simulations. So, the field is independent of the position of the endplate.
3. The field of the model corresponding to cases 2, 4 and 5 are different. Thus, the field close to the mesh is boundary-dependent, where a wider mesh means the mesh influence on the weak field extends farther away.

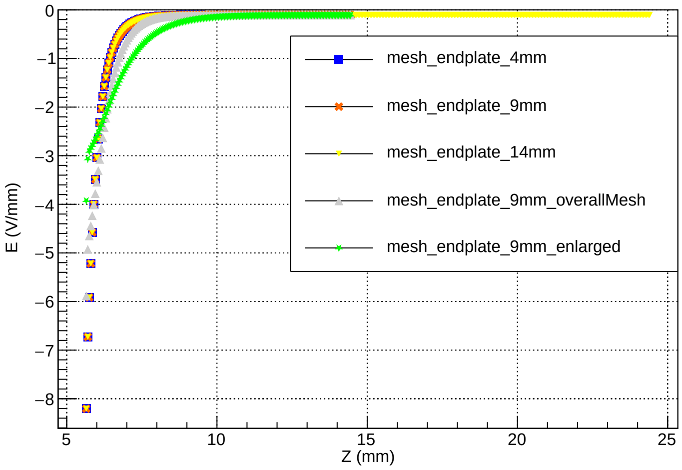

Figure 4.10: The variation of field along the line parallel to the symmetric axis and passing through the mesh cell at the center. The data marked in blue, orange, yellow, gray, green are associated with **Case 1**, **Case 2**, **Case 3**, **Case 4**, **Case 5**, respectively. The blue markers are overlapped by other markers.

In these five models, 5000 ions with initial positions randomly distributed in a square with dimension of 0.16 mm × 0.16 mm right in front of the endplate were flown to compute the standard deviation of TOF and impact radius. The axis of the square formed by the ions' initial positions was aligned with the axis of the mesh cell at the center of the mesh. The projection of the initial position and final position of ions to the mesh plane is shown in Fig. 4.13.

Doubly- and singly-charged ions are flown respectively to evaluate the TOF, IR, standard deviation of TOF and IR, and transmission rate of ions. For singly-charged (doubly-charged) ions, the initial kinetic energy is 89 eV (178 eV), which is from the 2-D simulation. According to the simulation data, 10% of ions are stopped by the mesh wires. The TOF standard deviations for doubly- and single-charged ions are 0.09 ns and 0.12 ns, respectively, which are smaller than the combined 1 ns TOF standard deviation of the x-ray detector, MCP and MOT size. Therefore

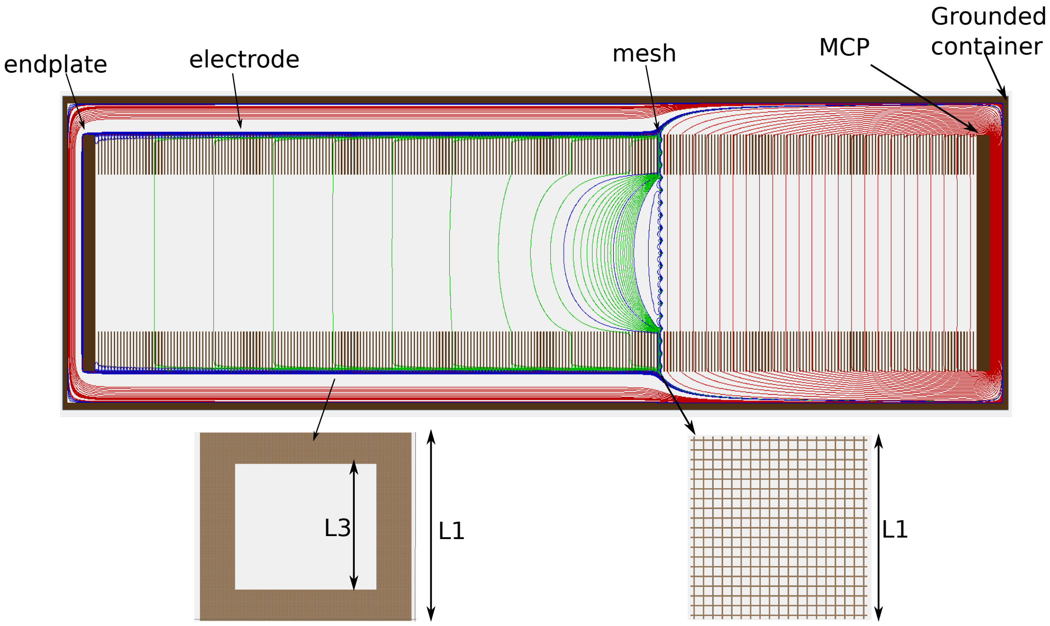

Figure 4.11: Illustration of the simulation model with full-width mesh. Square electrodes with outer side length of L1 and inner side length of L3 are used in the simulation. A frameless mesh with side length of L1 is used to separate two different electric fields represented in green and red.

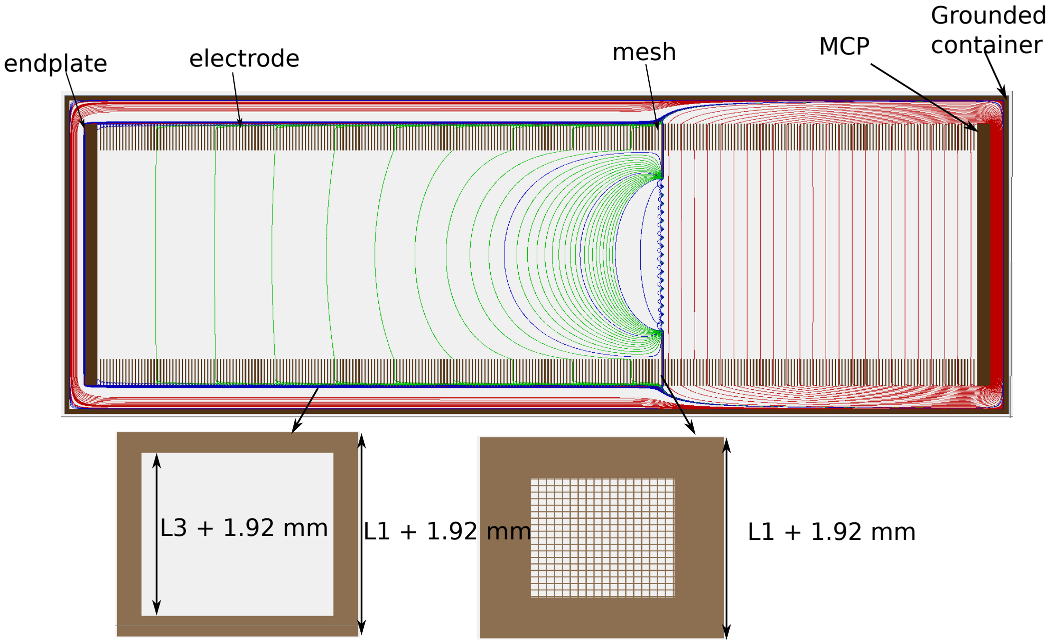

Figure 4.12: Illustration of the enlarged model similar to Fig. 4.11, but the side lengths of the electrodes and mesh are increased by 1.92 mm.

	q=1e			
	TOF_mean (ns)	TOF_std (ns)	IR_std (µm)	Transparency (%)
Case 1	443.14	0.12	33.7	89.7
Case 2	834.61	0.12	33.3	90.3
Case 3	834.60	0.12	34.0	90.2
Case 4	833.28	0.12	33.9	90.4
Case 5	834.16	0.12	33.6	89.8
Case 2 out most cell (Fig. 4.14)	835.07	0.17	33.6	90.0
ideal mesh	835.43	5.4×10^{-4}	46.5	100

	q=2e			
	TOF_mean (ns)	TOF_std (ns)	IR_std (µm)	Transparency (%)
Case 1	313.34	0.09	33.6	90.0
Case 2	590.15	0.09	33.4	90.3
Case 3	590.16	0.09	33.7	90.4
Case 4	589.22	0.09	33.7	89.3
Case 5	589.84	0.09	33.5	90.2
Case 2 out most cell (Fig. 4.14)	590.48	0.12	34.0	90.3
ideal mesh	590.74	3.8×10^{-4}	45.4	100

Table 4.7: The table lists the standard deviation of TOF and IR associated with the five models.

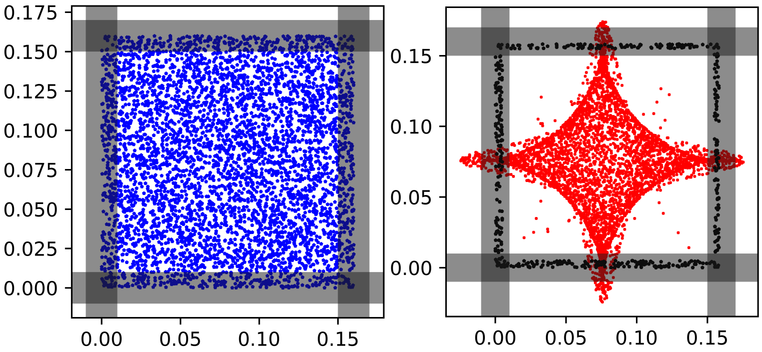

Figure 4.13: The projection of the ion trajectories penetrating the central cell of the accelerating mesh. The frames in gray color represent the wires of the woven mesh. Left: the projection of the initial ion position in the mesh plane. Right: the projection of the impact positions of ions, where the black star shape dots show where ions strike the mesh frame.

the variation of TOF due to the micro-lens of the mesh has limited influence on the $p_{||}$ resolution for HUNTER.

For ions with the distribution of initial position comparable to the cell size of the mesh, the standard deviation of IR after passing through the mesh cell is around 33 µm, which is comparable with the MCP spatial resolution. Therefore, the variation of the IR standard deviation caused by the micro-lens of the mesh can be tolerated in HUNTER. The distribution of the impact positions is shown in Fig. 4.13.

The trajectories of ions passing through the cells on edges of the mesh were slightly distorted, as the projection of impact positions shown in Fig. 4.14. This distortion only degrades the IR standard deviation by 1.5%, as shown in Table. 4.7. So, it can be tolerated in HUNTER.

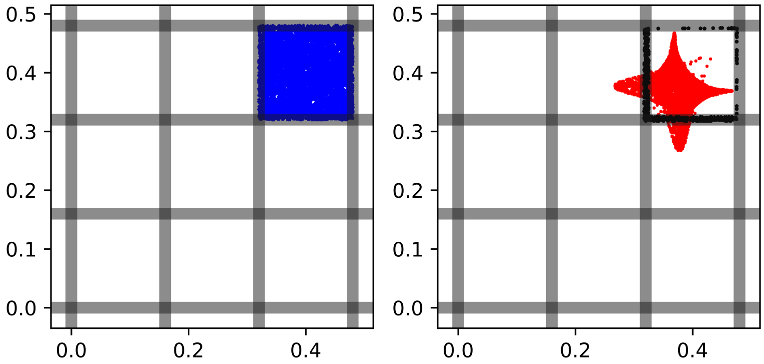

Figure 4.14: The projection of the ion trajectories penetrating a cell on the edge of the accelerating mesh. The frames in gray color represent the wires of the woven mesh. Left: the projection of the initial ion position in the mesh plane. Right: the projection of the impact positions of ions, where the black star shape dots are the ions striking the mesh frame. The trajectories were distorted for the ions passing through the cells on edges of the mesh by comparing the projection of impact positions in Fig. 4.13 and Fig. 4.14.

CHAPTER 5

SYSTEMATIC ERRORS DUE TO MECHANICAL DEFORMATION OF SPECTROMETER UNDER GRAVITY

This chapter studies the sagging of the supporting rods of the spectrometer under gravity, using a software called Autodesk Inventor. Deflections of a rod under its own gravity and a supported electrode were first simulated and compared to the theoretical calculations to prove the reliability of the software. The formulas for calculating deflections due to different loads can be found in Warren C.Young's book "Roark's Formulas for Stress & Strain" [88]. Then a model of the full spectrometer was simulated to see the importance of these effects.

5.1 Stiffness Improvement

To investigate the effectiveness of the spacers positioning the electrodes, we first compared the deflection of a rod with the spacer to the deflection of the rod due to its own weight, plus a concentrated force equal to the weight of the spacer. The stiffening results from "mating" the disk-shaped to the rod, effectively increasing the diameter of the rod to that of the disk for a distance equal to the thickness of the disk. Therefore, the disk in the above simulation was moved to a position 200 mm from the left end of the rod. The maximum deflection in this case was 0.57 mm as shown in Fig. 5.1a. Following this, the disk was removed and was replaced with a downward force equal to the weight of the disk. The resulting simulated deflection was 0.63 mm, which we consider to be marginally, significantly greater.

Thus, a mated disk-shaped spacer with a certain thickness can make the rod stiffer. The comparison between Fig. 5.2 and Fig. 5.3a also supports this conclusion.

In the concept of the spectrometer design of HUNTER, two supporting rings will be used to decrease the sagging of the supporting rods. A series of simulations were done to determine the position, the number, and the thickness of the supporting rings. The following paragraphs summarize the results of these simulations.

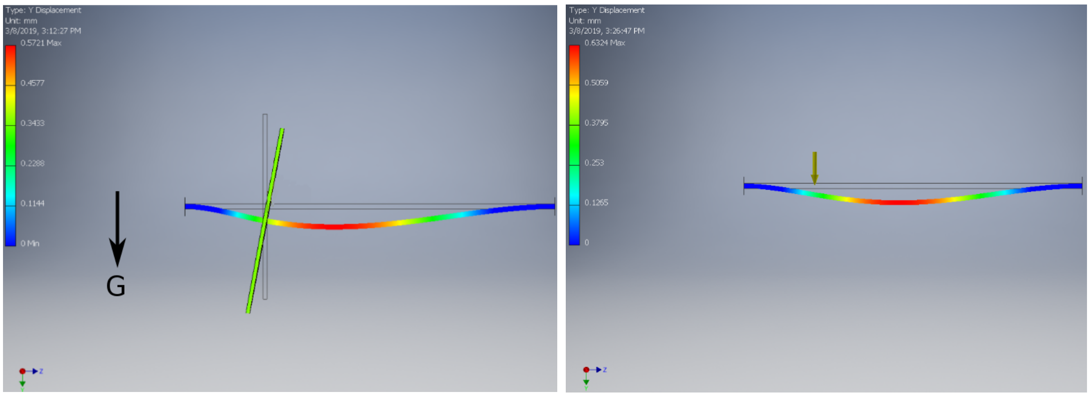

(a) (b)

Figure 5.1: Comparing the rod deflection due to the different loads. (a): The rod deflection due to its own weight plus the weight of the disk. (b): The rod deflection due to its own weight plus a concentrated force equal to the weight of the disk.

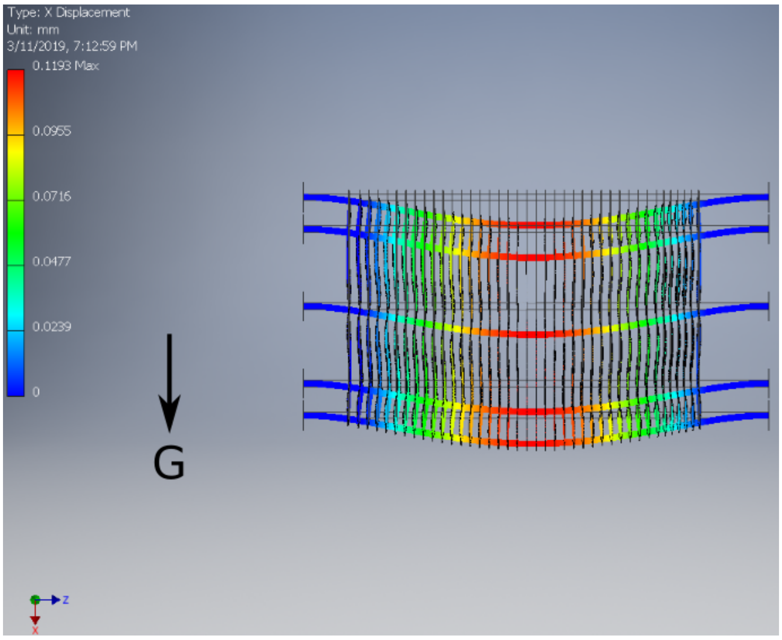

Figure 5.2: The rod deflection of the spectrometer without rings. In the simulation, the electrodes were supported by 8 rods. The two end surfaces of the supporting rods were "fixed".

1. The electrodes mated to the supporting rods are deformed by sagging. The electrodes with maximum horizontal deformation without supporting rings are those closest to the ends of the rods. The deformation of the electrodes at the center is much smaller. Therefore we will position a supporting ring between electrodes closest to the ends of the rods on both sides.
2. The thicker the ring is, the smaller the deflection is. Thus the thickness of the ring we used in the simulation is 19 mm, which is the largest gap between two electrodes.

Fig. 5.3a shows the deflection of the spectrometer. In this simulation the end surfaces of the 8 rods were fixed. To make the simulation more realistic, two "ears" (rings with a thickness of 10 mm and radial extension of 39 mm) were used to clamp the 8 rods instead of fixing their ends. The annular surfaces of the ears were fixed. The simulation result is shown in Fig. 5.3b.

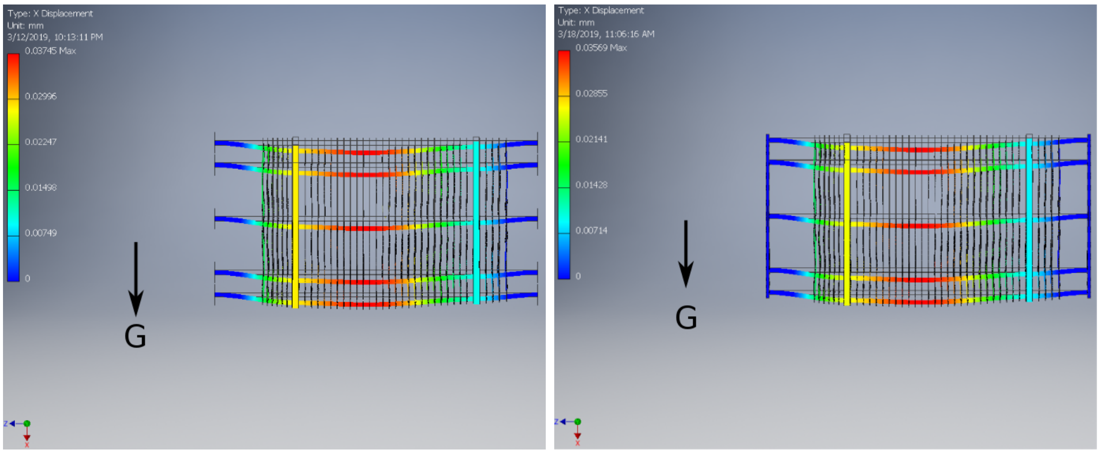

(a) (b)

Figure 5.3: Comparing the rod deflection of the different fixing methods. In this model, 8 rods pass through the electrodes and 4 supporting rings. (a): the two end surfaces of each rod are fixed. The maximum deflection as shown in the color bar is around 0.04 mm. (b): two "ears" are used to clamp the ends of the rods. In this simulation, the maximum deflection is around 0.04 mm.

The simulation results of these two fixing methods are roughly the same. The maximum deflection of the structure is around 30 µm. Table. 5.1 summaries the materials and dimensions of the components in each figure.

5.2 Spectrometer Deflection Under Gravity

The spectrometer structure constructed in Autodesk Inventor to study the deflection is based on a previous design, in which the materials of the components and the dimensions are different from current spectrometer design. In the spectrometer model, the spectrometer is only supported at

	component	Material	Thickness/ Length(mm)	OD (mm)	ID (mm)	deflection (mm)
Fig. 5.1a	single rod	stainless steel	1000	14	0	0.57
	disk	Al_2O_3	10	500	14	
Fig. 5.1b	single rod	stainless steel	1000	14	0	0.63
Fig. 5.2	8 rods	Al_2O_3	1000	14	0	0.12
	40 electrodes	Cu	0.5	500	realistic	
Fig. 5.3a	8 rods	Al_2O_3	1000	14	0	0.037
	2 rings	Al_2O_3	19	504	426	
	40 electrodes	Cu	0.5	500	realistic	
Fig. 5.3b	8 rods	Al_2O_3	1000	14	0	0.036
	2 rings	Al_2O_3	19	504	426	
	40 electrodes	Cu	0.5	500	realistic	
	2 ears	Al_2O_3	10	504	426	

Table 5.1: The detailed information of each component of the spectrometer. The inner diameters of electrodes are not listed because they have different values and the realistic inner radius is from a previous model.

its ends by two “ears”. 8 ceramic rods are passed through the ear plates and through the 40 electrodes at 250 mm from the central axis. In addition to the ear plates, two rings are placed close to the ends of the spectrometer. These were found to have a significant stiffening effect as presented above. Spacers are placed between electrodes to stop the electrodes from sliding along the rods. The spectrometer is shown in Fig.5.4. The detailed dimensions of the spectrometer are listed in the Table. 5.2.

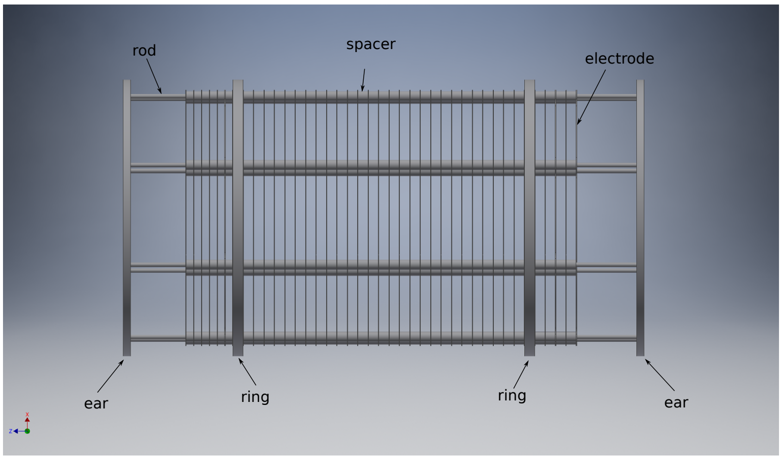

Figure 5.4: The figure shows the mechanical support structure of the spectrometer. The components are marked in the picture.

The concept of the design of the electrode is shown in Fig. 5.5. The slots in the electrodes were proposed to suppress the eddy current generated by the periodically varying magnetic field.

The spectrometer deflection due to gravity is shown in Fig. 5.6. The maximum deflection is around 53 µm and the largest deformation of the rods happens at the end of the rods. The maximum deformation of the electrodes in the horizontal direction is around 5 µm. These very

	component	Material	Thickness/ Length (mm)	OD (mm)	ID (mm)	deflection (mm)
Fig. 5.4	8 rods	Al_2O_3	1000	9	0	0.053
	2 rings	Al_2O_3	19	530	426	
	40 electrodes	bronze	1	480	realistic	
	2 ears	Al_2O_3	14	530	426	
	48 spacers	Al_2O_3	14	30	9.01	
	248 spacers	Al_2O_3	19	30	9.01	

Table 5.2: The detailed information of each component of the spectrometer.

small deflections indicate that the proposed design is mechanically stiff enough to achieve the HUNTER resolution goals.

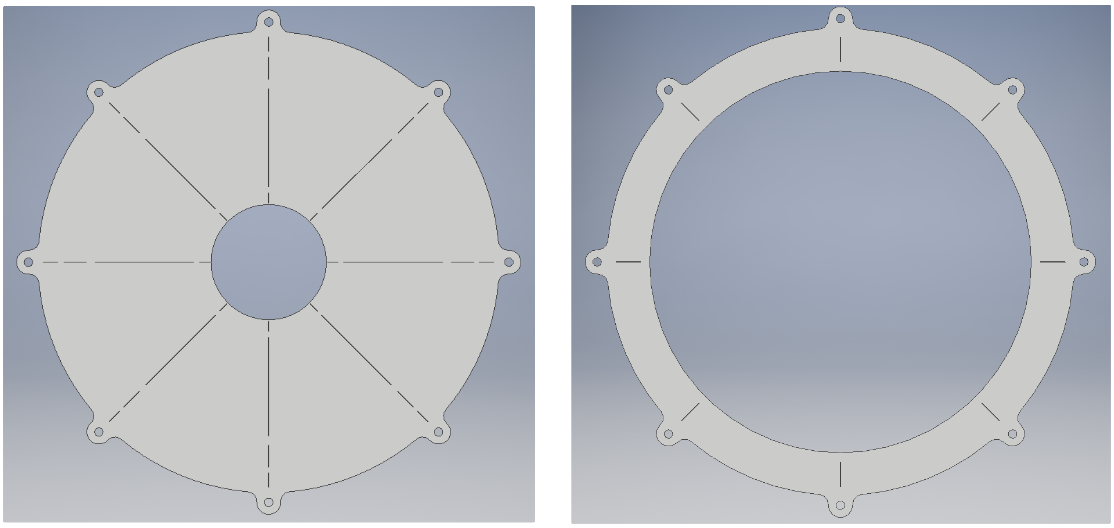
(a)

(b)

Figure 5.5: The concept of the electrode design is shown in the figures.

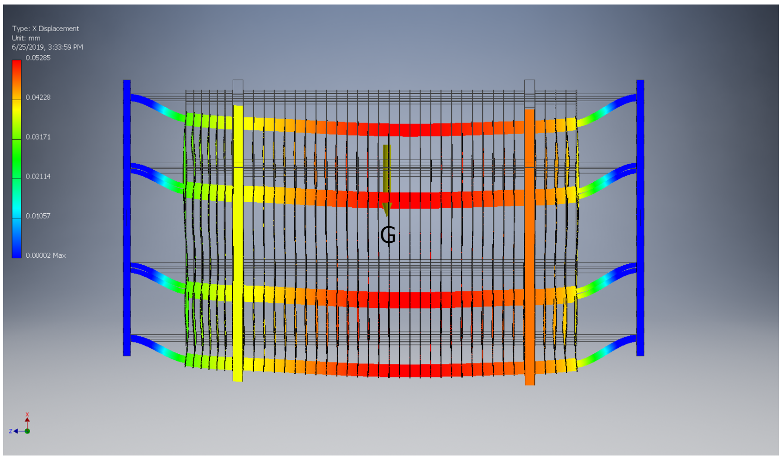

Figure 5.6: The figure shows the spectrometer deflection. The yellow arrow indicates the direction of the gravity. The maximum deflection indicated by the color bar is around 0.05 mm

CHAPTER 6

MAGNETIC FIELDS IN HUNTER

This chapter studies the various magnetic fields in the HUNTER Experiment, including the magnetic field generated by the anti-Helmholtz coils of the MOT and the transient magnetic field generated by the eddy currents induced by periodically switching on/off of the MOT coils. Different designs and materials of electrodes of the spectrometer were studied to investigate their ability to suppress the eddy current.

6.1 MOT Coils

In HUNTER, the MOT suspending ^{131}Cs atoms consist of an "optical molasses" formed by three pairs of orthogonal counter-propagating laser beams and a quadrupole field created by coils in anti-Helmholtz configuration [89, 90, 91]. Frequencies of the laser beams ω_l are red-detuned to the atomic resonance frequency ω_R. Therefore only atoms moving opposite to the propagating direction of the laser beams will be excited to a higher energy level. The de-excitation of the atom emits light isotropically in 4π solid angle, which slows down the atom since the net momentum of the photons emitted in the excitation and de-excitation transition cycle is zero. The force exerted on atoms is attributed to the incident laser beam, as shown in Eq. 6.1 [53, 85]

$$\boldsymbol{F}_{\pm} = \hbar \boldsymbol{k} \frac{\Gamma}{2} \frac{I/I_{sat}}{1 + I/I_{sat} + 4(\delta \mp \boldsymbol{kv})^2/\Gamma^2} \tag{6.1}$$

where Γ is the decay rate of the excited state. $\delta = \omega_l - \omega_R$ represents the detuning of the laser. The I/I_{sat} is the laser beam intensity to the saturation intensity of the excited state, where $I_{sat} = \pi hc\Gamma/(3\lambda^3)$. $\boldsymbol{v}$ is the velocity of the atom and $\boldsymbol{kv}$ is the Doppler shift in the rest frame of the atom. $\mp$ depends on the direction of the motion of the atoms.

Under the assumption $I \ll I_{sat}$, the stimulated emission can be ignored. To simplify the force acting on an atom from counter-propagating beams, we assume that $\boldsymbol{kv} << \Gamma$

$$\boldsymbol{F}_{OM} = \boldsymbol{F}_{+} - \boldsymbol{F}_{-} = -\frac{1}{\Gamma} \frac{I}{I_{sat}} \frac{8\hbar k^2 \delta}{(1 + 4\delta^2/\Gamma^2)^2} \boldsymbol{v} = -\beta \boldsymbol{v} \tag{6.2}$$

This velocity related force dampens the atomic motion to the Doppler cooling limit $\hbar\Gamma/2k_B$.

However, this so-called optical molasses only cools down the atoms. The atoms will diffuse out after being trapped for a period of time. Thus, a restoring force is required to pull the escaping atoms back to the intersection region of the laser beams. This restoring force is provided by the interaction of circularly polarized laser light with atoms Zeeman-split by a quadrupole magnetic field generated by a pair of coils with inverse currents as shown in Fig. 6.1a

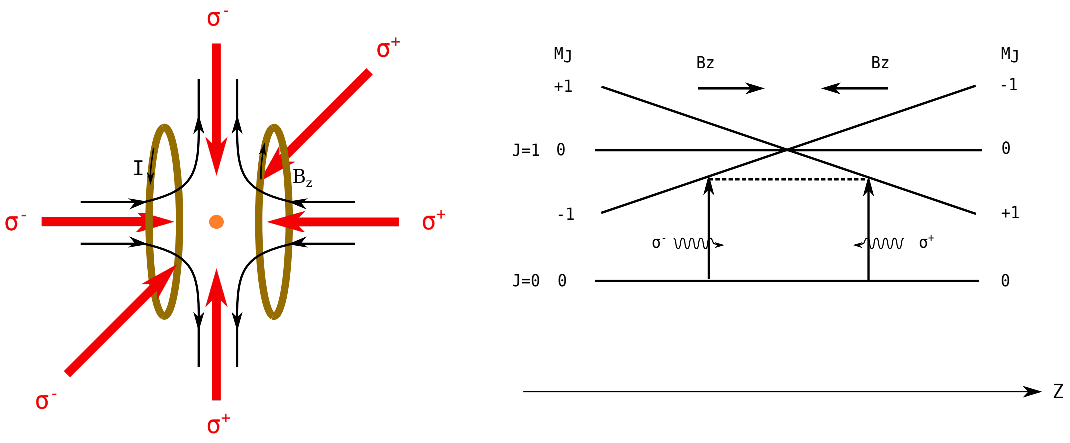

(a)

(b)

Figure 6.1: A typical configuration of a MOT. (a): A MOT consists of an arrangement producing both velocity damping (optical molasses) and a restoring force. (b): Schematic spectral splittings of a two-level atom.

A quadrupole magnetic field generated by anti-Helmholtz coils has zero field strength at the center, and a linearly increasing field away from the center. Escaping atoms will see an increase of the magnetic field along the paths. For a typical two-level atom with an angular moment J = 0, 1, the J = 1 energy level splits into three magnetic field dependent sub-levels M_J = -1, 0, 1, because of the Zeeman effect. The excited state of $M_J = -1$ is shifted down when $B < 0$ as shown in Fig. 6.1b. The shift of the atomic energy level due to the magnetic field is

$$\Delta E = -\boldsymbol{\mu}\boldsymbol{B} = -g_F \mu_B B M_F \tag{6.3}$$

where M_F is the Z component of the total atomic angular momentum $\boldsymbol{F} = \boldsymbol{J} + \boldsymbol{I}$, $\boldsymbol{J} = \boldsymbol{L} + \boldsymbol{S}$ is the total electron angular momentum. $\boldsymbol{\mu} = \mu_B(g_L\boldsymbol{L} + g_S\boldsymbol{S} + g_I\boldsymbol{I})$, considering the nuclear magnetic moment. The quantities g_L, g_S, and g_I are the g factors related to electron orbital motion, electron spin, and nuclear spin, respectively. $\mu_B = \hbar q/2m_e$ is the Bohr magneton. The hyperfine Landé g-factor g_F with respect to Landé g-factor g_J is [92, 93]

$$\begin{aligned} g_F &\approx g_J \frac{F(F+1) - I(I+1) + J(J+1)}{2F(F+1)} \\ &\approx (1 + \frac{J(J+1) + S(S+1) - L(L+1)}{2J(J+1)}) \frac{F(F+1) - I(I+1) + J(J+1)}{2F(F+1)} \end{aligned} \tag{6.4}$$

When including the Doppler effect and also the Zeeman effect into Eq. 6.1, the detuning for each laser beam becomes $(\delta \mp kv \mp \boldsymbol{\mu B}/\hbar)$. The net force acting on an atom can be written as

$$\boldsymbol{F} = -\beta\boldsymbol{v} - \beta\frac{\hat{k}}{k}\frac{g_F\mu_B BM_F}{\hbar} = -\beta\boldsymbol{v} - \kappa(z\hat{k}) \tag{6.5}$$

where $\hat{k}$ and k are the unit vector and the magnitude of $\boldsymbol{k}$, respectively. $\kappa = \beta g_F \mu_B A M_F/(\hbar k)$. The second term works as a restoring force pulling atoms back from escaping the optical molasses. The magnetic field B around the center of the MOT can be approximated as $B = A \cdot z$, where A is the magnetic field gradient which can be evaluated from the critical damping condition $\beta^2 - 4M\kappa = 0$ of a damped harmonic oscillation [94] and M is the mass of the atom.

If we assume that $I/I_{sat} = 0.1$, $\delta/\Gamma = -1/2$, and substitute the quantum number of the excited state $6^2P_{1/2}$ of ^{131}Cs atoms into the critical damping condition, we have a magnetic field gradient around -8.4 G/cm, which is in the typical range of the field gradient mentioned in Ref. [95, 96]. The corresponding oscillation frequency is ~1.3 kHz, which is also consistent with the typical values for the magnetic gradient [52].

In the HUNTER experiment, the anti-Helmholtz coil on each side consists of 16 turns of square wires forming a 4 × 4 array. The cross section of the square wire is 4.4 mm × 4.4 mm with a 2 mm diameter hole at the center. The current of each turn is 28.14 A, for achieving the designed magnetic field gradient. The innermost turns of the two coils have radius 69 mm and are separated by 66 mm. Eq. 6.6 shows the theoretical formula for the magnetic field generated by a single turn coil [97].

$$B_\rho = \frac{\mu_0 I}{2\pi\rho} \frac{z-b}{[(a+r)^2 + (z-b)^2]^{1/2}} [-K(\phi^2) + E(\phi^2)\frac{a^2 + r^2 + (z-b)^2}{(a-r)^2 + (z-b)^2}] \tag{6.6a}$$

$$B_z = \frac{\mu_0 I}{2\pi} \frac{1}{[(a+r)^2 + (z-b)^2]^{1/2}} [K(\phi^2) + E(\phi^2)\frac{a^2 - r^2 - (z-b)^2}{(a-r)^2 + (z-b)^2}] \tag{6.6b}$$

$$\phi^2 = \frac{4ar}{(a+r)^2 + (z-b)^2} \tag{6.6c}$$

In the calculation, the coil is in the XY plane and the Z axis is the central axis of the coil. a and b represent the radius and the Z coordinate of the coil, respectively. K and E are the elliptic functions. *Mathematica* was used to calculate the magnetic field and field gradient of the anti-Helmhotz coils described above with results as shown in Fig. 6.2.

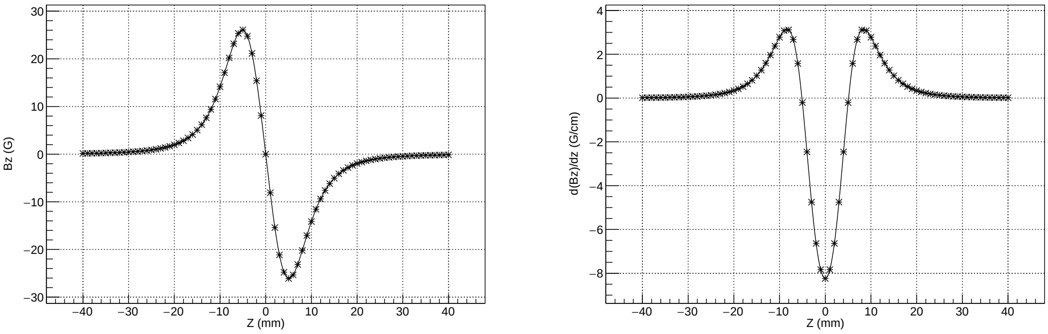

(a) (b)

Figure 6.2: (a): The axial component of the calculated magnetic field produced by the anti-Helmholtz coils with 4 × 4 turns of wires in each coil. The current in each turn of wire is 28.14 A. (b): The gradient of the field in (a).

In HUNTER, there is an 8 G magnetic field generated by the solenoids outside the spectrometer chamber for confining electron trajectories, which shifts up the magnetic field at the MOT center by 8 G. The zero magnetic field at the center can be restored by applying biased currents to the anti-Helmholtz coils as shown in Fig. 6.3, if the currents are set to 33 A and -42 A for coils on each side, respectively. The extent of the linear gradient region with unbalanced currents is more than sufficient for the MOT trapping field.

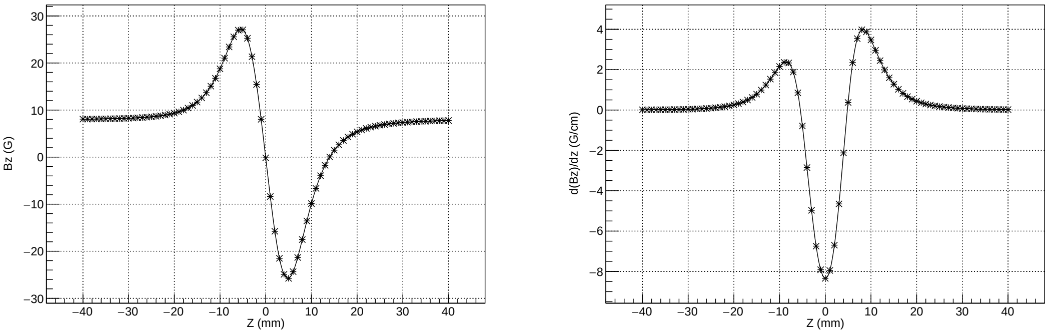

(a) (b)

Figure 6.3: (a): The magnetic field produced by the anti-Helmhlotz coils with biased currents plus the 8 G external magnetic field. (b): The gradient of the field in (a).

Even though the center of the MOT is shifted back by applying the biased currents, electrons still see the superposition of the 8 G magnetic field and the field generated by the MOT. The MOT field acts as a magnetic mirror, greatly reducing the collection efficiency of the electron spectrometer. To avoid the interference of the field from the MOT coils with the electron trajectories, the MOT coils will be cyclically switched on and off with a 50% duty factor, recording data only during the off part of the cycle. However, this switching on/off cycle may introduce other complications, such as vibration of the MOT coils due to the fluctuating magnetic forces, and induction of eddy currents in the electrodes.

6.2 Magnetic Force on Coils

To study the magnetic force on the coils, a 2-D model of the spectrometer was constructed in a finite element analysis software called "COMSOL" [98], as shown in Fig. 6.4. The details of the coil on one side of the MOT are shown in the inset. The space enclosed in the outermost circle is the "simulation world". The two concentric circles are a COMSOL construct called an "infinite domain", which simulates the boundary conditions of fields in an infinite domain. Smaller electrodes made of titanium [99] with a thickness of 0.3 mm were simulated in this model. Only one large electrode made of bronze with a thickness of 0.6 mm was included on each side of the spectrometer. The rest of the large electrodes were not modeled because they have limited influence on the problem. In COMSOL, the magnetic force can be evaluated from the integration of surface stress tensor or from the volume Lorentz force [100], and either of these methods requires a very fine mesh for achieving an accurate result. In the simulation, the mesh size of the coils is set to "extremely fine", as defined in COMSOL.

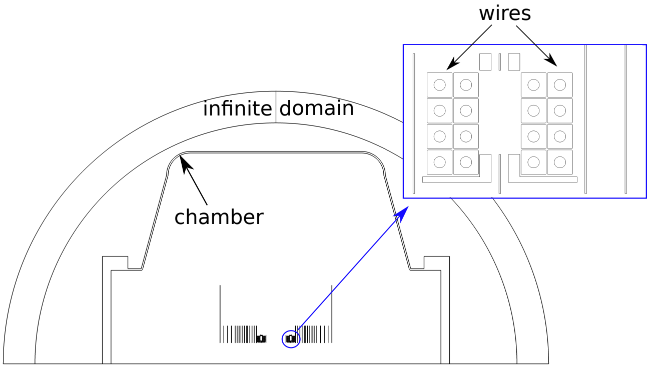

Figure 6.4: A truncated 2-D model of the spectrometer. The inset shows the details of the MOT coils on one side.

Given the possibility of producing a large magnetic force by induced currents in electrodes in the vicinity of the MOT coils during the transition zone of the driving current, time dependent simulations were implemented to study the force variation over time. Fig. 6.5a shows the driving current of the coils with a typical transition time of 100 µs. The axial magnetic field at $z = 55$ mm, where the maximum magnitude of the axial magnetic field is, is shown in Fig. 6.5b. The time dependence of the magnetic field generally follows the pattern of the driving current.

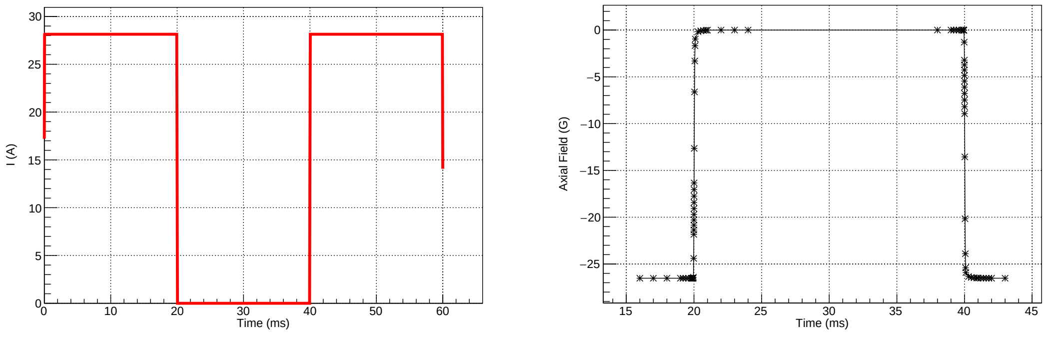

(a)

(b)

Figure 6.5: (a): The switching cycle of the MOT coils current with a transition time of 100 µs. (b): Time dependence of the axial magnetic field at $z = 55$ mm. The peak value of the axial magnetic field is around 26 G.

The axial magnetic force acting on the coil on the ion side is shown in Fig. 6.6. The magnetic force increases suddenly when the coils are turned on at $t = 40$ ms, which is due to the interaction of the driving current in the coil and the field of the opposing coil, as well as the induced eddy current in the electrodes considering its direction. The reaction force acting on the electrode next to the coil in the downstream direction of the spectrometer is shown in Fig. 6.6b. The interaction force was not observed at $t = 20$ ms in Fig. 6.6a because it is in the same direction as the force due to the other coil.

The sudden escalation of the magnetic force at $t = 40$ ms in Fig. 6.6a is small compared to the coil's force at the stationary state, and will not cause a shift of the coils. The decay of the eddy current inside the electrode can be understood from the decay of the force acted on the electrode shown in the red fitting curve $f = -exp(p0 + p1 \cdot t)$ in Fig. 6.6b because the variation of the force depends on the eddy current induced in the electrode. The time constant is $t = 1/p1 = 45$ µs. This time constant is 11 times larger than the simple estimation for a single electrode discussed in Section. 6.3.2 below. The difference may be due to the mutual inductance of the electrodes in the simulation.

The force between the coils in the stationary state can be calculated theoretically as shown below

$$\boldsymbol{dF} = Id\boldsymbol{L} \times \boldsymbol{B} = IdL\hat{\varphi} \times (B_z\hat{z} + B_\rho\hat{\rho}) \tag{6.7}$$

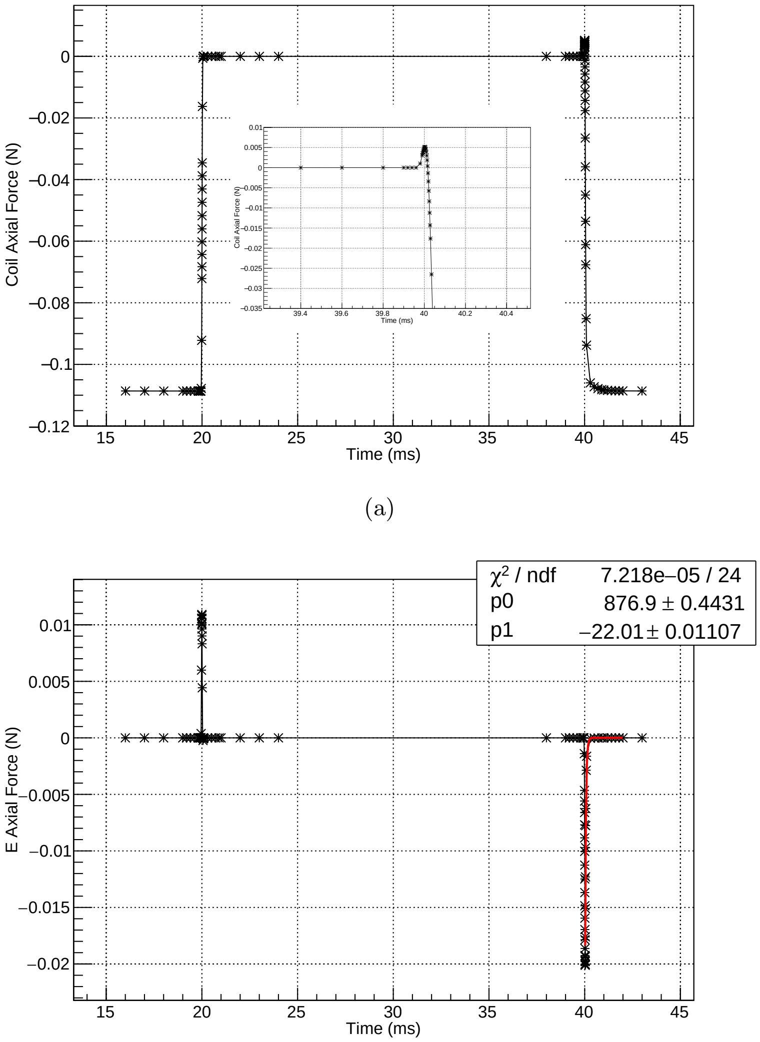

(a)

(b)

Figure 6.6: (a): Axial force acting on the coil. (b): Force acting on the electrode next to the coil in the downstream direction of the spectrometer. The force after switching on the coils is fitted with an exponential to study the decay time constant of the eddy current inside the electrode given that this force is the repulsion caused by the eddy current and the coil current.

where dL is an arc element of the coil along azimuthal direction. B_z and B_ρ are the axial and radial component, respectively. The net radial force, which is the integration of $\hat{\varphi} \times B_z \hat{z}$ over 2π, is zero. The axial force from the second integration is around 0.11 N, which is consistent with the simulation result.

For the biased current situation, the simulated force is around 0.19 N, which is consistent with the calculation. The force acting on a single turn of the coil depends on its position, and it is smaller than the net force acting on the coil as a whole.

6.3 Eddy Current Magnetic Field

6.3.1 Slotted Electrodes

Given the mutual inductance between the coils and the electrodes in the vicinity of the coils, periodically switching on/off the MOT coils will induce eddy currents in the electrodes. The eddy currents die out with a time constant $t = L/R$ (L is self-inductance, R is resistance) but produce their own magnetic fields which may disturb the trajectories of electrons. To avoid unduly disturbing the electron trajectories, simulations indicate that the induced magnetic field should be kept under 30 mG, according to Geant4 simulations of electron trajectories. 3-D COMSOL simulations with different materials for various spectrometer components and different electrode configurations were performed to study the constructions required to keep the eddy current fields below this value.

The truncated spectrometer model discussed in Section. 6.2 above was used in these simulations to save computation time. The cross-section view of the simplified model is shown in Fig. 6.7. A portion of large electrodes of the two spectrometer arms are not included in the simulations because the magnetic field generated by the coils is negligible in the region where the large electrodes are located, so the induced eddy currents in these electrodes are too small to produce an effective eddy current magnetic field.

To suppress the eddy current magnetic field, the electrodes are proposed to be split since this can diminish the induced eddy currents in the electrodes. To study the effectiveness of splitting electrodes, various proposals of splitting electrodes were considered in the simulations, as shown in Table. 6.1. In these simulations, bronze and stainless steel were used for the supporting rings to study the eddy current magnetic field contributed by them. Bronze is used for the electrodes with different slot configurations.

Time dependent COMSOL simulations were performed to find the induced magnetic field as

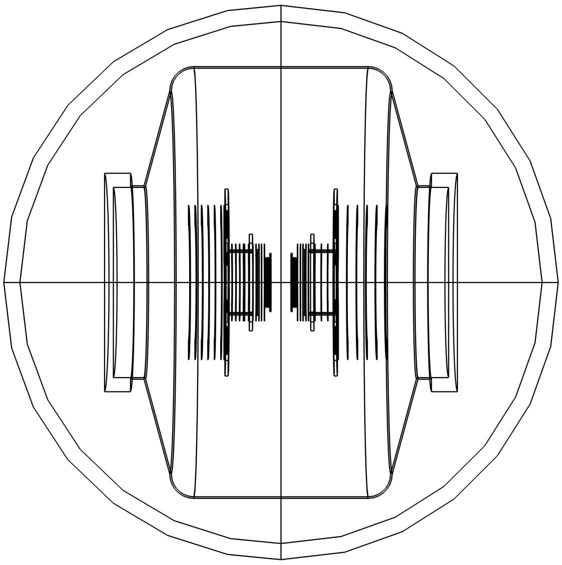

Figure 6.7: The cross-section view of the simplified spectrometer model. This model is based on an old design of the spectrometer, but the conclusion still stands.

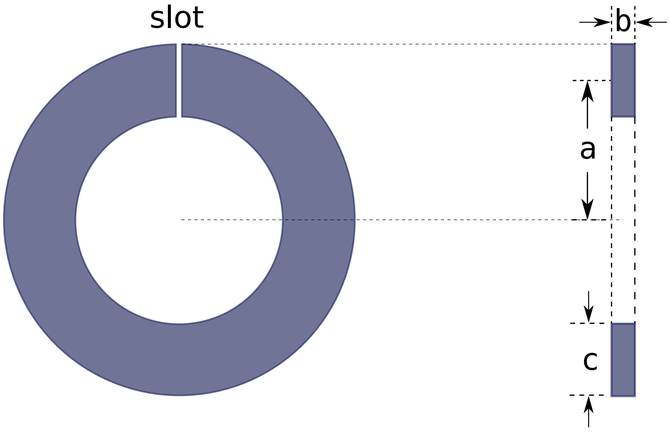

Figure 6.8: Left: Illustration of a C-shaped electrode. Right: Cross section of the electrode. For small electrodes, a, b and c are 93 mm, 0.3 mm and 54 mm, respectively.

slot condition	Eb_Rb	Eb_Rs
one full radius slot on E	Y	Y
one full radius slot on E & R	N	Y
two full radius slots on E	Y	Y
one partial radius slot on E	N	Y

Table 6.1: This table gives a matrix indicating all the different simulations that were done to study the abatement of eddy current effects. All the simulations in a given row share the same slot geometry and differ in which components were simulated or in the materials used. For the first row, each annular electrode has one full-radius slot, i.e. the electrodes are C-shaped, but the support rings are fully intact, as shown in Fig. 6.8. For the second row, electrodes and supporting rings are both full-radius slotted. For the third row, each electrode has two full-radius slots along a diameter, dividing the electrode into two equal halves. For the last row, the electrodes have partial radius slots, leaving a 2 mm radial thickness bridge across the outer edge of the gap in the C-shape. The width of all slots is 1 mm. The models in the column "Eb_Rb" and "Eb_Rs" include all the components. "E" refers to electrodes, "R" to support rings, and suffix "b" means bronze, while "s" means 316LN stainless steel. Using 316L stainless steel for the supporting rings generally does not change the induced magnetic fields compared to using 316LN. Two additional eddy current simulations not shown in the table were also run as baseline cases; the coils by themselves, with no vessel or other components, and the coils plus the 316L stainless steel vessel but no other components.

a function of time during the switching cycle. The same driving current shown in Fig. 6.5a is used in the simulations. The comparisons of the axial magnetic fields at t = 18, 24, 26, 31 are shown in Fig. 6.9.

The explanations of the items in the legend in Fig. 6.9 are listed below:

1. "one_slot_Eb_Rb_RingNotSp": The electrodes are fully split; the materials of the electrodes and supporting rings are bronze; the supporting rings are not split.

2. "one_slot_Eb_Rs_RingNotSp": It has the same configuration as "one_slot_Eb_Rb_RingNotSp", except that the supporting rings are stainless steel.

3. "one_slot_E&R_Eb_Rs": The electrodes and the supporting rings are fully split; the materials of the electrodes and the supporting rings are bronze and stainless steel, respectively.

4. "coil_noVessel": Only the MOT coils are included in the simulation. The magnetic field produced by the coils serves as a reference for the other simulations.

5. "coil_Vessel": The MOT coils and the chamber are included in the simulation. This simulation is for studying the eddy current magnetic field produced by the eddy currents induced in the chamber.

6. "oneBridgedSlot_Eb_Rs_RingNotSp": The electrodes are partially split; the materials of the electrodes and the supporting rings are bronze and stainless steel, respectively; the

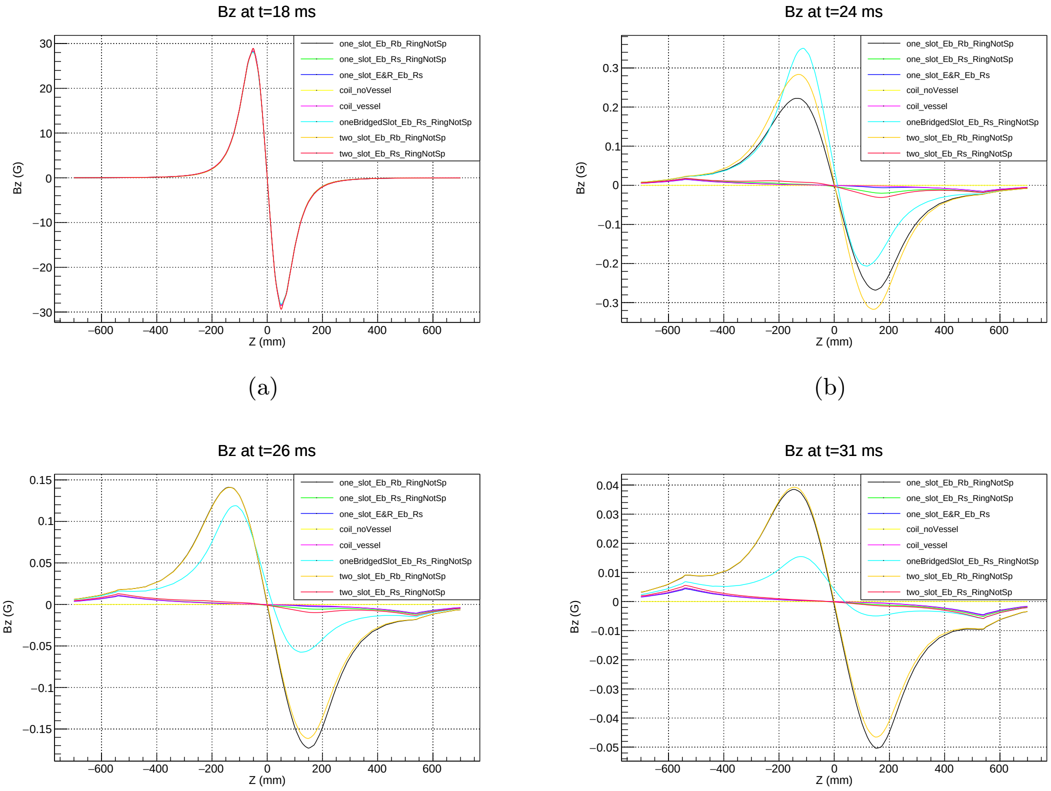

(a) (b)

(c) (d)

Figure 6.9: Comparison of the axial magnetic fields at different time slots. The time slots are labeled in the titles of the figures. The magnetic fields are not symmetric with respect to the center of the MOT because these simulations are based on an old design of the spectrometer, in which the ion and electron spectrometer arms were asymmetric. The labels in the legend are explained following their orders in the legend:

1. "one_slot_Eb_Rb_RingNotSp": The electrodes are fully split; the materials of the electrodes and supporting rings are bronze; the supporting rings are not split;
2. "one_slot_Eb_Rs_RingNotSp": It has the same configuration as "one_slot_Eb_Rb_RingNotSp", except that the supporting rings are stainless steel;
3. "one_slot_E&R_Eb_Rs": The electrodes and the supporting rings are fully split; the materials of the electrodes and the supporting rings are bronze and stainless steel, respectively;
4. "coil_noVessel": Only the MOT coils are included in the simulation. The magnetic field produced by the coils serves as a reference for the other simulations;
5. "coil_Vessel": The MOT coils and the chamber are included in the simulation. This simulation is for studying the eddy current magnetic field produced by the eddy currents induced in the chamber;
6. "oneBridgedSlot_Eb_Rs_RingNotSp": The electrodes are partially split; the materials of the electrodes and the supporting rings are bronze and stainless steel, respectively; the supporting rings are not split;
7. "two_slot_Eb_Rb_RingNotSp": The electrodes are split into two equal halves; the materials of the electrodes and the supporting rings are bronze;
8. "two_slot_Eb_Rs_RingNotSp": The configuration is the same as "two_slot_Eb_Rb" except that the supporting rings are made of stainless steel.

supporting rings are not split.

7. "two_slot_Eb_Rb_RingNotSp": The electrodes are split into two equal halves; the materials of the electrodes and the supporting rings are bronze.

8. "two_slot_Eb_Rs_RingNotSp": The configuration is the same as "two_slot_Eb_Rb" except that the supporting rings are made of stainless steel.

The peak values of the induced magnetic fields are summarized in Table. 6.2

	t=24 ms		t=31 ms	
slot condition	Eb_Rb (G)	Eb_Rs (G)	Eb_Rb (G)	Eb_Rs (G)
one full radius slot on E	0.26	0.02	0.045	0.005
one full radius slot on E & R	NOT Simulated	0.018	NOT Simulated	0.005
two full radius slots on E	0.32	0.031	0.043	0.005
one partial radius slot on E	NOT Simulated	0.35	NOT Simulated	0.015

Table 6.2: The labels in the table have the same meaning as table 6.1. The numbers are the peak values of the induced magnetic fields in Gauss. The number in red is the peak value of the magnetic field generated by the eddy current in the vacuum vessel flange.

By comparing axial magnetic fields of different simulations at different times, we can conclude that:

1. Slotting the electrodes across their full radial width is effective to diminish the eddy current and therefore the induced magnetic field.

2. The comparison between "two_slot_Eb_Rb_RingNotSp" and its counterpart "one_slot_Eb_Rb_RingNotSp", or the ones with stainless steel for the supporting rings, indicates that splitting electrodes with one slot vs. two slots does not make a big difference to the induced magnetic field. Considering the mechanical stability of the spectrometer, it would be better to use the one slot configuration.

3. The eddy current magnetic field of "two_slot_Eb_Rs_RingNotSp" is much smaller compared to the field of "two_slot_Eb_Rb_RingNotSp", suggesting that it would be better to make the supporting rings out of 316LN stainless steel.

4. "one_slot_E&R_Eb_Rs" has the lowest eddy current magnetic field compared to other simulations, with the spectrometer model demonstrating that splitting the supporting rings also reduces the induced magnetic field. However this option requires further study, because it may affect the mechanical stability of the supporting structures.

5. The difference between "coil_noVessel" and "coil_Vessel" indicates that the decay time of the fields induced by the annular flanges of the central chamber is comparable to the data

acquisition time. However, the field is too weak to disturb electron trajectories.

6. The comparison between "oneBridgedSlot_Eb_Rs_RingNotSp" and "one_slot_Eb_Rs_RingNotSp" indicates that partial slot is ineffective in suppressing the eddy currents.

6.3.2 Effectiveness of Titanium Electrodes

The above simulations are for studying the effectiveness of split electrodes in suppressing the eddy current magnetic field. Another way of suppressing the magnetic field is by using a material with a large resistivity for the electrodes. In electrical engineering, the decay time of an eddy current can be expressed as $t = L/R$, where L is the self-inductance determined by the geometry of the electrode [101] and R is the resistance. To achieve a short decay time of the eddy current, titanium with resistivity of $\rho_R = 1.7 \times 10^{-4}\ \Omega \cdot \mathrm{cm}$, which is 14 times larger than bronze, was selected for the small electrodes because of its large resistivity. Bronze is recommended for large electrodes because oxides of copper are conductive, eliminating patch effect [102]. There is not a high priority to use titanium for the large electrodes, given that the large electrodes are far away from the MOT, and the induced eddy currents in the large electrodes don't play a significant role in producing an eddy current magnetic field.

For small electrodes with an outer radius of 120 mm, an inner radius of 66 mm and a thickness of 0.3 mm, the self-inductance of the electrodes can be calculated by treating them as a coil.

$$L = 0.001N^2 \cdot a \cdot P \cdot F = 0.001 \times 1 \times 9.3 \times 0.9978 \times 26.968\mathrm{\mu H} = 0.25\mathrm{\mu H} \tag{6.8}$$

where N is the number of turns of the wires forming the coil, in this case $N = 1$. P is a function of c/2a, F is a function of c/2a and b/c. Values of P and F are tabulated in Ref. [101]. The values not listed in the tables can be linearly interpolated from the tabulated values. The definitions of a, b, c are shown in Fig. 6.8. The decay time of the small titanium electrode is therefore

$$t = \frac{L}{R} = \frac{0.25 \times 10^{-6}}{\rho_R \cdot 2\pi \cdot a/(b \cdot c)}\mathrm{s} = 4.1\ \mathrm{\mu s} \tag{6.9}$$

This is very short compared to the proposed 20 ms switching cycle and so should be very effective in reducing the eddy current effects. The eddy current magnetic fields produced by the electrodes made of different materials were simulated to study the effectiveness of different materials in suppressing eddy currents without splitting the electrodes. The comparisons of the

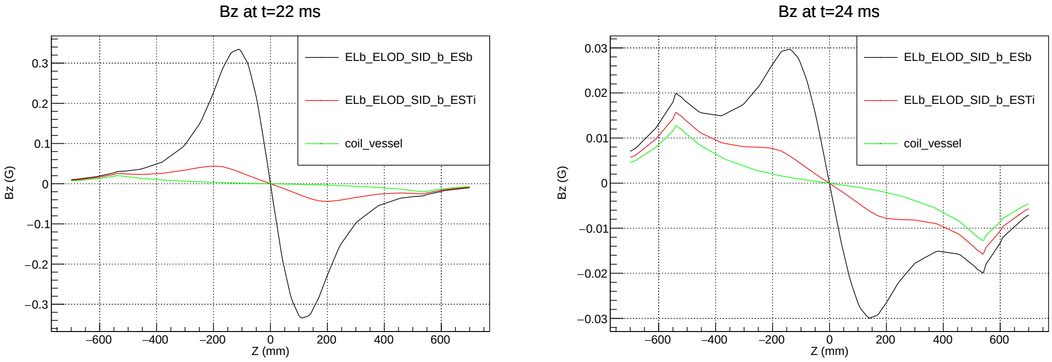

(a) Bz at $t = 22$ ms

(b) Bz at $t = 24$ ms

Figure 6.10: Comparison of Bz of three simulations at $t = 22$ ms and $t = 24$ ms. The eddy current magnetic field generated in the simulation with only coils and a vessel serves as reference. "ELb_ELOD_SID_b_ESb" means that the large electrodes, the large electrode with a small inner diameter, and the small electrodes are made of bronze. "ELb_ELOD_SID_b_ESTi" is the same as "ELb_ELOD_SID_b_ESb" except that the small electrodes are made of titanium. These simulations are based on the latest spectrometer model, in which the ion arm and the electron arm are symmetric. The thicknesses of the small electrodes and large electrodes are 0.3 mm and 0.6 mm, respectively.

eddy current magnetic fields are shown in Fig. 6.10

The comparisons in Fig. 6.10 indicate that as expected, the titanium electrodes have much better performance in suppressing eddy currents than the bronze electrodes. The eddy current magnetic field for the model with the small electrodes made of titanium at $t = 24$ ms is less than 10 mG, which satisfies the requirements of electron momentum resolution.

CHAPTER 7

MAGNETIC SHIELD DESIGN

This chapter introduces the design of a magnetic shield of the spectrometer in the HUNTER experiment, to shield the external magnetic fields from the Earth, building systems, and the electronic devices in the vicinity of the spectrometer. Given the scale of the chamber and the ports distributed at the central chamber along the azimuthal direction, a traditional continuous cylindrical magnetic shield is not possible for HUNTER. An octagonal magnetic shield design consisting of separable flat and bent pieces was adopted, considering the feasibility of manufacturing and assembling the magnetic shield. The achieved highest attenuation factors of the magnetic shield for the external 0.6 G longitudinal and transverse magnetic field are ∼200 and ∼3000, respectively.

In the Phase 1 HUNTER experiment, the expected electron momentum resolution associated with the finite MOT size and the presence of a uniform 8 G magnetic field is ∼0.1 keV based on Geant4 simulations of electron trajectories. To avoid degrading electron momentum resolution, the penetration of the external magnetic fields into the spectrometer interior should be controlled under 30 mG.

7.1 Estimation of Permitted Stray Field Leakage into HUNTER Spectrometers

For an electron produced in a ^{131}Cs decay, initial $p_{\parallel}$ of the electron can be easily reconstructed from TOF based on the formula of accelerated motion. The reconstruction error of $p_{\parallel}$ is dominated by the time resolutions of the x-ray detector and the electron MCP. Initial $p_{\perp}$ reconstruction is complicated due to the combined effect of the electric and magnetic field [70]. The projection of a typical spiraling trajectory of an electron is shown in Fig. 7.1. In this figure, O is the initial position of the electron. r and C are the impact radius and impact position, respectively. $p_{\perp}$ can be reconstructed from the measurements of r, TOF, and the combined fields. Assume the magnetic field only has the longitudinal component B and the uniform electric field is E. The TOF of the electron can be written as

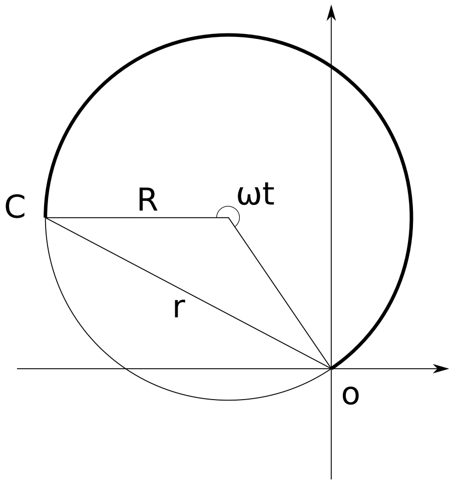

Figure 7.1: (Reproduced from Ref. [70]) Projection of an electron trajectory for the idealized case of uniform magnetic field. Point O is the initial point of electron trajectory and C is the impact position. ωt is the total spiraling angle, where ω is the angular frequency. R is the radius of the spiral.

$$t = \frac{-p_{\parallel} + \sqrt{p_{\parallel}^2 + 2qEm_eL}}{qEc} \tag{7.1}$$

where t is in unit s, $p_{\parallel}$ is in unit eV/c, $q = 1e$, m_e is electron mass in unit eV, E is in unit V/mm, and L is the length of the electron spectrometer in unit mm. c is the speed of light. The total spiraling angle of the electron before impacting the electron MCP is equal to the product of the angular frequency and the TOF, which can be written as

$$\omega t = \eta \frac{qB}{m_e} t \tag{7.2}$$

where $\eta = 8.96 \times 10^{12}$ is used for converting the unit of Bq/m_e to $rad \cdot s^{-1}$, B , q and m_e are in units of Gauss, e and eV/c^2, respectively. The impact radius is

$$r = 2R|\sin(\frac{1}{2}\omega t)| = 2\frac{p_{\perp}c}{\eta qB}|\sin(\frac{1}{2}\omega t)| \tag{7.3}$$

Rearranging Eq. 7.3, the $p_{\perp}$ can be expressed as

$$p_{\perp} = \frac{rqB\eta}{2c|\sin(\frac{1}{2}\omega t)|} \tag{7.4}$$

Given the complicated dependence of $p_{\perp}$ on B and E, it is difficult to estimate the B precision from a required momentum resolution. Geant4 simulations indicate that a stray field less than $\sim$ 30 mG has a negligible influence on the electron momentum resolution. Therefore, a shield design reducing the known external fields in the HUNTER lab to below 30 mG was sought.

7.2 HUNTER Magnetic Shield Design

The 2-D cross-section layout of the spectrometer is shown in Fig. 3.3. The six solenoids outside of the chamber, used to produce the required magnetic field for confining electron trajectories, should be situated inside the shield. The longest solenoid, in purple, is for generating a uniform ∼8 G magnetic field. The rest of the solenoids are for tuning the magnetic field at the MOT center to be uniform. The large gap between the two solenoids in yellow is reserved for the chamber ports, as shown in the end-view of the chamber in Fig. 7.4. Twenty-four ports are distributed along the central chamber with a diameter of 1325 mm azimuthally. The numbers and diameters of the ports in the first quarter of the drawing in the clockwise direction are: one port with a CF flange of 13.25 inches; two ports at the same azimuthal angel with a CF flange of 4.5 inches; one port with a CF flange of 13.25 inches; one wire seal tube with an outer diameter of 16 inches; three ports at the same azimuthal angle with CF flanges of 4.5 inches. The azimuthal angles from the vertical direction to the central axis of the ports are 20, 40, 68.5, 90 degrees, respectively.

To achieve high momentum resolution for electrons, the internal magnetic field must be precisely controlled and be independent of the external magnetic fields. The residual magnetic field induced by the eddy currents is diminished by choosing materials with a large resistivity for the electrodes. To reduce the influence of the external magnetic fields, a two-layer magnetic shield has been designed using COMSOL. The reliability of the simulation results of COMSOL has been proved by comparing the simulation results of simple shield models with the theoretical calculations in Ref. [103, 104, 105].

Given that the main source of the external magnetic field in the HUNTER experiment comes from the Earth, a 0.6 G background magnetic field was used in the COMSOL simulations. The measured background magnetic field in the HUNTER lab is shown in Fig. 7.2 (figures courtesy of the HUNTER collaborators at UCLA, where the experimental apparatus will be set up).

A long term measurement of the background magnetic field shown in Fig. 7.3 indicates that the X and Y components of the magnetic field are ∼230 mG, and the Z component is ∼-50 mG. The magnitude of the magnetic field that is beyond the stray field can be tolerated in HUNTER, which requires a magnetic shield outside of the spectrometer to shield the external fields. The general idea of a magnetic shield design can be found in Ref. [106, 107, 108, 109, 110]. In these references, cylindrical shields are used since the apparatuses to be shielded are either simple or small. Given the large dimension and the complicated structure of the spectrometer chamber, applying a cylindrical shield in the HUNTER experiment is not feasible because of the difficulties

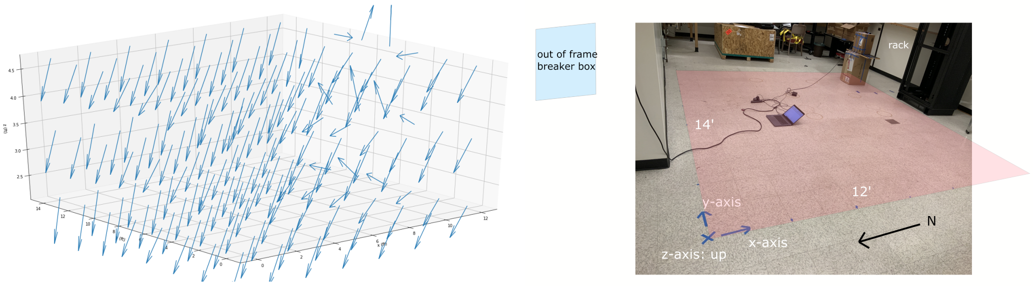

(a)

(b)

Figure 7.2: (a): Results of measuring the 3-D background magnetic field in the laboratory. The disorder of the magnetic field on the right side of the plot is due to highly magnetic objects, like a breaker box and an equipment rack. (b): Illustration of the position at which the spectrometer will be situated.

in the manufacturing and assembling process. To avoid these difficulties, an octagonal shield concept developed in Ref. [111] is adopted in HUNTER, which requires no rolled (circular) profiles, only flat pieces and pieces bent through specific angles.

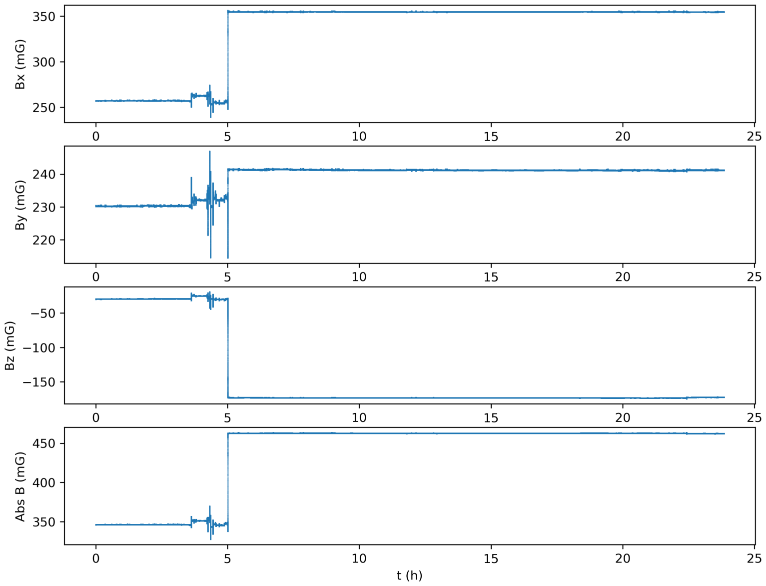

Figure 7.3: Long term measurement of the background magnetic field. The step of the magnetic field measurement at $t = 5$ h is an artifact due to a misplaced ruler close to the magnetometer.

The end-view of the chamber with the cross-section of the magnetic shield is shown in Fig. 7.4. The blue lines in this figure represent the bent components of the shield, with a thickness of 1 mm. The bent components are situated between the ports. Each red line represents two flat sheets with a thickness of 1 mm, which are clamped together and sandwiched between two bent pieces in this concept. End caps with a thickness of 2 mm will be used to close the shield. The distances from the center of the chamber to the flat pieces vary at different angles. The key dimensions of the design are labeled in the figure. Only a quarter of the cross section of the shield is drawn, because of the four-fold rotational symmetry of the chamber, ignoring the asymmetry of the ports in the end flanges of the chamber.

To accommodate the protruding ports of the chamber, rectangular pieces are cut out from the flat and bent components of the shield. However, this provides windows for the penetration of external magnetic fields. To diminish the penetration, rectangular boxes (“sleeves”) are deployed at both the outer and inner layers of the shield. The cross section of the sleeves are shown in green in Fig. 7.4. The heights of the outer and inner sleeves are 500 mm and 250 mm, respectively. The height of the inner sleeves for the end ports is 100 mm. One end of the sleeves is bent at 90 degrees at the base of the sleeves, so that they can be clamped between the bent pieces and the flat pieces of the shield, as shown in the right of Fig.7.4. The rectangular piece cut out from the upper sheet of the flat piece is slightly larger than the lower sheet, for accommodating the base of the sleeve. The right angle transition between the sleeve and its base is believed not to cause a big leakage of the external magnetic fields [112]. This was confirmed by our simulations.

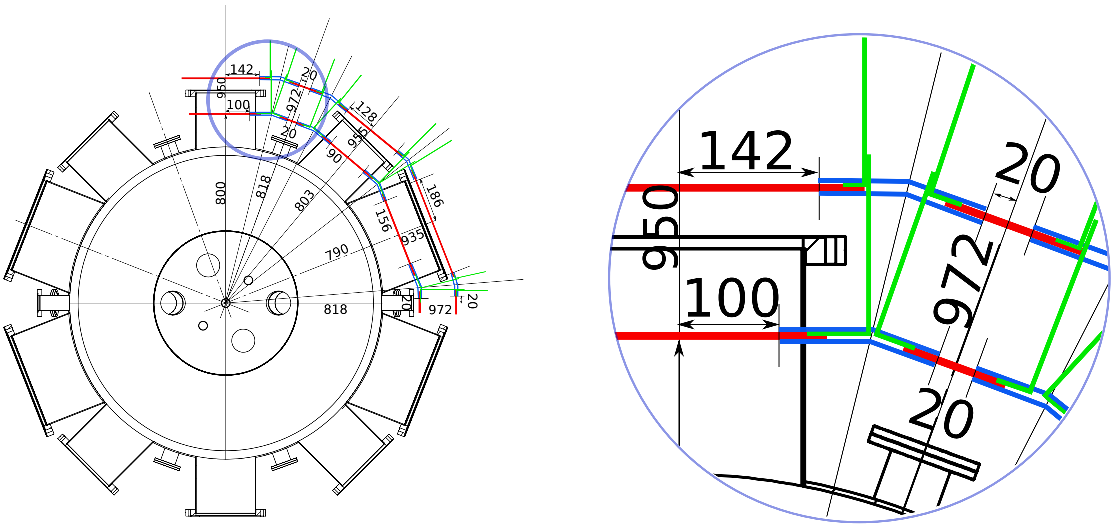

Figure 7.4: Left: The end-view of the chamber with the octagonal magnetic shield designed here. The red and blue lines represent the flat and bent components of the shield. Right: Zoom in of the details in the circle to show how the base of a sleeve is clamped between shield pieces. The unit of size marked in the figure is mm.

The total length of the outer layer of the magnetic shield is 3406 mm. The distances from the center of the chamber to the left and right end of the outer layer are 1516 mm and 1890 mm, respectively. To have a uniform magnetic field on the electron side, the main solenoid on the electron side is longer than that of the ion side. The total length of the inner shield layer is 3106 mm. The distance between the end caps of the inner layer and outer layer is 150 mm.

The shield is composed of two layers, an outer layer of mu-metal and an inner layer of pure iron. The outer layer of the shield mostly screens the (weak) external field. Given the ∼8 G field produced by the solenoids, the inner layer of the shield must provide a return path for the solenoid field without becoming magnetically saturated. Therefore, the outer and inner layer are composed of mu-metal and pure iron respectively, according to their properties of saturation and permeability [113].

To design the shield and study its effectiveness, one quadrant of the magnetic shield model was constructed in COMSOL, as shown in Fig. 7.5a [114]. The vacuum chamber and the spectrometer are not included in this model since these components are made of nonmagnetic materials and should contribute little to the internal magnetic field, considering the static external fields.

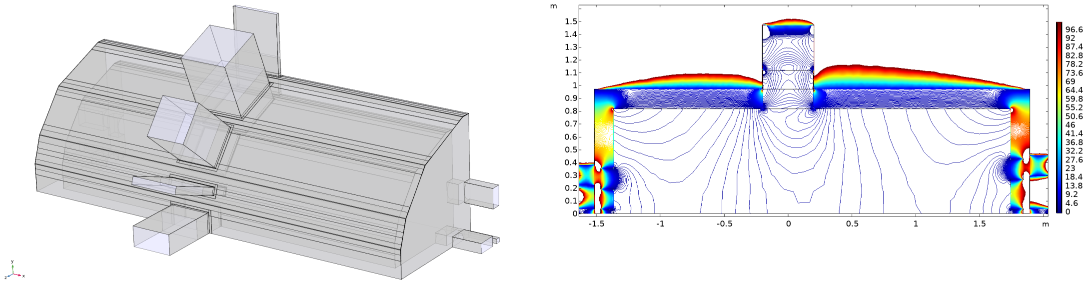

(a) (b)

Figure 7.5: (a): A quadrant of the magnetic shield model with sleeves. In this figure, the X axis is along the long axis of the shield pointing in the right direction, the Y axis is in the vertical direction with the positive direction pointing up. The Z axis is pointing outward perpendicular to the XY plane. (b): Contour lines in the XZ plane of the field inside the shield for a 0.6 G external longitudinal field. The range of the contour lines is from 0 to 30 milligauss with a contour interval of 0.2 milligauss.

To study the internal magnetic field of the shield, simulations with three different shield models were implemented. The configurations of the models are listed below:

1. Outer and inner layer are mu-metal and pure iron, respectively. mu-metal sleeves are employed for both layers.
2. Outer and inner layer are mu-metal and pure iron, respectively. Sleeves are not used in the model.
3. Both outer and inner layers are pure iron. Sleeves are not used in the model.

Simulations with 0.6 G longitudinal and transverse external magnetic field were performed for each model to study the shielding effectivenesses for the external magnetic field in different directions. The transverse external magnetic field is along the Z axis as defined in Fig. 7.5a. The X component (axial component) of the internal magnetic field for the longitudinal and transverse external field are shown in Fig. 7.6

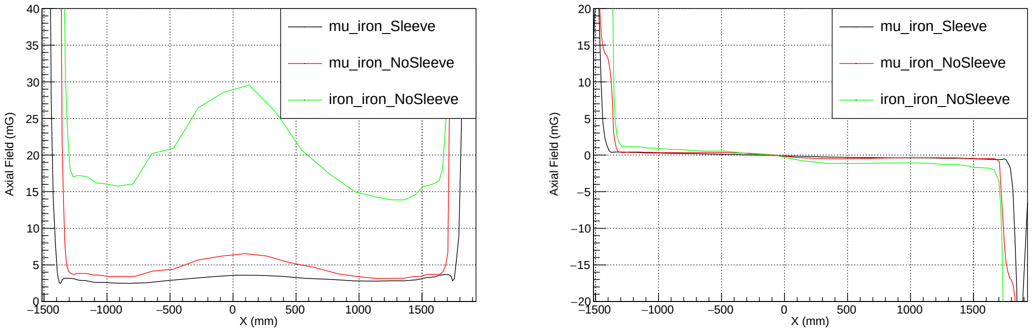

(a) (b)

Figure 7.6: (a): The X component of the magnetic field within the shielded volume along the central axis for the longitudinal external magnetic field of 0.6 G. (b): The X component of the magnetic field within the shielded volume along the central axis for the transverse external magnetic field of 0.6 G.

The highest shielding effectiveness shown in Fig. 7.6a is ∼200 for the shield model with the mu-metal layer, pure iron layer, and sleeves. The internal magnetic field for the shield with mu-metal layer and pure iron layer, but without sleeves, is around 6 mG, which also satisfies the requirements for achieving a high momentum resolution for electrons. The internal magnetic field for the shield, consisting of two pure iron layers, marginally satisfies the requirements.

In the simulation with the transverse external magnetic field, the field lines are absorbed and redirected in the magnetic shield. The leakage of the magnetic field from the walls of the shield form the internal magnetic field as shown in Fig. 7.6b. The opposite sign of the internal magnetic field with respect to the MOT center is due to the redirected propagation directions of the field inside the shield.

7.3 Interaction of Spectrometer with Magnetic Shield

To study the magnetic field produced by the solenoids, simulations with solenoids inside the shield were also implemented. The configuration of the solenoids, provided by Francesco Granato, is shown in Table. 7.1

In Table. 7.1, “D (mm)” is the distance between the MOT center and the near side of a solenoid. “Len (mm)” is the length of a solenoid. “I (A)” and “OD (mm)” are the current and outer diameter of a solenoid, respectively.

The magnetic field produced by the solenoids inside the shield is shown in Fig. 7.7.

The magnetic fields of these three models are generally the same. The field at $Z = 0$ has a small gradient, which is good for the MOT. However, the field along the electron path is not

	D (mm)	I (A)	Len (mm)	Turns	OD (mm)
solenoids on the ion side					
1	207	-4.963	100	100	1351
2	307	-0.217	300	300	1351
3	607	-0.119	503	503	1341
solenoids on the electron side					
1	207	-2.52	100	100	1351
2	307	-0.43	300	300	1351
3	607	-0.685	1000	1000	1341
4	1607	-0.45	30	30	1341

Table 7.1: The parameters of the electron-confining solenoids are shown in the table. Distances are measured from the center of MOT to the near end of solenoids. The solenoids are numbered from the inside near the MOT to the outside.

as uniform as desired. Analysis methods are being developed which can diminish the negative effect of the inhomogeneity of the magnetic field upon the electron momentum reconstruction.

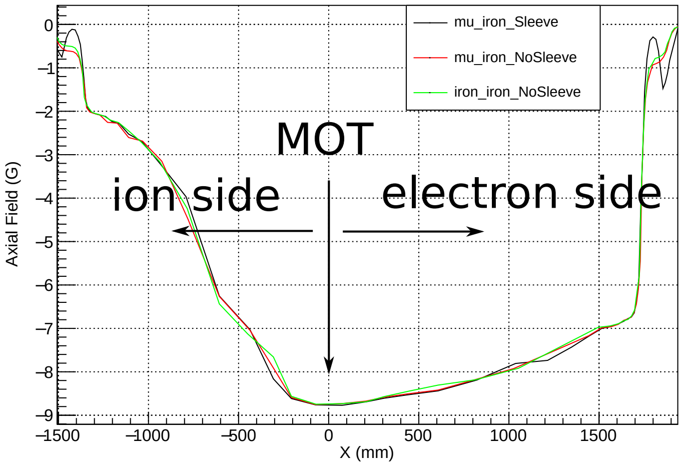

Figure 7.7: X component of the magnetic field produced by the solenoids inside the different models of magnetic shield.

7.4 Shield Performance with Particle Trajectories

In order to simulate the electron trajectories under the total magnetic field from the solenoids and the external background, the field map of the simulation of the shield with sleeves was exported from COMSOL and imported into Geant4 [115], a Monte Carlo package based on C++ for particle physics simulation, to simulate the trajectories of electrons. 10^5 electrons were propagated through the interior volume for the case of the solenoid field only, the solenoid field plus the longitudinal shielding simulation, and the solenoid field plus the transverse shielding simulation. The initial energy of the electrons was randomly selected from the eight standard

Auger energies, 23, 34, 45, 54, 65, 100, 111, 122 eV. The initial positions of the electrons were generated from a three-dimensional Gaussian distribution centered on the MOT position, and with a root mean square sufficient to give a peak density of $2 \times 10^8/\text{mm}^3$ particles. The initial elevation and azimuth of the particles were randomly generated. Fixing the initial random number seed insured that the same particles were propagated in all three cases.

Table. 7.2 classifies the average p_{tot} difference calculated by using the developed analytical methods for the three cases mentioned above according to the electron initial energies. The errors shown in Table. 7.2 in blue color for both the momentum and energy are intrinsic errors because of the MOT size. Comparing the errors in red and black with blue shows that the stray field does not make any noticeable change to the electron momentum and energy resolution.

KE [eV]	$\langle \delta p_{tot} \rangle$ [keV/c]			$\langle \delta E \rangle$ [eV]		
23	0.171	0.171	0.171	1.925	1.929	1.925
34	0.163	0.164	0.164	2.766	2.765	2.766
45	0.146	0.146	0.146	3.389	3.391	3.389
54	0.147	0.148	0.147	3.997	3.996	3.997
65	0.146	0.148	0.146	4.331	4.325	4.331
100	0.115	0.115	0.115	3.476	3.475	3.476
111	0.113	0.114	0.113	3.318	3.317	3.318
122	0.122	0.122	0.122	3.853	3.824	3.853

Table 7.2: Reconstruction results for three different external stray magnetic field cases. Numbers in blue refer to the "no stray field" case; numbers in red refer to the "longitudinal 0.6G" case; numbers in black refer to the "transverse 0.6G" case.

The electron trajectory simulation shows that influence of the residual field is negligible for high precision measurements of electron momentum in the HUNTER experiment. Given that the shielding effectiveness of the magnetic shield design without sleeves is comparable to the one with sleeves, it can also be a candidate of the shield design for HUNTER.

7.5 Magnetic Effects of X-ray Detector Components

In the Phase 1 HUNTER experiment, x-rays from N shell refilling of ^{131}Cs decays will be detected and serve as the start time of TOF measurements. Four x-ray detectors will be employed and situated in four re-entrant flanges. This Section introduces the x-ray detectors and the magnetic shields of the detectors.

In the HUNTER experiment, x-ray detector scintillators will be made up of 50 mm × 50 mm × 1 mm thick YAP tiles, with each tile read out by a SiPM array. The energy resolution of the x-ray detector is around 1 keV, which is marginal to identify x-rays from the M shell and N shell refilling. To achieve a high angular resolution in x-ray momentum reconstruction, the

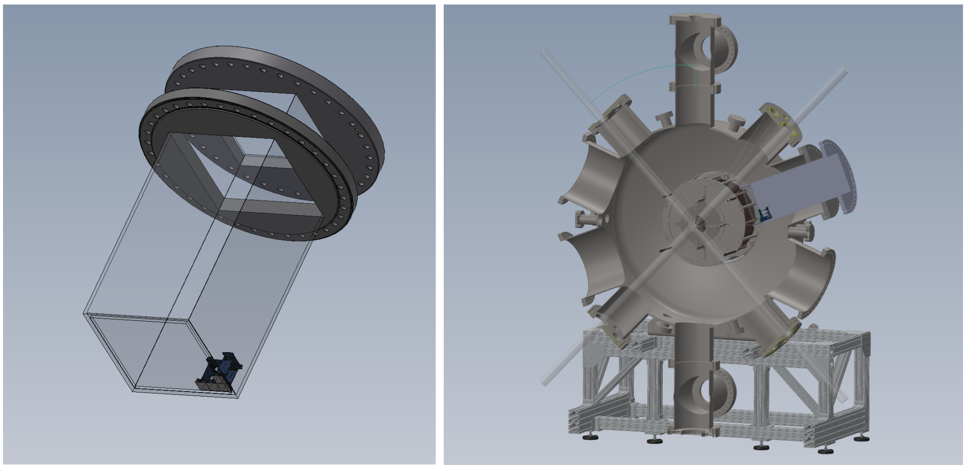

(a) (b)

Figure 7.8: (a): A re-entrant flange with a few SiPM modules. (b): The assembly of a re-entrant flange and the central chamber. The two crossed cylinders passing through the center of the chamber represent the laser beams for trapping Cs atoms. One re-entrant flange is placed in each wire-seal-flanged tube with an outer diameter of 16 inches.

x-ray detectors are suggested to be placed 400 mm radially away from the MOT center in the azimuthal direction. A 5×5 array of YAP tiles will be grouped to form an x-ray detector panel. The solid angle subtended by the x-ray detector panels is around 12% of 4π in the Phase 1 HUNTER experiment.

Given the outgasing issue of the x-ray detectors, they will be placed in four re-entrant flanges with a thin aluminum window of 125 µm to isolate them from the UHV surrounding that is inside the chamber, as shown in Fig. 7.8a.

One re-entrant flange is placed in the wire seal nominal tube with outer diameter of 16 inches as shown in Fig. 7.8a and the other three are symmetric to this one with respect to the vertical and horizontal planes. The heights of the re-entrant flange are designed to not block the two intersecting laser beams as shown in Fig. 7.8b.

In a test phase of HUNTER, photomultiplier tubes (PMT) R580 from Hamamatsu will replace SiPM for scintillator light collection and read out in the Phase 1 HUNTER experiment. Given the 8 G magnetic field produced by the solenoids, the PMTs require magnetic shields of their own to maintain their gain and efficiency. The effect of the magnetic field on the output of PMT according to the manufacturer is shown in Fig. 7.9 [116].

The effects of magnetic fields to PMT R580 is depicted by the curve labeled "38 mm dia. HEAD-ON TYPE" in Fig. 7.9, where 38 mm is the diameter of the PMT of R580. According to Fig. 7.9, the output of the PMT signal also depends on the direction of magnetic fields. Give the 8 G magnetic field in the chamber, a cylindrical mu-metal magnetic shield case will be applied

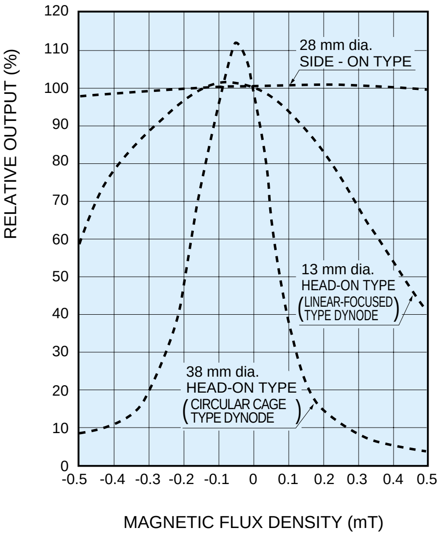

Figure 7.9: Typical effect of magnetic fields perpendicular to PMT from Ref. [116]

to reduce the influence of the magnetic field on the PMT. 16 PMT shield cases form a 4 × 4 array as shown in Fig. 7.10.

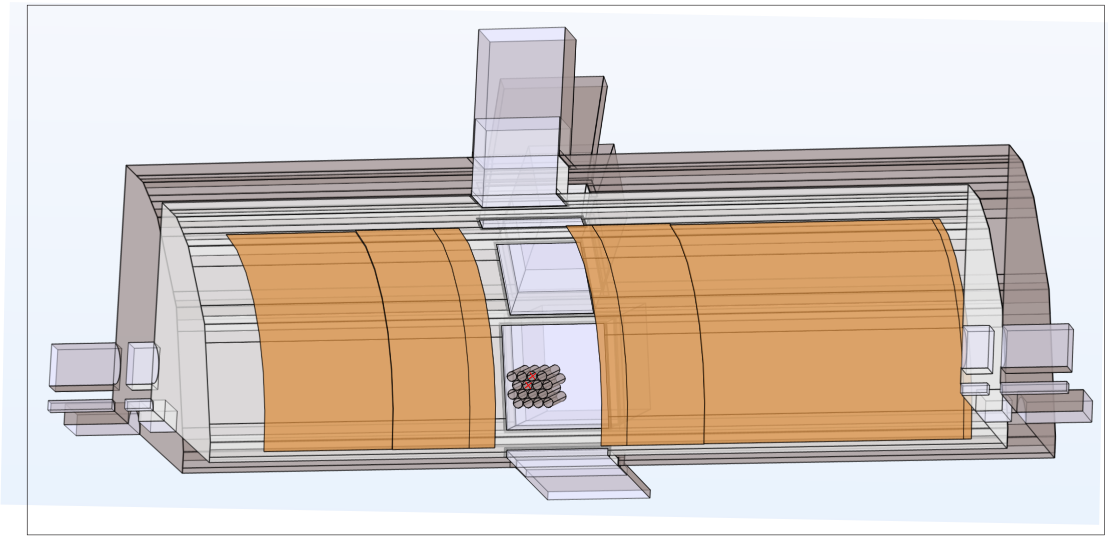

Figure 7.10: Configuration of PMT magnetic shields for simulations. The PMT shield cases in the magnetic shield model are oriented toward the x-ray port. 16 PMT shield cases form a 4 × 4 array as shown in the figure.

The PMT shield array is oriented toward the x-ray ports, with a distance of 400 mm between the MOT center and the near-end of the PMT shields. Each PMT shield case in the array has a thickness of 1 mm, while the radius and the length are 19 mm and 200 mm, respectively. The magnetic fields along the axial direction of the two shield cases marked with a red cross in Fig. 7.10 were extracted from the COMSOL simulation as shown in Fig. 7.11.

The magnetic field at the near-end of the PMT shield case is around 1 G, and then decreases to 10 mG by 40 mm inside the PMT shield. Note that the peak of the relative output shown in Fig. 7.9 for PMT R580 is not centered at zero. The 1 G magnetic field indicated in Fig. 7.11 at the face of the PMT can be ignored if the right direction of the external magnetic field is chosen since it only degrades the relative output by 12% according to Fig. 7.9. Otherwise, light guides should be applied to connect the scintillator and the PMT, allowing the shield to extend beyond the end of the PMT and reducing the field effect further.

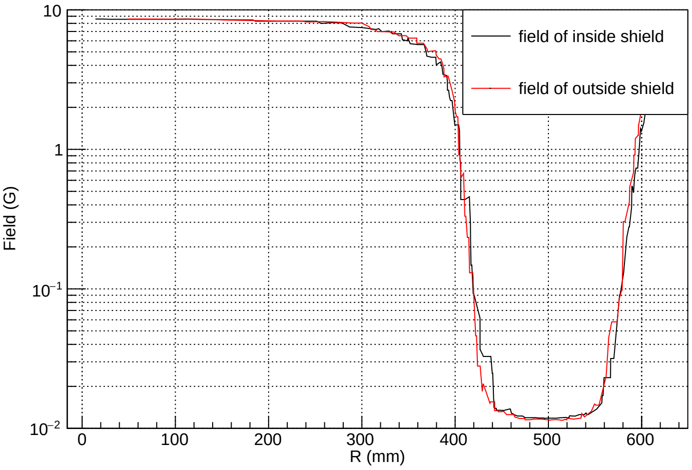

Figure 7.11: Simulated magnetic fields along the axis of the two PMT shields in Fig. 7.10, marked with red cross. “inside shield” in the legend means the PMT shield at the center of the shield array. “outside shield” means the PMT shield on the edge of the shield array.

CHAPTER 8

BACKGROUNDS IN HUNTER

The background study is one of the most important parts of particle physics research, as it helps to understand the feasibility of an experiment. In HUNTER, various backgrounds were identified, and the mass-squared spectrum including different backgrounds were plotted. The background study indicates that the number of background events at a mass region greater than 20 keV is low enough to achieve high-confidence sensitivity in HUNTER.

8.1 Random Coincidence Background

In the HUNTER experiment, if an x-ray signal with an energy of 34.43 keV is followed by one or two electron signals and an ion signal that is not from the same ^{131}Cs decay as the x-ray, and the TOF and IR of the electrons and the ion are in the expected ranges, then the signals of these three or four particles form a random coincidence background event (RCBE). To study the spectrum of RCBE and find a way to rule out these events, a simulation workup of RCBE was performed.

In an EC decay of a ^{131}Cs at rest, energy-momentum conservation gives the reconstruction formula shown in Eq. 2.5 for the neutrino mass-squared, assuming a three particle final state (nucleus with momentum $\mathbf{P_{Xe^+}}$, one Auger electron with momentum $\mathbf{P_e}$, one x-ray with momentum $\mathbf{P}_\gamma$). Define the first term on the right side of the equation as $\tilde{Q}$:

$$\tilde{Q} = m_{Cs} - m_{Xe^+} - m_e - E_e - E_{Xe^+} - E_\gamma \tag{8.1}$$

The second term in the last line of the equation is equal to the neutrino momentum. Define it as:

$$-\mathbf{P}_\nu = \mathbf{P_e} + \mathbf{P_{Xe^+}} + \mathbf{P}_\gamma \tag{8.2}$$

The neutrino mass reconstruction formula can be written as Eq. 8.3

$$\mathbf{P}_\nu{}^2 = \tilde{Q}^2 - m_\nu^2 \tag{8.3}$$

In Eq. 8.1, the kinetic energy of the Xenon ion is around 0.4 eV. The number of Auger electron(s) in ^{131}Cs decays we are interested in can either be one or two, and the difference of the total kinetic energy of Auger electrons in these two cases is less than 20 eV. This difference is negligible compared to the mass term in $\tilde{Q}$. Given the mass of the Xenon ion plus the electrons is a constant, without considering the binding energies of the electrons in the ion, $\tilde{Q}$ is also a constant. This is proved by a Monte Carlo calculation of the kinematics of ^{131}Cs decays.

In the Monte Carlo calculation, momenta of a Xe^{+} ion, Auger electron(s), and an x-ray were generated to satisfy energy-momentum conservation for a ^{131}Cs decay at rest were exported to SIMION. These and their trajectories through the spectrometer were simulated. The TOF, IR, and azimuthal angles of the decay products when striking the corresponding MCPs were recorded. The initial momentum of each secondary particle except the neutrino was then reconstructed from the TOF, IR, and angular information. The distribution of the reconstructed events computed from the energy-momentum conservation in the neutrino mass-squared vs. neutrino momentum plane is shown in Fig. 8.1. The events are seen to be located at the predicted line given by Eq. 8.3.

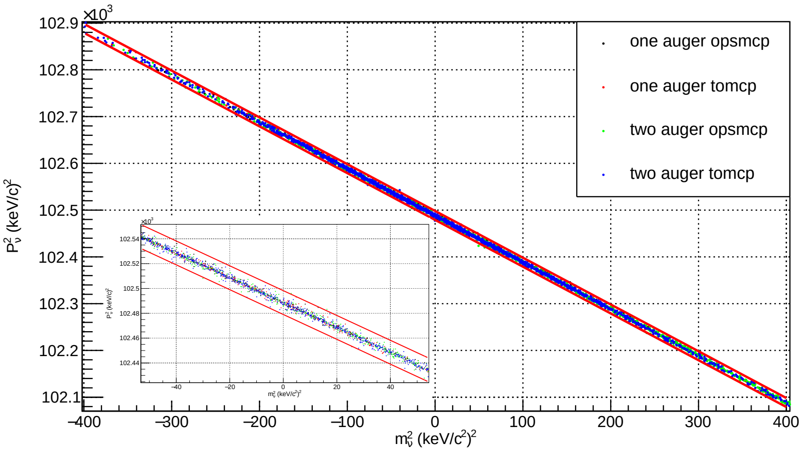

Figure 8.1: Distribution of the reconstructed decay events in m_ν^2 vs. p_ν^2. Considering the standard deviation of the mass-squared spectrum of the neutrino, the X axis range is set to [-400, 400] (keV/c^2)^2. The black (green) dots are the events with one (two) Auger(s), and the ions are emitted from the hemisphere of the MOT opposite the ion MCP. The red (blue) dots are for the events with one (two) Auger(s) and the ions are emitted from the hemisphere of the MOT facing the ion MCP. The details of the events' distribution are shown in the inset. The functions of the pair of red lines are $y = (\tilde{Q}^2 \pm 9.6) - m_\nu^2$

A true coincidence reconstructed decay event must lie within the narrow belt in Fig. 8.1 defined by two lines parallel to Eq. 8.3 representing the reconstruction accuracy. This requirement can be applied to rule out the RCBE.

$$f1 = (\tilde{Q}^2 - 9.6) - m_\nu^2 \tag{8.4a}$$

$$f2 = (\tilde{Q}^2 + 9.6) - m_\nu^2 \tag{8.4b}$$

$\tilde{Q} = 320.1\ \text{keV}/c^2$ is obtained from the kinematics calculation. A band of width $\pm 9.6\ \text{keV}^2$ in Eq. 8.4 was selected to include more than 90% of the reconstructed events in the region between these two parallel lines. It can be named "$\tilde{Q}$ cut" since the $\tilde{Q}$ value is used in the data selection.

8.1.1 Random Background Simulation

To study the characteristics of RCBE, the impact position of the x-ray on the x-ray detectors, the TOF, and the impact positions of ions and electrons were randomly picked from the corresponding ranges according to the SIMION simulation. The details are listed below:

1. x-ray event: In the Phase 1 HUNTER experiment, only x-rays with energy of 34.43 keV will be considered. To simulate the x-ray of a RCBE, the polar angle and the azimuth angle of the x-ray were randomly picked from the corresponding ranges determined by the dimensions and the positions of the x-ray detectors. The ranges of the azimuthal angle θ are $[52.26, 86.96]$ degrees and $[93.04, 127.74]$ degrees, and the polar angle ϕ are $[69.33, 110.67]$ degrees and $[249.33, 290.67]$ degrees, by convention in spherical coordinates, θ and ϕ are the polar angle and azimuthal angle, respectively.

2. Auger event: There are three recorded values associated with an electron event: TOF, IR and azimuthal angle. For the electron of a RCBE, TOF should be in the ranges $[0.094, 0.12]$ µs and $[0.13, 0.16]$ µs, which are the typical TOF ranges for electrons with all the possible initial momenta accepted by the spectrometer. The impact radius of the electron was selected by randomly picking a value from $[3^2, 60^2]$ mm, and then taking square root of the picked value in order to uniformly populate the MCP plane. The lower limit begins at 3 mm because the electron events with impact radius less than 3 mm have a large reconstruction error, and will thus be discarded. The azimuth angle of the electron was randomly picked from $[0, 2\pi]$. The electron number in a RCBE was randomly selected to be either 1 or 2.

3. Ion event: The TOF, IR, and azimuthal angle of an ion were also randomly picked from the

corresponding ranges according to the SIMION simulation results. The TOF ranges for singly-charged (doubly-charged) ions are $[91.5, 93.0]$ µs and $[96.0, 97.8]$ µs ($[65.5, 66.9]$ µs and $(66.9, 68.3]$ µs) depending on the emission polar angle of the ion. The impact radius of the ion was selected in the same way as electrons. The azimuthal angle range of ions is $[0, 2\pi]$. The charge of the ion is consistent with the number of electrons for charge conservation.

With the randomly picked values of x-ray, electrons and ion, the "neutrino mass" and "$\tilde{Q}$" of RCBE can be reconstructed. The distribution of reconstructed $\tilde{Q}$ for RCBE is shown in Fig. 8.2. All RCBE with reconstructed $\tilde{Q}$ outside the range of $\sqrt{\tilde{Q}^2 \pm 9.6}$ can be distinguished from physical ^{131}Cs decay events. The spectrum of $\tilde{Q}$ of these RCBE is shown between the parallel red lines in Fig. 8.2

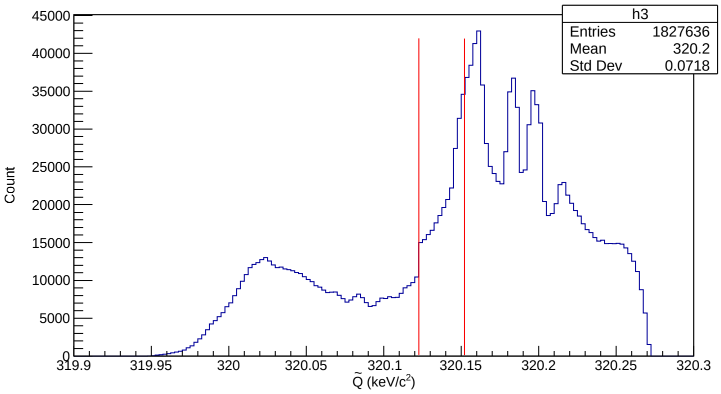

Figure 8.2: (a): The spectrum of $\tilde{Q}$ of simulated random background events without applying the $\tilde{Q}$ cut. The $\tilde{Q}$ cut are represented by the parallel red lines. This shows the effectiveness of the $\tilde{Q}$ cut in suppressing random coincidence background to be 14%.

More than 80% of the RCBE can be excluded by applying the $\tilde{Q}$ cut. The inset in Fig. 8.3 shows the details of the distribution of the RCBE.

Fig. 8.4 is the same scatter plot as Fig. 8.3, but each item in the legend of Fig. 8.3 is plotted in a separate sub-plot.

The spectrum of the RCBEs passing through the $\tilde{Q}$ cut is shown in Fig. 8.5.

8.2 Other Physics Backgrounds

The dominant background in HUNTER is the scattering of the outgoing ^{131}Xe^{+} ions from the MOT. The Monte Carlo calculation of the scattering background of the outgoing ^{131}Xe^{+} colliding with the ^{131}Cs atoms [117, 118] on the path of exiting the MOT was done by Francesco Granato.

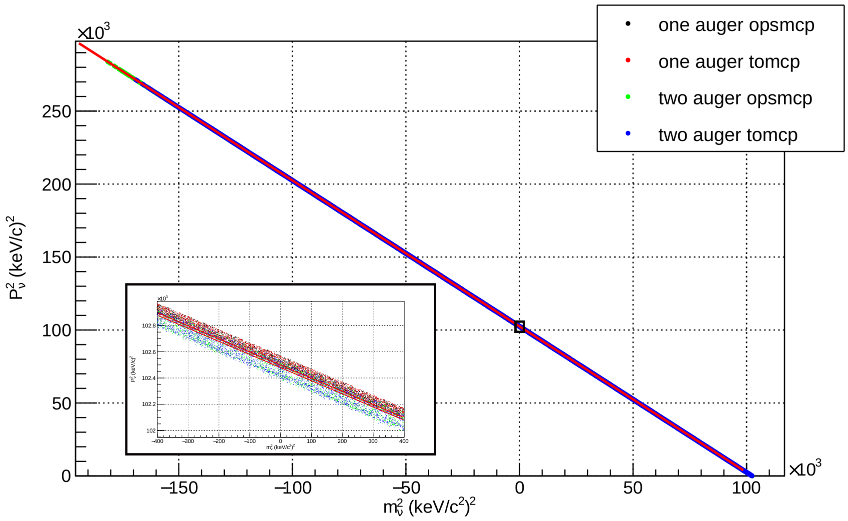

Figure 8.3: Scatter plot of the random coincidence background events. The black (green) dots are the random coincidence background events with one (two) Auger(s), and the ions are emitted from the hemisphere of the MOT opposite the ion MCP. The red (blue) dots are for the random coincidence background events with one (two) Auger(s) and the ions are emitted from the hemisphere of the MOT facing the ion MCP.

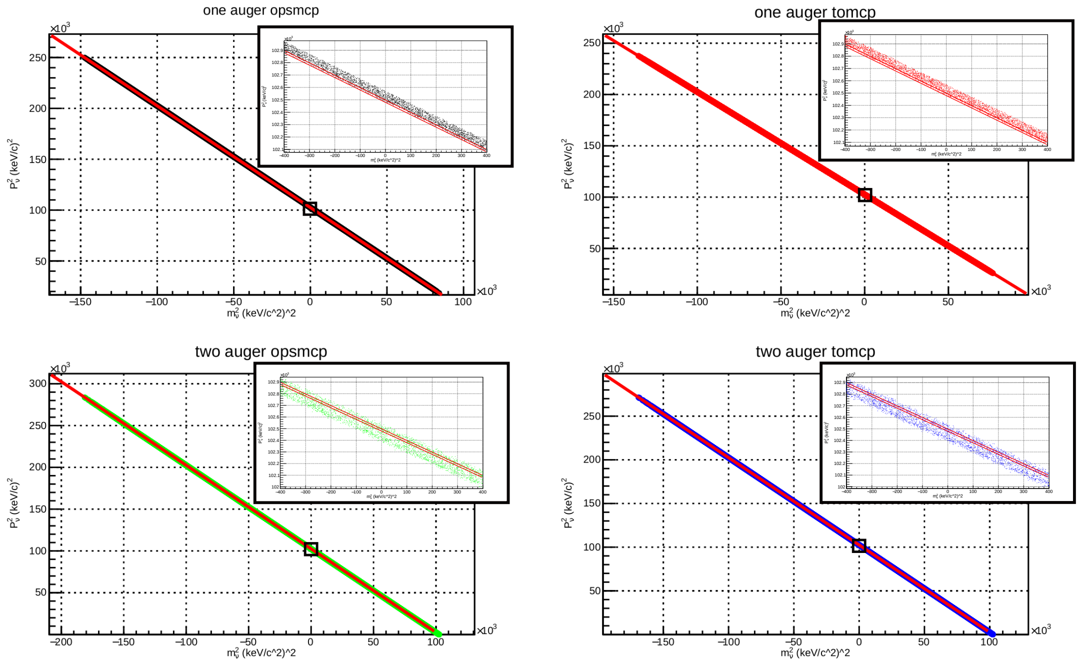

Figure 8.4: The scatter plot of triple coincidence background events for different cases. Each sub-plot is associated with an item in the legend of Fig. 8.3. The small window in each sub-plot is a zoom in of the plot around $m_\nu^2 = 0$.

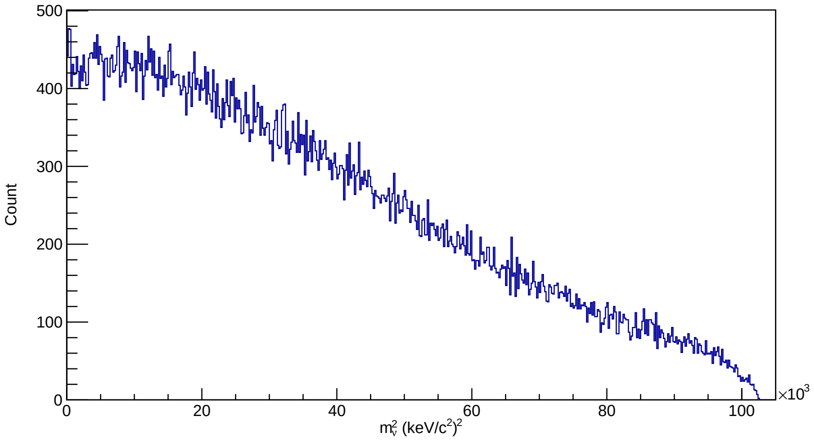

Figure 8.5: Mass-squared spectrum of the RCBE accepted by the $\tilde{Q}$ cut. The smooth distribution cannot easily give a false sterile neutrino mass peak. In this simulation, 2×10^6 events were produced. 1.8×10^6 events passed through two preliminary momentum cuts [200, 400] keV and [5, 30] keV for ions and electrons, respectively. 2.6×10^5 events from the preliminary selection passed through the $\tilde{Q}$ cut, and formed the mass-squared spectrum.

The calculation indicates that the scattering background is mainly contributed by the forward-scattered ions, which form a background spectrum with a resolution lower than the zero-mass neutrino spectrum, as shown in green in Fig. 8.6. The scattering background in the upgraded HUNTER experiment can be suppressed by using MOT with a larger radius, which will decrease the probability of the $^{131}\mathrm{Xe}^{+}$ being scattered on its way out of the atom cloud.

The second major background comes from the radiative K-capture [119, 120, 121, 122], which contributes a smooth background smearing over the full mass range. 99.99% of the radiative K-capture background events can be ruled out by the flight time windows mentioned above. This leads to a background with events of that are a tenth as probable as the ion scattering background.

Other possible backgrounds in HUNTER are studied in Ref. [63]. They are briefly listed below [123]

1. Auger electrons produced by the interaction between x-rays from $^{131}\mathrm{Cs}$ decays and the surfaces of the spectrometer components.
2. Ionization of the residual gas by Auger electrons on the flight path to the electron MCP.
3. Emission of a second photon instead of an Auger electron.
4. Background cosmic ray muons.
5. The decay products from the component materials of the chamber and spectrometer.

According to the study of the backgrounds, a HUNTER background spectrum, including random coincidences background and ion scattering background, is simulated and shown in Fig. 8.6. The zoomed Y-axis in this plot cuts away the vast majority of the normal $m_\nu^2 = 0$ events. The background in a log scale is shown in the inset of Fig. 8.6. A Gaussian distribution, including 40 events centered at $m_\nu^2 = (60\ \mathrm{keV/c^2})^2$ with standard deviation of 329 $(\mathrm{keV/c^2})^2$ equal to the normal $m_\nu^2 = 0$ peak, is added to the mass-squared spectrum to give a highly statistically significant sterile neutrino peak with $\sin^2\theta = 2 \times 10^{-4}$.

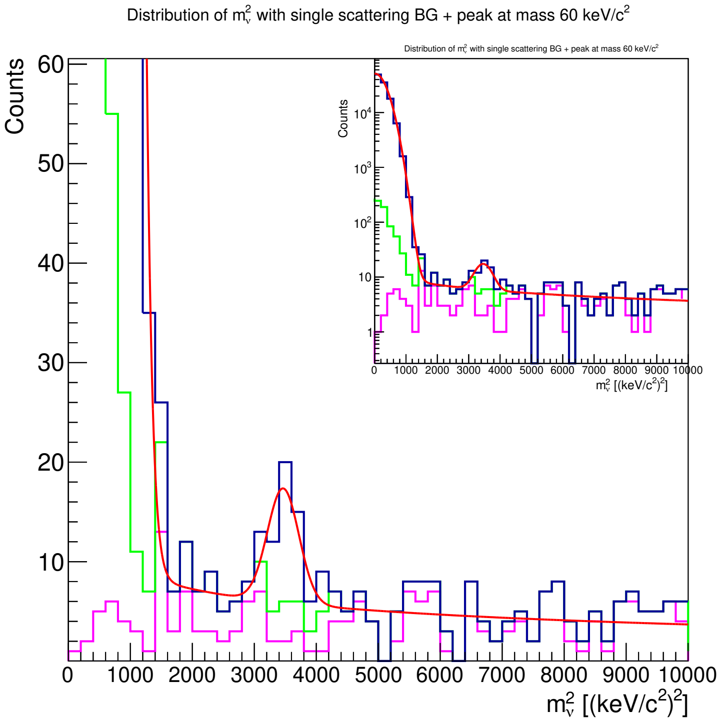

Figure 8.6: Simulated "discovery spectrum" with 40 sterile neutrino events giving a 5σ peak at $m_\nu^2 = (60\ \mathrm{keV/c^2})^2$ using the current reconstruction width 329 $(\mathrm{keV/c^2})^2$. This corresponds to a mixing of sterile neutrinos with active neutrinos given by $\sin^2\theta = 2 \times 10^{-4}$ based on the current estimation of one year background events (2.1×10^5 events) as shown in Table. 9.1. The curves are: magenta- random coincidence background; green- random plus ion-atom scattering; dark blue- backgrounds plus zero-mass and $(60\ \mathrm{keV/c^2})^2$ peak.

CHAPTER 9

SUMMARY

The HUNTER experiment, a laboratory search for sterile neutrinos based on the EC of ^{131}Cs, has been carefully studied during the past five years. The electric and magnetic fields for guiding charged decay products of ^{131}Cs were optimized to achieve the required reconstruction resolution of initial momentum. Various systematic errors of the HUNTER experiment were studied and their influences on the ion resolution were simulated. The simulation results show that the asymmetric components of the spectrometer and the shift of the MOT center can significantly degrade the ion resolution. The eddy currents induced by cycling the MOT magnetic field were simulated in COMSOL to select the materials of the spectrometer components to suppress the eddy current magnetic field. The eddy current magnetic field for the simulation using titanium electrodes 4 ms after the assumed step-functions switch-off of the MOT coils is less than 10 mG, which satisfies the requirements of HUNTER. An octagonal magnetic shield structure was adopted to design the spectrometer magnetic shield for HUNTER to prevent the external stray fields from disturbing the electron trajectories. The achieved internal magnetic field with the two-layer magnetic shield with sleeves is 3 mG, which gives a shielding effectiveness of $\sim$200. According to these simulations and studies, the expected detection efficiencies of the different decay products for the first phase HUNTER experiment are listed in Table. 9.1 in the first column.

The first 4 lines in Table. 9.1 show the decay channel of ^{131}Cs considered in different phases of HUNTER. The lines under the section "Decays" show the trigger efficiency of the x-rays. The estimation of the overall detection efficiency of ions and electrons in the Phase 1 HUNTER experiment is 4.9%, which results in 2.1×10^5 events per year, by multiplying the trapped atom population and x-ray trigger efficiency.

HUNTER also has a clear upgrade path for the future experiment with a higher sensitivity and lower sterile neutrino mass limit as described in the following two columns after the column for Phase 1 HUNTER experiment.

In the upgraded HUNTER experiment, we are expecting to increase the number of laser trapped atoms from 10^8 to 4×10^9 and 3×10^{11} for Phase 2 and Phase 3, respectively. This will

Sensitivity table for Cs131 K-capture

	Phase 1	Phase 2	Phase 3
Capture shells	K	K	K+L
X-rays used	N	N	M,N
Augers initial vacancy	N2,N3	N2,N3	M,N
Augers per trigger	40% 1e, 60% 2e	40% 1e, 60% 2e	1, 2 or 3
Decays			
Atoms in MOT	1×10^8	4×10^9	3×10^{11}
Source radioactivity (mCi)	10	100	1000
MOT lifetime (s)	30	30	300
Total decays per year per atom $= 0.7 \times 365/9.7$	26	26	26
Fraction of decays giving specified N or M vacancies	0.025	0.025	0.2
X-ray detection $\mathrm{d}\Omega/4\pi$	0.12	0.36	0.6
Trigger X-rays/year/atom	0.078	0.234	3.12
Rejected triggers with shake-off electron	0.45	0.45	0.45
Triggered events without shake-offs/y/atom	0.043	0.13	1.7
Ion efficiencies			
One or two hemisphere collection	2	2	2
On-axis MCP diameter (mm)	120	150	250
Ion capture solid angle fraction	1	1	1
Ion detection efficiency	0.55	0.55	0.6
Total ion detection efficiency	0.55	0.55	0.6
Electron efficiencies (60% 2 Augers + 40% 1 Auger)			
On-axis MCP diameter (mm)	120	150	250
(T) data capture duty cycle	0.5	0.5	0.5
(A) electron capture efficiency for single Auger (40%)	0.25	0.35	0.6
(B) cut efficiency for single Auger	0.61	0.7	0.8
(A') electron capture efficiency for double Augers (60%)	0.93	1	1
(B') cut efficiency for double Auger	0.50	0.6	0.8
(C) electron detection efficiency (MCP at 400V)	0.95	0.95	0.95
$(D = A \times B \times C \times 0.4)$ overall efficiency for single Auger (40%)	0.058	0.093	0.18
$(D' = (A' \times B' \times C)^2 \times 0.6)$ overall efficiency for double Augers (60%)	0.12	0.21	0.37
$(E = T \times (D + D'))$ overall electron efficiency	0.089	0.15	0.28
Overall efficiency			
Overall completed event efficiency (product of red totals)	0.049	0.083	0.17
Processed events per year			
Net events/y/source atom	0.0021	0.011	0.29
Completed events per 360 days active running	2.1×10^5	4.3×10^7	8.7×10^{10}

Table 9.1: Table of factors to determine the overall collection efficiency of HUNTER using full kinematic reconstruction. Phase 1 is funded and being built at this time. The remaining Phases are illustrative of possible upgrades to increase the efficiency and extend the coverage to lower sterile neutrino masses.

result in more decay events in the same running time of the experiment. The overall detection efficiency will be improved by using MCP detectors with larger diameter and by developing a more efficient reconstruction algorithm for electrons. The diameter of MCP detectors will be increased from 120 mm to 150 mm and 250 mm for Phase 2 and Phase 3 respectively. A larger MCP diameter can also improve the momentum resolution for charged particles. The expected sensitivities for Phase 2 and Phase 3 HUNTER experiments are shown in Fig. 2.2.

BIBLIOGRAPHY

[1] C. L. Cowan, F. Reines, F. B. Harrison, *et al.*, Science **124**, 103 (1956).

[2] S. Bilenky and J. Hošek, Physics Reports **90**, 73 (1982).

[3] "Dirac equation," in *Elementary Particle Physics*, Chap. 4, pp. 59–88, https://onlinelibrary.wiley.com/doi/pdf/10.1002/9783527630097 .

[4] M. Tanabashi, K. Hagiwara, K. Hikasa, *et al.* (Particle Data Group), Phys. Rev. D **98**, 030001 (2018).

[5] T. D. Lee and C. N. Yang, Phys. Rev. **104**, 254 (1956).

[6] C. S. Wu, E. Ambler, R. W. Hayward, *et al.*, Phys. Rev. **105**, 1413 (1957).

[7] W. Greiner and B. M?ller, *Gauge Theory of Weak Interactions* (Springer-Verlag Berlin Heidelberg, 2009).

[8] "Weak interaction," in *Elementary Particle Physics*, Chap. 15, pp. 553–615, https://onlinelibrary.wiley.com/doi/pdf/10.1002/9783527630097.ch15 .

[9] S. M. Bilenky and J. Hosek, Phys. Rept. **90**, 73 (1982).

[10] F. Halzen and A. Martin, *QUARK & LEPTONS: AN INTRODUCTORY COURSE IN MODERN PARTICLE PHYSICS* (Wiley India Pvt. Limited, 2008).

[11] D. J. Griffiths, *Introduction to elementary particles; 2nd rev. version*, Physics textbook (Wiley, New York, NY, 2008).

[12] S. Fukuda, Y. Fukuda, M. Ishitsuka, *et al.* (Super-Kamiokande Collaboration), Phys. Rev. Lett. **86**, 5651 (2001).

[13] S. N. Ahmed, A. E. Anthony, E. W. Beier, *et al.* (SNO Collaboration), Phys. Rev. Lett. **92**, 181301 (2004).

[14] F. Kaether, W. Hampel, G. Heusser, *et al.*, Physics Letters B **685**, 47 (2010).

[15] F. P. An, J. Z. Bai, A. B. Balantekin, *et al.*, Phys. Rev. Lett. **108**, 171803 (2012).

[16] P. Adamson, I. Anghel, C. Backhouse, *et al.* (MINOS Collaboration), Phys. Rev. Lett. **110**, 251801 (2013).

[17] K. Abe, J. Adam, H. Aihara, *et al.* (T2K Collaboration), Phys. Rev. Lett. **112**, 181801 (2014).

[18] T. Kajita, Nuclear Physics B - Proceedings Supplements **77**, 123 (1999).

[19] Y. Fukuda, T. Hayakawa, E. Ichihara, *et al.* (Super-Kamiokande Collaboration), Phys. Rev. Lett. **81**, 1562 (1998).

[20] A. Bettini, *Introduction to elementary particle physics; 1st ed.* (Cambridge Univ. Press, Cambridge, 2008).

[21] R. N. Mohapatra, S. Antusch, K. S. Babu, *et al.*, Reports on Progress in Physics **70**, 1757 (2007).

[22] R. Adhikari, M. Agostini, N. A. Ky, *et al.*, Journal of Cosmology and Astroparticle Physics **2017**, 025 (2017).

[23] C. Benso, V. Brdar, M. Lindner, *et al.*, Phys. Rev. D **100**, 115035 (2019).

[24] K. N. Abazajian, Physics Reports **711-712**, 1 (2017), sterile neutrinos in cosmology.

[25] A. de Gouvea, K. Pitts, K. Scholberg, *et al.*, *Neutrinos*, Tech. Rep. arXiv:1310.4340 (2013) comments: Report of the Community Summer Study 2013 (Snowmass) Intensity Frontier Neutrino Working Group.

[26] T. Asaka and M. Shaposhnikov, Physics Letters B **620**, 17 (2005).

[27] M. Thomson, *Modern particle physics* (Cambridge University Press, New York, 2013).

[28] P. Hernandez, CERN Yellow Reports **5**, 85 (2016).

[29] J. A. Dror, *Neutrino Lecture Notes* (2014).

[30] H. R. Reza Zadeh, *Sterile Neutrinos and Cosmology*, Master's thesis, Uppsala University, High Energy Physics (2017).

[31] S. Dawson, "Introduction to electroweak symmetry breaking," (1999), arXiv:hep-ph/9901280 [hep-ph] .

[32] J. L. Feng, Annual Review of Astronomy and Astrophysics **48**, 495 (2010), https://doi.org/10.1146/annurev-astro-082708-101659 .

[33] Q. Yue, K. Kang, J. Li, *et al.*, Journal of Physics: Conference Series **718**, 042066 (2016).

[34] P. Agnes, I. F. M. Albuquerque, T. Alexander, *et al.* (DarkSide Collaboration), Phys. Rev. Lett. **121**, 081307 (2018).

[35] D. S. Akerib, C. W. Akerlof, S. K. Alsum, *et al.* (LUX-ZEPLIN Collaboration), Phys. Rev. D **101**, 052002 (2020).

[36] J. N. Bahcall and R. Davis, Science **191**, 264 (1976).

[37] B. Pontecorvo, Sov. Phys. JETP **26**, 984 (1968).

[38] G. J. Feldman, J. Hartnell, and T. Kobayashi, Adv. High Energy Phys. **2013**, 475749 (2013), arXiv:1210.1778 [hep-ex] .

[39] F. P. An, A. B. Balantekin, H. R. Band, *et al.* (Daya Bay Collaboration), Phys. Rev. D **95**, 072006 (2017).

[40] M. Drewes *et al.*, JCAP **1701**, 025 (2017), arXiv:1602.04816 [hep-ph] .

[41] X.-D. Shi, G. M. Fuller, and K. Abazajian, (1999), arXiv:astro-ph/9909221 .

[42] S. Dodelson and L. M. Widrow, Phys. Rev. Lett. **72**, 17 (1994).

[43] M. Drewes, Int. J. Mod. Phys. E **22**, 1330019 (2013), arXiv:1303.6912 [hep-ph] .

[44] E. Bulbul, M. Markevitch, A. Foster, *et al.*, The Astrophysical Journal **789**, 13 (2014).

[45] K. Abazajian, G. M. Fuller, and W. H. Tucker, The Astrophysical Journal **562**, 593 (2001).

[46] C. Patrignani *et al.* (Particle Data Group), Chin. Phys. C **40**, 100001 (2016).

[47] M. G. Aartsen, K. Abraham, M. Ackermann, *et al.* (IceCube Collaboration), Phys. Rev. Lett. **117**, 071801 (2016).

[48] D. Abdurashitov, A. Belesev, A. Berlev, *et al.*, Journal of Instrumentation **10**, T10005 (2015).

[49] J. N. Abdurashitov, A. I. Belesev, V. G. Chernov, *et al.*, JETP Letters **105**, 753 (2017).

[50] A. Boyarsky, O. Ruchayskiy, D. Iakubovskyi, *et al.*, Phys. Rev. Lett. **113**, 251301 (2014), arXiv:1402.4119 [astro-ph.CO] .

[51] R. Adhikari, M. Agostini, N. A. Ky, *et al.*, Journal of Cosmology and Astroparticle Physics **2017**, 025 (2017).

[52] H. J. Metcalf and P. van der Straten, "Laser cooling and trapping of neutral atoms," in *The Optics Encyclopedia* (American Cancer Society, 2007) https://onlinelibrary.wiley.com/doi/pdf/10.1002/9783527600441.oe005 .

[53] H. Metcalf and P. [van der Straten], Physics Reports **244**, 203 (1994).

[54] G. D. Sprouse and L. A. Orozco, Annual Review of Nuclear and Particle Science **47**, 429 (1997), https://doi.org/10.1146/annurev.nucl.47.1.429 .

[55] `https://www.crytur.cz/materials/yap-ce/`.

[56] `https://www.photonis.com/products/microchannel-plates` ().

[57] A. Guest, ACTA ELECTRONICA **14**, 79 (1971).

[58] J. Oberheide, P. Wilhelms, and M. Zimmer, Measurement Science and Technology **8**, 351 (1997).

[59] `https://www.triumf.ca/sites/default/files/Hamamatsu%20MCP%20guide.pdf` ().

[60] P. Hamilton, M. Jaffe, J. M. Brown, *et al.*, Phys. Rev. Lett. **114**, 100405 (2015).

[61] K. E. Gibble, S. Kasapi, and S. Chu, Opt. Lett. **17**, 526 (ts , url = http://ol.osa.org/abstract.cfm?URI=ol-17-7-526, doi = 10.1364/OL.17.000526,).

[62] K. Buchtela, edited by P. Worsfold, A. Townshend, and C. Poole (Elsevier, Oxford, 2005) second edition ed., pp. 1–8.

[63] P. F. Smith, New Journal of Physics **21**, 053022 (2019).

[64] L. W. Alvarez, Phys. Rev. **54**, 486 (1938).

[65] W. Coghlan and R. Clausing, Atomic Data and Nuclear Data Tables **5**, 317 (1973).

[66] `https://www.webelements.com/xenon/atoms.html`.

[67] P. Filianin, *Measurements of low decay energies of beta-processes using Penning traps*, Ph.D. thesis, U. Heidelberg (main) (2019).

[68] `https://periodictable.com/Isotopes/055.131/index2.p.full.dm.html` ().

[69] `https://www.nndc.bnl.gov/nudat2/decaysearchdirect.jsp?nuc=131CS&unc=nds` ().

[70] J. Ullrich, R. Moshammer, A. Dorn, *et al.*, Reports on Progress in Physics **66**, 1463 (2003).

[71] W. C. Wiley and I. H. McLaren, Review of Scientific Instruments **26**, 1150 (1955).

[72] V. Mergel, Ph.D. thesis, Universität Frankfurt (1996).

[73] R. Dörner, H. Bräuning, J. M. Feagin, *et al.*, Phys. Rev. A **57**, 1074 (1998).

[74] R. Hubele, M. Schuricke, J. Goullon, *et al.*, Review of Scientific Instruments **86**, 033105 (2015), https://doi.org/10.1063/1.4914040 .

[75] A. Bodi, P. Hemberger, T. Gerber, *et al.*, Review of Scientific Instruments **83**, 083105 (2012), https://doi.org/10.1063/1.4742769 .

[76] R. Dörner, V. Mergel, L. Spielberger, *et al.*, Nuclear Instruments and Methods in Physics Research Section B: Beam Interactions with Materials and Atoms **124**, 225 (1997), fast Ion-Atom Collisions.

[77] C. Dornes, *3D-focusing Spectrometer for a Reaction Microscope*, diploma, Ruprecht-Karls-Universität, Heidelberg, Germany (2011).

[78] T. Kong, *Feasibility Test Of Exotic Particle Searches In The Decay Of Trapped Rubidium Isomers*, Ph.D. thesis, British Columbia U. (2012).

[79] P. Hawkes and E. Kasper, *Principles of Electron Optics*, Principles of Electron Optics No. v. 1 (Academic Press, 1996).

[80] `https://simion.com/`.

[81] G. A. Garcia, H. Soldi-Lose, and L. Nahon, Review of Scientific Instruments **80**, 023102 (2009), https://doi.org/10.1063/1.3079331 .

[82] M. Minot, B. Adams, M. Aviles, *et al.*, Nuclear Instruments and Methods in Physics Research Section A: Accelerators, Spectrometers, Detectors and Associated Equipment **936**, 527 (2019), frontier Detectors for Frontier Physics: 14th Pisa Meeting on Advanced Detectors.

[83] E. Bulbul, M. Markevitch, A. Foster, *et al.*, Astrophys. J. **789**, 13 (2014), arXiv:1402.2301 [astro-ph.CO] .

[84] J. P. Gordon and A. Ashkin, Phys. Rev. A **21**, 1606 (1980).

[85] H. J. Metcalf and P. van der Straten, J. Opt. Soc. Am. B **20**, 887 (2003).

[86] J. D. Jackson, *Classical Electrodynamics* (Wiley, 1998).

[87] `http://www.roentdek.de/products/supplement/Mesh%20and%20Mask%20description.pdf`.

[88] W. C. Young, R. G. Budynas, and A. M. Sadegh, *Roark's formulas for stress and strain; 8th ed.* (McGraw Hill, New York, NY, 2012).

[89] W. D. Phillips, Rev. Mod. Phys. **70**, 721 (1998).

[90] S. Chu, Rev. Mod. Phys , 685 (1998).

[91] C. Cohen-Tannoudji, Physica Scripta **T76**, 33 (1998).

[92] L. E. Ballentine, *Quantum Mechanics*, 2nd ed. (WORLD SCIENTIFIC, 2014) https://www.worldscientific.com/doi/pdf/10.1142/9038 .

[93] D. A. Steck, Cesium D Line Data.

[94] E. L. Raab, M. Prentiss, A. Cable, *et al.*, Phys. Rev. Lett. **59**, 2631 (1987).

[95] C. Monroe, W. Swann, H. Robinson, *et al.*, Phys. Rev. Lett. **65**, 1571 (1990).

[96] K. E. Gibble, S. Kasapi, and S. Chu, Opt. Lett. **17**, 526 (1992).

[97] W. Smythe, *Static and Dynamic Electricity*, International series in pure and applied physics (McGraw-Hill, 1950).

[98] `https://www.comsol.ch/comsol-multiphysics` ().

[99] `http://www.matweb.com/search/datasheet.aspx?bassnum=MT0001&ckck=1`.

[100] `https://www.comsol.com/model/download/735711/models.acdc.parallel_wires.pdf` ().

[101] F. Grover, *Inductance Calculations*, Dover Books on Electrical Engineering (Dover Publications, 2013).

[102] Priv. comm. A. Czasch, RoentDek Corp.

[103] A. Mager, Journal of Applied Physics **39**, 1914 (1968), https://doi.org/10.1063/1.1656455 .

[104] A. Mager, IEEE Transactions on Magnetics **6**, 67 (1970).

[105] D. U. Gubser, S. A. Wolf, and J. E. Cox, Review of Scientific Instruments **50**, 751 (1979), https://doi.org/10.1063/1.1135915 .

[106] A. P. Wills, Phys. Rev. (Series I) **9**, 193 (1899).

[107] W. G. Wadey, Review of Scientific Instruments **27**, 910 (1956), https://doi.org/10.1063/1.1715413 .

[108] E. A. Burt and C. R. Ekstrom, Review of Scientific Instruments **73**, 2699 (2002), https://doi.org/10.1063/1.1487892 .

[109] I. Altarev, M. Bales, D. H. Beck, *et al.*, Journal of Applied Physics **117**, 183903 (2015), https://doi.org/10.1063/1.4919366 .

[110] A. Farolfi, D. Trypogeorgos, G. Colzi, *et al.*, Review of Scientific Instruments **90**, 115114 (2019), https://doi.org/10.1063/1.5119915 .

[111] E. Wodey, D. Tell, E. M. Rasel, *et al.*, Review of Scientific Instruments **91**, 035117 (2020), https://doi.org/10.1063/1.5141340 .

[112] E. A. Burt and C. R. Ekstrom, Review of Scientific Instruments **73**, 2699 (2002), https://doi.org/10.1063/1.1487892 .

[113] R. J. Hanson and F. M. Pipkin, Review of Scientific Instruments **36**, 179 (1965), https://doi.org/10.1063/1.1719514 .

[114] `https://www.comsol.com/model/download/734291/models.acdc.permanent_magnet.pdf` ().

[115] `https://geant4.web.cern.ch/node/1`.

[116] `http://astroa.physics.metu.edu.tr/~umk/astr517/Hamamatsu_PMT.pdf`.

[117] E. W. McDaniel, J. B. Mitchell, and M. E. Rudd, .

[118] K. Chen, S. T. Sullivan, and E. R. Hudson, Phys. Rev. Lett. **112** (2014), 10.1103/PhysRevLett.112.143009.

[119] P. Morrison and L. I. Schiff, Phys. Rev. **58**, 24 (1940).

[120] R. Glauber, Phys. Rev. **109**, 1307 (1958).

[121] J. L. Olsen, Phys. Rev. **106**, 985 (1957).

[122] B. Saraf, **94**, 642 (1957).

[123] C. J. Martoff, F. Granato, V. Palmaccio, *et al.*, Quantum Science and Technology **6**, 024008 (2021).

APPENDIX A

ELECTRODES DESIGN

The designs of the electrodes in the source region are shown in the following figures.Fig. 1 is the design of the regular electrodes in the source region. Fig. 2 is the electrode facing the MOT. The smaller outer radius of this electrode is for leaving adequate clearance for the x-rays. Fan sections are cut off from the electrodes shown in Fig. 3 and Fig. 4 for suppressing the eddy currents.

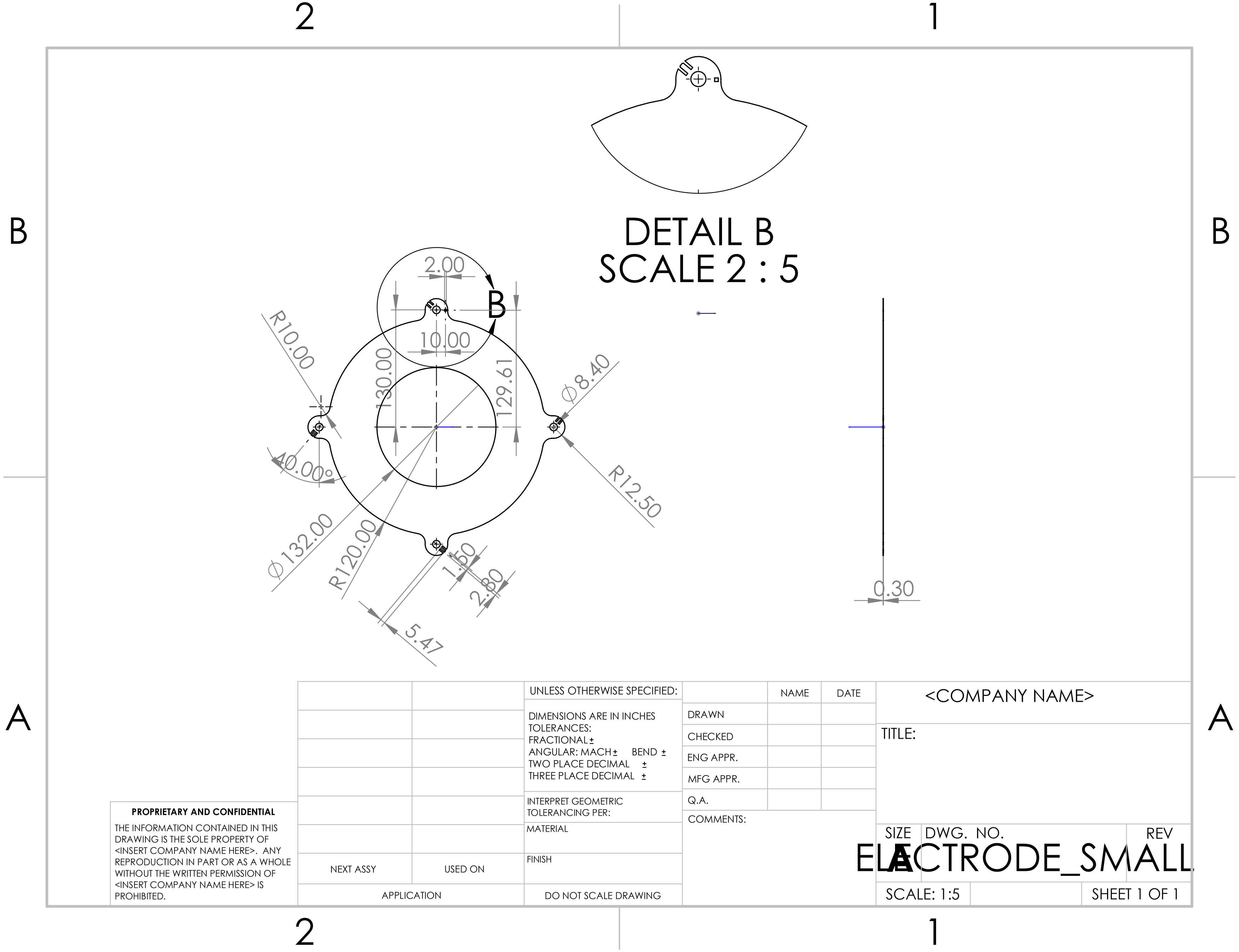

Figure 1: Small electrode in the source region.

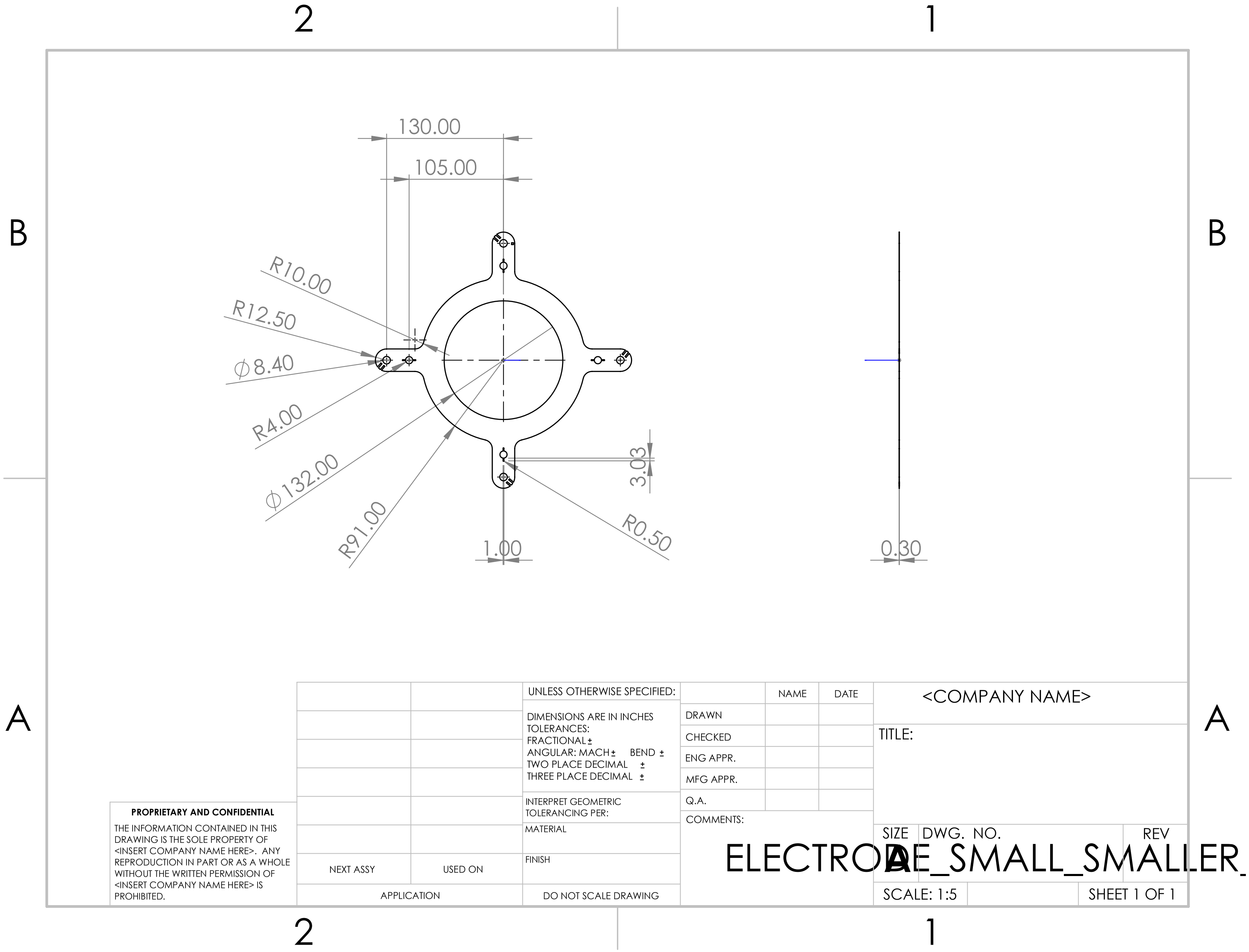

Figure 2: Small electrode facing the MOT.

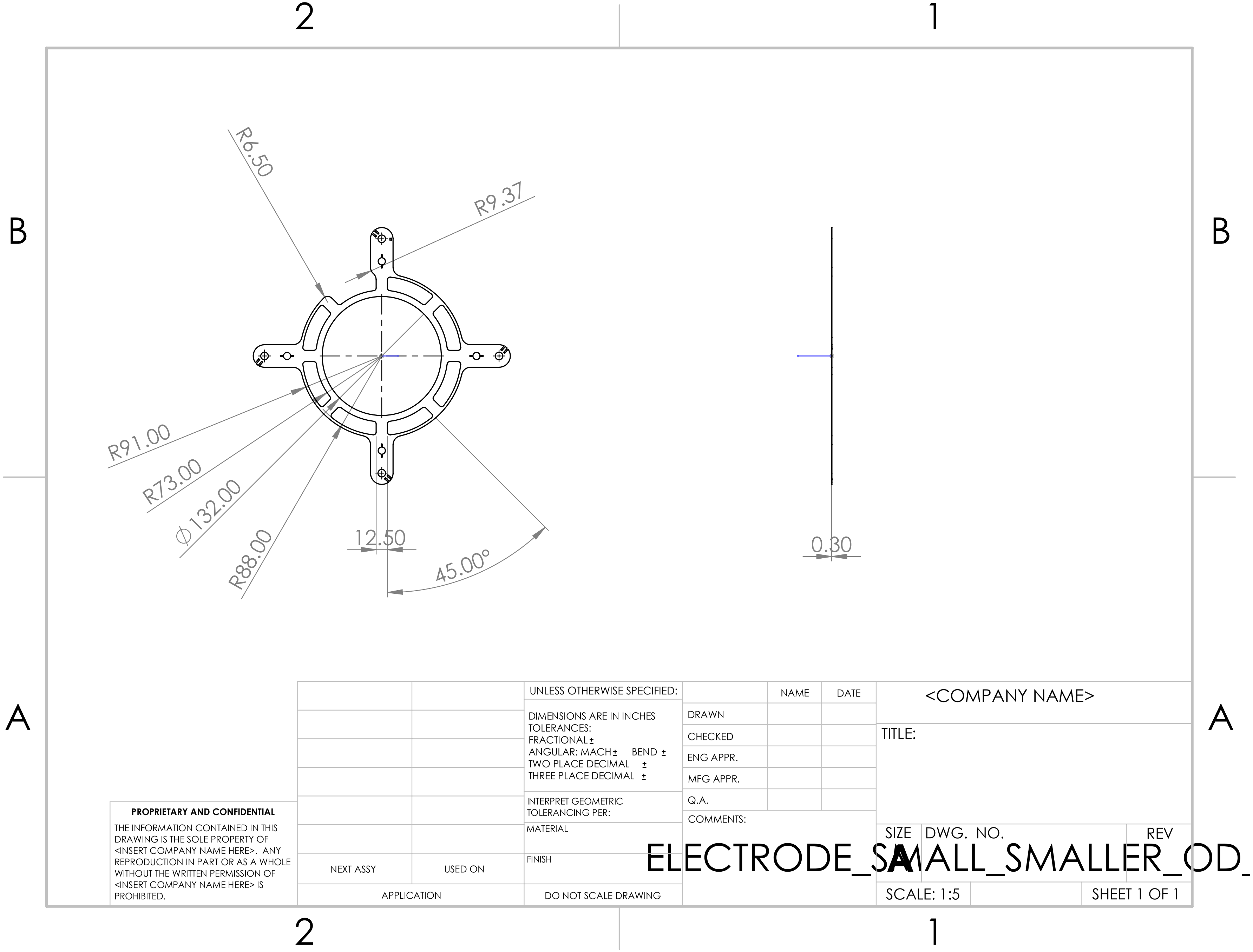

Figure 3: Small electrode sandwiched between the two halves of coil holders.

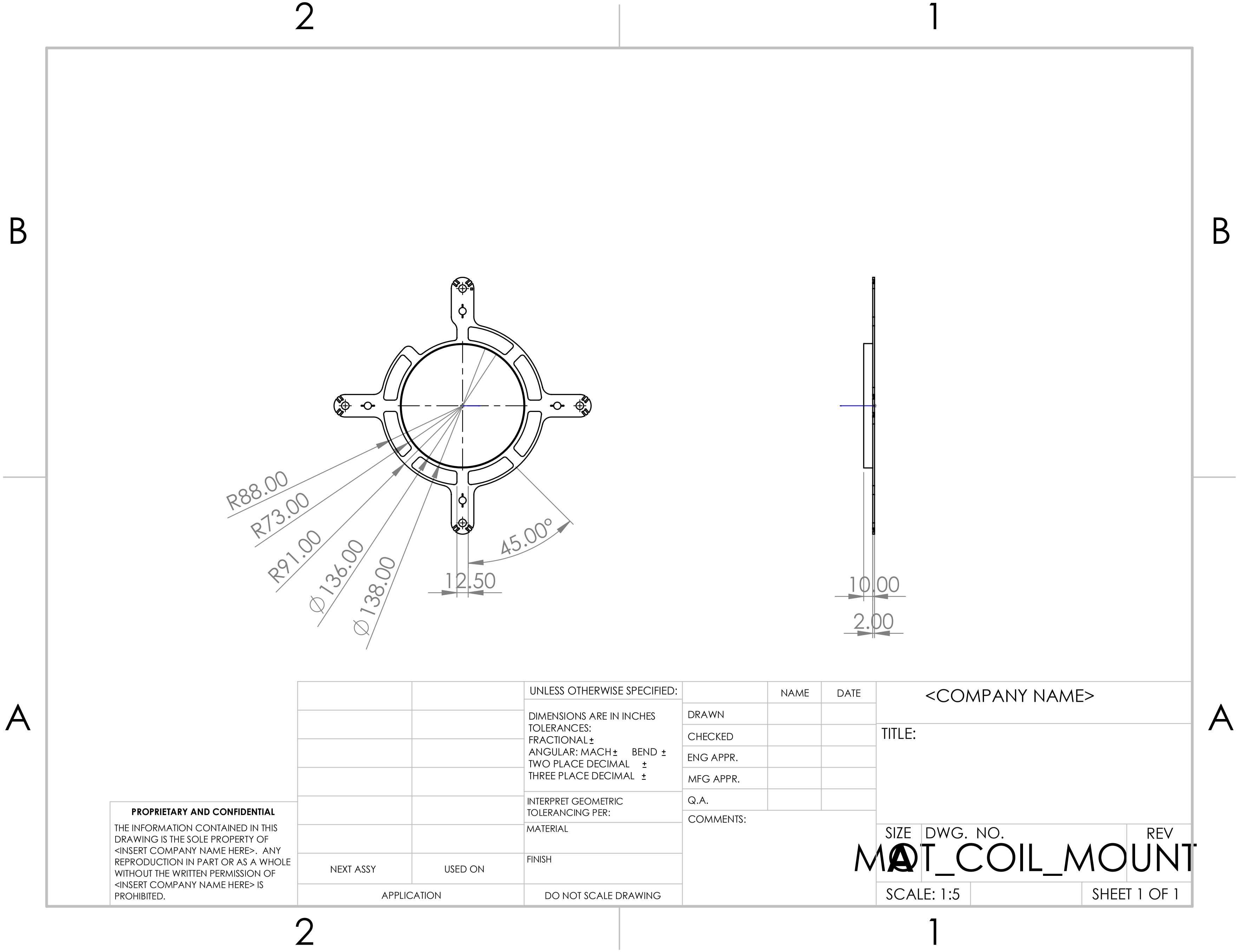

Figure 4: Half of the coil holder.

APPENDIX B

POTENTIALS AND RESOLUTIONS

The potentials of electrodes used for evaluating the ion momentum resolutions are shown in Table. A.1. The large step of the potential between V48 and V49 for the pair of electrodes with 2 mm gap produces a stronger electric field than the fields produced between other electrodes, which forms an electrostatic lens.

V1	V2	V3	V4	V5	V6	V7
-101.836	-114.503	-114.250	-121.024	-119.055	-119.217	-122.370
V8	V9	V10	V11	V12	V13	V14
-120.508	-117.019	-118.058	-115.402	-112.911	-130.507	-117.829
V15	V16	V17	V18	V19	V20	V21
-116.558	-111.905	-111.678	-112.997	-113.089	-109.729	-113.465
V22	V23	V24	V25	V26	V27	V28
-110.514	-112.020	-111.683	-108.815	-108.871	-108.279	-109.653
V29	V30	V31	V32	V33	V34	V35
-108.494	-108.824	-111.031	-110.962	-112.434	-110.283	-110.056
V36	V37	V38	V39	V40	V41	V42
-112.954	-110.453	-112.061	-111.236	-109.182	-110.777	-123.291
V43	V44	V45	V46	V47	V48	V49
-128.793	-131.878	-135.582	-136.642	-132.358	-125.486	-84.976
V50	V51	V52	V53	V54	V55	V56
-80.486	-77.993	-73.130	-71.101	-63.306	-58.408	-54.458
V57	V58	59				
-52.029	-51.132	5.569				

Table A.1: Optimized electrode potentials for the low resolution tune. unit: V

The ions of Set **A** described in Section. 3.5 but with 1000 initial positions were flown to evaluate the resolutions. The evaluated $\delta p_{\parallel}$ and $\delta p_{\perp}$ for ions with charge 2e and 1e emitting in 10 polar angles are shown in Table. A.2. μ_{TOF} (μ_{IR}) and σ_{TOF} (σ_{IR}) are the average TOF (IR) and the standard deviation of the TOF (IR) for 1000 ions in a group, respectively.

q=2e					
Angle(degree)	0.0	22.0	44.0	66.0	88.0
$p_{\parallel}$ (keV/c)	330.000	305.971	237.382	134.223	11.517
$\delta p_{\parallel}$ (keV/c)	0.306	0.330	0.372	0.386	0.369
μ_{TOF} (µs)	68.252	68.155	67.877	67.457	66.953
σ_{TOF} (µs)	0.00091	0.00104	0.00126	0.00132	0.00124
$p_{\perp}$ (keV/c)	0.000	123.620	229.237	301.470	329.799
$\delta p_{\perp}$ (keV/c)	0.314	0.371	0.390	0.455	0.503
μ_{IR} (mm)	0.058	21.569	39.842	52.221	57.232
σ_{IR} (mm)	0.02116	0.04043	0.04549	0.06079	0.07125
Angle(degree)	92.0	114.0	136.0	158.0	180.0
$p_{\parallel}$ (keV/c)	-11.517	-134.223	-237.382	-305.971	-330.000
$\delta p_{\parallel}$ (keV/c)	0.360	0.293	0.248	0.226	0.216
μ_{TOF} (µs)	66.859	66.361	65.940	65.660	65.562
σ_{TOF} (µs)	0.00119	0.00083	0.00054	0.00034	0.00021
$p_{\perp}$ (keV/c)	329.799	301.470	229.237	123.620	0.000
$\delta p_{\perp}$ (keV/c)	0.496	0.397	0.319	0.312	0.305
μ_{IR} (mm)	57.238	52.265	39.848	21.538	0.034
σ_{IR} (mm)	0.06990	0.04719	0.02379	0.02039	0.01691
q=1e					
Angle(degree)	0.0	11.0	22.0	33.0	44.0
$p_{\parallel}$ (keV/c)	330.000	323.937	305.971	276.761	237.382
$\delta p_{\parallel}$ (keV/c)	0.241	0.253	0.279	0.314	0.350
μ_{TOF} (µs)	97.310	97.261	97.117	96.881	96.560
σ_{TOF} (µs)	0.00175	0.00186	0.00209	0.00239	0.00270
$p_{\perp}$ (keV/c)	0.000	62.967	123.620	179.731	229.237
$\delta p_{\perp}$ (keV/c)	0.229	0.303	0.295	0.310	0.380
μ_{IR} (mm)	0.079	15.578	30.502	44.173	56.195
σ_{IR} (mm)	0.02545	0.05496	0.05217	0.05718	0.07858
Angle(degree)	136.0	147.0	158.0	169.0	180.0
$p_{\parallel}$ (keV/c)	-237.382	-276.761	-305.971	-323.937	-330.000
$\delta p_{\parallel}$ (keV/c)	0.147	0.126	0.118	0.113	0.111
μ_{TOF} (µs)	92.684	92.365	92.127	91.980	91.931
σ_{TOF} (µs)	0.00083	0.00057	0.00043	0.00033	0.00030
$p_{\perp}$ (keV/c)	229.237	179.731	123.620	62.967	0.000
$\delta p_{\perp}$ (keV/c)	0.259	0.216	0.219	0.237	0.217
μ_{IR} (mm)	56.311	44.172	30.438	15.522	0.045
σ_{IR} (mm)	0.03941	0.01769	0.01992	0.02955	0.01861

Table A.2: Optimization results of ions are shown in the table. $\delta p_{\parallel}$ and $p_{\perp}$ are the resolution of longitudinal and transverse momentum. μ_{TOF} (μ_{IR}) and σ_{TOF} (σ_{IR}) are the average TOF (IR) and the standard deviation of the TOF for 1000 ions in a group, respectively.